Spin polarized tunneling and spin injection in Fe-GaAs hybrid structures

DISSERTATION

zur Erlangung des Doktorgrades der Naturwissenschaften
(Dr. rer. nat.)
der Naturwissenschaftlichen Fakultät II - Physik
der Universität Regensburg

vorgelegt von
Peifeng Chen
aus Shanghai, China

Regensburg 2006

Die Arbeit wurde angeleitet von: Prof. Dr. Werner Wegscheider
Datum des Promotionskolloquiums: 19.09.2006

Prüfungsausschuss:	Vorsitzender:	Prof. Dr. Jaroslav Fabian
	Erstgutachter:	Prof. Dr. Werner Wegscheider
	Zweitgutachter:	Prof. Dr. Dieter Weiss
	Weiterer Prüfer:	Prof. Dr. Christian Back

Contents

List of Figures

List of Tables

List of abbreviations and symbols

Abbreviations

2DEG	Two Dimensional Electron Gas
AES	Auger Electron Spectroscopy
AP	Anti-parallel
BCS	Bardeen Cooper Schrieffer
CMOS	Complementary Metal-Oxide Semiconductor
COM	Common Ground
DC	Direct Current
DMS	Diluted Magnetic Semiconductor
DOS	Density of States
EBASE	Epoxy Bond and Stop Etch-technique
FE	Field Emission
F/I/F	Ferromagnet/Insulator/Ferromagnet
F/I/S	Ferromagnet/Insulator/Superconductor
F/N/F	Ferromagnet/Non-magnetic metal/Ferromagnet
F/SC/F	Ferromagnet/Semiconductor/Ferromagnet
GMR	Giant Magnetoresistance
MBE	Molecular Beam Epitaxy
MRAM	Magnetic Random Access Memory
MTJ	Magnetic Tunneling Junction
P	Parallel
PMMA	Polymethyl Methacrylate
QW	Quantum Well
SI	Semi-insulating

SMU	Source Monitor Unit
Spin-FET	Spin-polarized Field Effect Transistor
Spin-LED	Spin-polarized Light Emitting Diode
SQUID	Superconducting Quantum Interference Device
STM	Scanning Tunneling Microscope
TE	Thermionic Emission
TFE	Thermionic-field Emission
TMR	Tunneling Magnetoresistance
UV	Ultra Violet
VMU	Voltage Monitor Unit
VTI	Variable Temperature Insert
WKB	Wentzel-Kramers-Brillouin

Symbols

A, B, C	Factors in Simmons model
A^*	Richardson constant
α	Spin wave parameter
α', η, β	Spin selectivity
d, Δs	Barrier thickness
$D(E_x)$	Penetrate probability of an electron with energy level E_x
D	Weighted average diffusion constant
$D_{\uparrow,\downarrow}$	Diffusion constants for spin-up and spin-down channels
Δ	Superconducting energy gap
ΔG	$= G_{max} - G_{min}$
$\Delta\mu_{\uparrow,\downarrow}$	Interfacial discontinuity of electrochemical potential for two spin types
δP_n	Non-equilibrium spin polarization
E, E_x	Energy
E_c	Bottom of conduction band
E_F	Fermi energy level
E_m	Maximum height of the barrier
E_r	$= E_y + E_z$

E_v	Top of valence band
E_0, E_{00}	Tunneling parameters for Schottky barriers
ϵ_s	Semiconductor permittivity
ε'	Tunneling parameter for Schottky barriers under a reverse bias
$F(E)$	Fermi-Dirac distribution function
$F_{1/2}(\eta)$	Fermi integral
φ	Barrier height
φ_n	$= E_C - E_F$
$\bar{\varphi}$	Mean barrier height
$g(V)$	Logarithmic derivative of the conductivity
G	Conductance
$G_{\uparrow,\downarrow}$	Interface conductances for spin-up and spin-down channels
G_0	Spin dependent conductance at 0K
G_{av}	$= (G_{max} + G_{min})/2$
G_{eff}	Effective conductance
G_{max}, G_{min}	Maximum (minimum) conductance of a MTJ
G_{SI}	Spin independent conductance
G_T	Spin dependent conductance
γ'	Exponent to describe spin independent conductance
γ	Interface spin polarization
h	Planck constant
$\hbar$	$= h/2\pi$
I	Current
$j_{\uparrow,\downarrow}$	Current density of spin-up and spin-down channels
$j_P^{\uparrow,(\downarrow)}$, $j_{AP}^{\uparrow,(\downarrow)}$	Current density of spin-up and spin-down channels for parallel and antiparallel configurations
J, J_0, J_{LV}	Current density
J_s, J_{st}, J_{stf}, J_{sf}	Saturation current density
k_B	Boltzmann constant
κ_1, κ_2, β	Wave number
L_{sf}^F, L_{sf}^N, L_{sf}^{SC}	Spin-flip length for ferromagnets non-ferromagnetic metals and semiconductors
m	Mass of electron
μ_B	Bohr magneton

$\mu_{\uparrow,\downarrow}$	Electrochemical potentials for spin-up and spin-down channels
n_0	Electron density
N	Localized hopping states
$N_{\uparrow}(_{\downarrow})$	Majority (minority) density of states
N_c	Effective density of states in conduction band
N_d	Doping density
N_d^+	Ionized donor density
P, P_1, P_2	Spin polarization
P_0	Spin polarization at 0k
P_{n0}	Equilibrium spin polarization
$\psi(x)$	Wave function
q	Magnitude of electronic charge
$r_{\uparrow,\downarrow}$	Interface resistance of spin-up (down) channel
r_b^*	Interface resistance
r_F, r_N	Product of the resistivity by the spin diffusion length for ferromagnetic and non-magnetic metals
R_P, R_{AP}	Resistances of parallel and antiparallel configurations
R_{max}, R_{min}	Maximum (minimum) resistance of a MTJ
$\rho_{\uparrow,\downarrow}$	Resistivity of spin-up (down) channel
ρ_F^*, ρ_N^*	Resistivity of ferromagnetic and non-magnetic metals
S	Parameter to describe spin independent conductance
σ	Conductivity
σ_{1-4}	Conductance peaks in a F/I/S junction
t_N	N region thickness in a F/N/F junction
T	Temperature
T_c	Curie temperature
T_p	Probability of transmission in tunneling junctions
τ_{sf}	Spin relaxation time
$U(x)$, U_0	Potential
V	Voltage
V_i	$= (W_m - W_s)/q$
W	Width of the depletion layer
W_m	Work function of metals
W_s	Work function of semiconductors

χ_s	Electron affinity
ζ	Zeeman splitting in GaMnAs

Abstract

Spin electronics, or spintronics, is a new branch of electronics whereby the spin degree of freedom in electronic devices is employed. For understanding the physics of spin injection in semiconductors, this thesis is aimed at contributing to fabricate ferromagnetic metal-semiconductor hybrid structures, typically Fe-GaAs hybrid structures, in which the spin-polarized transport phenomena are studied. Our investigation which is introduced in this thesis can be divided into two parts.

In order to understand the spin transport at the Fe/GaAs interface, the spin-polarized tunneling is studied first. The Fe/GaAs/Fe/Co magnetic tunneling junctions are fabricated and the TMR effect as well as I-V characteristics are measured at different temperatures. Interpretations of the experimental data by the theoretical model allow us to characterize the junction quality, which shows that apart from the conductivity mismatch problem, the oxidation of the semiconductor surface and the interdiffusion between Fe and GaAs are key issues in the fabrication of high quality ferromagnet-semiconductor hybrid structures. Since the study of the epitaxial growth of Fe on the sulphur-passivated GaAs substrate showed that the chemical inertness of the passivated surface could prevent the oxidation and the interdiffusion of semiconductor material, resulting in the growth of a pure Fe film, the spin-polarized tunneling through a sulphur-passivated GaAs barrier is studied to clarify the passivation effect. However, our experiments show no positive influence of sulphur passivation.

The spin injection in the ferromagnetic metal-semiconductor hybrid structures is investigated in the second part of this work. The theoretical analysis and calculation show that the difference in conductivities between a metal and a semiconductor gives a basic obstacle to effective spin injection, which can be overcome by introducing an interface resistance provided by a Schot-

tky barrier or a tunneling barrier inserted between the ferromagnetic metal and the semiconductor. Before performing the spin injection experiments, we try to measure the interface resistivity of Fe/GaAs Schottky barriers with different doping densities at low temperatures. From the calculation and experiments, we find increasing the doping density decreases the depletion region width and changes the interface resistance. If we control the transport length on the scale of nanometers, the interface resistance of such a Fe/GaAs barrier with a high doping density can meet Fert's condition for efficient spin injection in semiconductors. Using the measured interface resistance as a guide for experimental design, the magnetic *p*-*n* junction diodes and Fe/GaAs/Fe structures are fabricated, and spin injection is investigated in these devices. In the magnetic *p*-*n* junction diode, a negative GMR-like effect is found under a large applied bias, when the relative magnetizations of the two magnetic electrodes are changed from parallel to antiparallel. The experimental finding agrees with the theoretical prediction very well. For spin injection in Fe/GaAs/Fe structures, the experiments are carefully performed by different surface treatments with different doping profiles of the GaAs. The small but clear magnetoresistance could only be found in the device with 50nm homogeneous heavily doped GaAs under a large bias, indicating a surface spin polarization of 2.6% in the Fe/GaAs/Fe structure.

Chapter 1

Introduction

Electrons which are the elementary constituent components of electronic devices not only carry electrical charge but also have a magnetic character contained within their spin. Although the electron spin has been known for most of the 20th century, today's semiconductor devices are restricted to the precise manipulation of the charge only. Spin electronics, or spintronics, refers to the study to employ this spin properties instead of or in addition to the charge degree of freedom [1, 2]. Taking additional advantage of the electron spin might revolutionize traditional electronics.

Presently the research in the field of spin-dependent transport is driven by two aspects: commercial application and fundamental research. The applied side is based on the very rapid commercial success of giant magnetoresistance (GMR) devices, which work as read head sensors in the hard-disks, entering large-scale production within ten years in the magnetic data storage industry. Moreover, magnetic random access memories (MRAM) as a fast, non-volatile replacement for the current CMOS based random access memory has also received a great deal of interest [3]. On the other side, the physics of spin is interesting for the study of quantum computation. The intrinsic binary property of the electron spin suggests it could be used as the basic unit (qubit) for quantum information storage and processing. Compared to Coulomb interactions, spin interactions with the environment and with other spins are much weaker, one expects that spin coherence should be preserved on much longer time scale. Therefore electron or nuclear spins forming the qubits are proposed for the realizations of quantum computers [4, 5].

Using semiconductors for spintronic applications has a distinguished advantage: integration of spintronics with traditional semiconductor technology. A generic semiconductor spintronics approach requires three steps: injection of nonequilibrium spins into the semiconductor; spin storage, manipulation and transfer; and spin detection [6]. It is found that the injected nonequilibrium spin can survive for a reasonably long time in the semiconductor, typically in nanoseconds and diffuse over micron distances from the point of injection, which is sufficient for microelectronics applications [7]. For the spin detection, optical observation of circular polarization of the recombination light or electrically detection of nonequilibrium spins in semiconductors such as magnetoresistance can be used [8]. However, the efficient spin injection from a ferromagnetic source into a semiconductor is still more difficult than that of charge [9], remaining a challenging task. This thesis is aimed at contributing to fabricate ferromagnetic metal-semiconductor hybrid structures, typically Fe-GaAs hybrid structures, in which the spin-polarized transport phenomena are studied to understand the physics of spin injection in semiconductors.

1.1 A brief introduction to spintronics

Historically in electronics, the electron spin has mostly been neglected until the first determination of the spin polarization of the conduction band in a ferromagnetic material has been performed by Tedrow and Messervey et al. in the early 70's [10]. This was achieved by studying the magnetoresistance of a ferromagnet/insulator/superconductor (F/I/S) junction. It was found that the tunneling current remains spin polarized even outside of the ferromagnetic region. The Zeeman split quasi particle density of states in a superconductor was used as a detector in such a junction. Based on their experiments, the spin polarization at the Fermi level in the ferromagnet could be determined which is varying between 43% in permalloy of $Ni_{80}Fe_{20}$ and 11% in Ni.

Jullière extended the work to the ferromagnet/insulator/ferromagnet (F/I/F) junctions, where the insulator was amorphous germanium. The tunneling magnetoresistance (TMR) of this magnetic tunnel junction (MTJ) depends on the relative magnetization of the two ferromagnetic electrodes [11]. Assuming that spin and total energy is conserved during the tunneling pro-

cess, the conductance will be proportional to the products of the densities of states for each subband, therefore to the relative magnetization of the two ferromagnetic layers. Thus, Jullière formulated a model for a change of conductance between the parallel and antiparallel magnetic configurations in the two ferromagnetic layers by adopting Tedrow's analysis of the tunneling conductance from F/I/S to the F/I/F junctions.

Although spin polarized tunneling between two ferromagnet films was known from the experiments of Jullière, yet it has not been successfully realized for twenty years. The major problems are related to the technological demanding of fabrication processes, which is necessary to fabricate robust and reliable tunnel junctions [12]. In 1995, Miyazaki and Tezuka et al. demonstrated the possibility to obtain large values of TMR in the tunnel junction with Al_2O_3 insulating barriers [13], and Moodera et al. developed a fabrication process which appeared to fulfill the requirements for smooth and pinhole-free Al_2O_3 deposition [14]. In these days, MTJs that are based on ferromagnetic films and Al_2O_3 barriers can be routinely fabricated with reproducible characteristics and with TMR values up to 50% at room temperature, making them suitable for applications in the industry [15].

The TMR effect is a spin dependent interface effect, and it does not require nonequilibrium spin accumulation or transport in a non-magnetic material. For the spintronic applications, the current flow and manipulation of the nonequilibrium spins is essential. The first prototypical spintronic device, the spin field-effect transistor (spin-FET), was proposed by Datta and Das [16]. The spin-FET consists of ferromagnetic source and drain contacts that are connected by a two-dimensional electron gas (2DEG) formed at the heterojunction between two narrow gap semiconductor materials. The presence of ferromagnetic injector and drain allows the observation of the spin of electrons. In a simplified picture, the electron can enter the drain when its spin points in the same direction as the spin orientation of the drain. Otherwise it is scattered away. The function of the gate is to generate an effective magnetic field, arising from the Rashba-type spin-orbit interaction. This effective magnetic field causes the electron spins to precess. By modifying the voltage, one can lead the precession to either parallel or antiparrelel to electron spin at the drain, effectively controlling the current. The essential requirements for a spin-FET device are: first, an efficient injection of the spin polarized current from ferromagnet to semiconductor; second, a long

spin relaxation time in the semiconductor.

The first successful experiments to measure the spin relaxation time (τ_{sf}) in bulk n-GaAs were all optical experiments reported by Kikkawa et al. [17], where circularly-polarized pumping and time-resolved Faraday rotation spectroscopy have been employed. In these experiments, it was found for a doping density $N_d = 1 \times 10^{16}\text{cm}^{-3}$ of Si donors in GaAs at the temperature of 5K, the observed τ_{sf} was 120ns at zero magnetic field. With greater and smaller doping densities, spin relaxation times are significantly reduced [18].

With respect to the issues of how to realize in practice spin injection and detection, different approaches were taken. Considerable efforts have been dedicated to observe the spin valve effect with semiconductors as the intermediate layer, which is the first step towards the realization of the spin-FET. Direct spin injection from a ferromagnet into a 2DEG showed very small effects [19, 20], with arguments about the presence or absence of spin injection [21, 22].

Moreover, the spin injection from the ferromagnetic metal into a 2DEG by ohmic contacts has so far resulted in low efficiencies, because the conductance mismatch between the ferromagnetic metal and semiconductor is believed to represent the intrinsic obstacle for spin injection [9]. In order to overcome the conductance mismatch problem, a Schottky barrier or a tunneling barrier insertion between the ferromagnetic metal and the semiconductor producing an interface resistance, or even the diluted magnetic semiconductor (DMS) used as a spin injector are proposed by Rashba and Schmidt et al. [23, 24]. The experimental focus hence shifted from spin injection in 2DEGs to other approaches.

Clear spin injection was demonstrated by Zhu et al. in a spin-polarized light emitting diode (Spin-LED) in 2001 [25]. They drove current from ferromagnetic Fe across a Schottky barrier into a light emitting diode and subsequently performed optical detection of spin injection by observation of the polarization of the emitted light. In their experiments, the results could be understood in terms of tunneling to overcome the conductance mismatch obstacle for the spin injection from the ferromagnetic material into the semiconductor. Recently, spin injection from Fe into an identical GaAs based spin-LED using different tunnel barriers i.e. a reverse-biased Fe/AlGaAs Schottky barrier and a Fe/Al_2O_3 barrier were done by Hanbicki

and Jonker et al. They found the spin polarization could be achieved in GaAs up to 30% typically [26, 27].

A similar experiment has already been performed by Ohno et al. in 1999, where electrical spin injection occurs from a diluted magnetic semiconductor into a non-magnetic semiconductor [28]. Under forward bias, spin polarized holes from the p-type diluted magnetic semiconductor (DMS) GaMnAs and unpolarized electrons from a n-type GaAs substrate are injected into an embedded InGaAs quantum well (QW) separated from the ferromagnetic region by a spacer layer. The hole spin polarization in the QW was measured by analyzing the polarization of the emitted electroluminescence. A highly efficient spin injection up to 80% in GaAs has been observed using GaMnAs as a spin injector in a Zener diode structure [29]. However, the low Curie temperature (T_c) of the material is the drawback of the usage of diluted magnetic semiconductors as spin injectors.

The spin-LED experiments have proved successful spin injection in semiconductors. However, from a device point of view, a major breakthrough still would be to have an all electronic device which can preferably operate at room temperature. As the ferromagnetic metals have a high Curie temperature, well known magnetic properties and a significant spin polarization even at room temperature, efforts have been dedicated to the study on ferromagnet/semiconductor/ferromagnet (F/SC/F) hybrid structures, which is helpful to clarify the spin-dependent transport at ferromagnet-semiconductor interfaces [30, 31]. However, the TMR effect achieved in the Fe/GaAs/Fe tunneling junctions is only 0.21%, much less than the theoretical predicted value. It suggests that apart from the conductance mismatch problem, the fabrication of clean and robust interfaces between ferromagnetic metals and semiconductors is another important issue for spin injection.

We conclude our brief introduction of the study of spin-dependent electronics here. The overview was not intended to be exhaustive. For example, the observation of spin effects in scanning tunneling microscope (STM) experiments is not included here [32]. However, from the present research introduced above, it is evident that in order to achieve a significant spin polarization of conduction electrons in the semiconductor, it is necessary to control the interface quality and introduce an interface resistance between ferromagnetic metals and semiconductors.

1.2 This thesis

The question to be addressed in this thesis is whether we can improve the interface quality between ferromagnetic metals and semiconductors, and whether we can inject spin-polarized electrons into a semiconductor and subsequently detect it all electrically. The detailed structure of this thesis is shown below:

Chapter 2: The fundamental concepts necessary to understand the spin polarized tunneling in F/SC/F junctions is introduced. Ferromagnetism and Schottky barriers between metal and semiconductor are reviewed, followed by an introduction to the theory of tunneling. Next, the magnetic tunneling junction and spin polarized tunneling is emphasized as the onset for the other chapters.

Chapter 3: The technology needed to fabricate our tunneling junctions and spin injection devices, and the measurement setup of the transport properties are described. The wafer structure and critical fabrication processes are also discussed in this chapter.

Chapter 4: In order to understand the low TMR effect in the Fe/GaAs/Fe junctions, the temperature dependence of the spin polarized tunneling is studied. A theoretical model including spin dependent tunneling and spin independent tunneling to describe the temperature dependence of the TMR effect is introduced in this chapter. It is found that measuring the TMR effect at different temperatures in combination with interpretations of the experimental data by the theoretical model allows us to characterize the junction quality. The study shows that the oxidation of the semiconductor surface and the interdiffusion between Fe and GaAs are key issues to increase the TMR effect in such a junction.

Chapter 5: Since the epitaxial experiments of ferromagnetic metal layers on the passivated GaAs substrate shows that sulphur-passivation on GaAs surfaces can prevent the interdiffusion of As into the Fe overlayer effectively, the study of the spin-polarized tunneling through the sulphur-passivated GaAs barrier is introduced in this chapter. The tunneling junction with a

GaAs barrier which is passivated in an aqueous ammonium sulphide $(NH_4)_2S$ solution is fabricated and the tunneling I-V characteristics and TMR effect are measured at low temperatures. However, the study shows that the TMR effect with sulphur-passivated GaAs barriers is reduced compared to the barriers without passivation, which we attribute to the presence of spin-flip scattering in the passivation layer.

Chapter 6: The fundamental concepts and drift-diffusion model to understand the spin transport in hybrid structures are introduced. The transport property of a ferromagnet/normal metal (F/N) junction is discussed first. The theoretical analysis shows that the conductance mismatch, which is the intrinsic obstacle for the spin injection in semiconductors, can be overcome by the interface resistance insert between the ferromagnet and the semiconductor. The Fert's condition for spin injection in a F/SC/F is introduced next, followed by a simple introduction to the spin injection through a depletion layer in a magnetic p-n junction. The theories introduced here will be used as the guide to design the spin injection devices.

Chapter 7: Since a key element to realize the spin injection is the control of the interface resistance to overcome the conductance mismatch, the I-V characteristics of Schottky barriers between Fe and GaAs with different doping densities have been investigated. The current transport mechanisms in the Schottky barrier have been reviewed and the depletion layer width and the Fermi energy have been calculated. The I-V characteristics shows that the field-emission is the dominant transport mechanism when the doping density of GaAs is sufficient high. The analysis of the semiconductor resistivity at low temperatures and the interface resistance of the Fe/GaAs barrier show that the Schottky barrier with proper doping density can fulfill Fert's condition for spin injection in semiconductors.

Chapter 8: In the last chapter, we will describe our experimental efforts in realizing the electrical spin injection in semiconductors. Schottky barrier of Fe/GaAs are used to produce the interface resistance to overcome the conductance mismatch between ferromagnets and semiconductors. We studied the magnetic p-n junction diode covered by a ferromagnetic metal layer. The spin-polarized electrons are injected from Fe into the bulk n-GaAs via

Schottky contacts and then drift across the depletion layer into p-GaMnAs by a positive bias applied on the diode. When the relative magnetizations of the two magnetic electrodes are changed from parallel to antiparallel, the magnetic p-n junction diode displays a GMR-like effect. The spin injection in F/SC/F junctions is also studied in this chapter. Small but clear magnetoresistance has been observed in this structure, where the transport region is homogeneously and heavily doped GaAs.

Chapter 2

Fundamental concepts of spin polarized tunneling

In this chapter, some of the basic concepts of spin-polarized tunneling and related phenomena will be covered, which act as the basic reference for the study of F/SC/F tunneling junctions. In section 2.1, we first introduce the magnetic materials. The ferromagnetic metal/semiconductor Schottky barrier is then discussed in section 2.2. Finally, section 2.3 and section 2.4 tackles the subject of a simple model of electron tunneling through an ideal rectangular barrier and spin-polarized tunneling in magnetic tunneling junctions.

2.1 Ferromagnetism

For the transition metals Fe, Ni and Co, they have two partially filled bands, which are the $3d$ and $4s$ bands. Because of the Heisenberg exchange interaction, there is an unbalance between the density of spin-up and spin-down electrons populating the $3d$ band, which gives rise to a net magnetic moment per atom [33–35]. The majority (minority) electrons are referred to the electrons in the spin band with the highest (lowest) number of occupied stated. In the $4s$ band, a weaker exchange interaction causes an approximately equal distribution of spin-up and spin-down electrons. Thus, the $3d$ band is responsible for the magnetism of the transition metals [36]. The spin polarization P of a ferromagnet is defined as the spin asymmetry in the

density of states (DOS) at the Fermi level:

$$P = \frac{N_\uparrow(E_F) - N_\downarrow(E_F)}{N_\uparrow(E_F) + N_\downarrow(E_F)}, \tag{2.1}$$

where $N_\uparrow(_\downarrow)$ represents the majority (minority) DOS, respectively. In the bulk magnetic transition metals, the DOS at the Fermi level is dominated by the spin-split d band and a high P is expected assuming simple parabolic bands. Since the electrons responsible for conduction processes are those close to the Fermi level, this means that a current flowing through a ferromagnet is spin polarized with a polarization approximately described by P. The majority (minority) carriers are the electrons with the highest (lowest) DOS at the Fermi level for a particular spin [37].

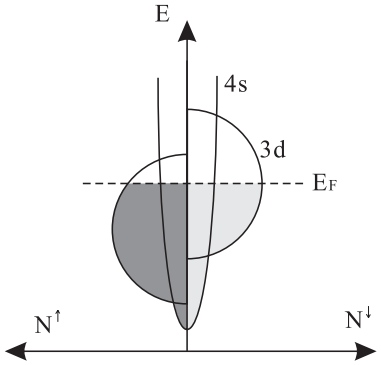

Figure 2.1: *A simplified band picture for the magnetic transition metals. The 3d band is split into a spin-up and spin-down part and causes a net magnetic moment per atom and a spin dependent density of states, $N(E)$. The Fermi level E_F is indicated by the dashed line.*

2.2 Schottky Barrier

The ferromagnetic metal/semiconductor Schottky barriers play an important role in our experiments. Many of the properties of the MTJ or spin injection device are determined by the interface characteristics of Fe/GaAs in this work, so the basic concepts of such a Schottky barrier will be discussed here, except for the details of the I-V characteristics and interface resistance discussed in chapter 7.

2.2.1 Ideal metal-semiconductor contact

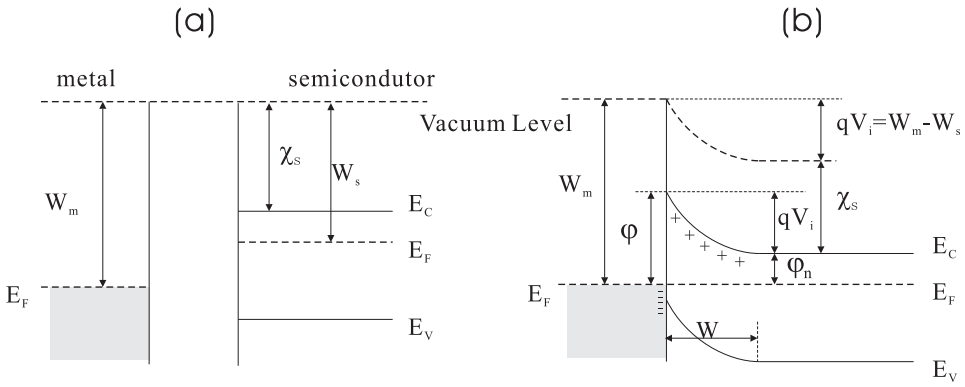

Figure 2.2: *Electron energy diagram of a metal contact to an n-type semiconductor [38]. (a) The two materials separated from each other (b) Thermal equilibrium situation after the contact has been made*

Schottky barriers are intrinsic energy barriers which are formed at the interfaces of most metal/semiconductor junctions. It comes from the fact that difference in electron densities in the given metal and a given semiconductor leads to a difference in the Fermi energies of the two materials. The earliest model to explain this phenomena is that of Schottky and Mott [38, 39]. According to this model the barrier results from the difference in the work functions of the two materials. The energy band diagram in Fig. 2.2 illustrates the process of a Schottky barrier formation. Fig. 2.2(a) shows the electron energy band diagram of a metal of working function W_m and an n-type semiconductor of work function W_s. For the semiconductor, W_s is a variable quantity because the Fermi level varies with the doping density. The other important surface parameter of the semiconductor is the electron affinity χ_s. Fig. 2.2(b) shows the energy band diagram after the contact is made and equilibrium has been reached. When the two substances are brought into intimate contact, electrons from the conduction band of the semiconductor which have higher energy flow into the metal until the Fermi level on the two sides is identical. The barrier height from the metal towards the semiconductor is given by:

$$\varphi = qV_i + \varphi_n, \tag{2.2}$$

where $\varphi_n = E_C - E_F$ and $qV_i = W_m - W_s$. The electron from the conduction band which moves into the metal leave a positive charge of the ionized donor behind, so the semiconductor region near the metal becomes depleted of mobile electrons. According to the Poisson equation, the width of the depletion layer can be described as:

$$W = \sqrt{\frac{2\epsilon_s}{qN_d}(\varphi - V)}, \tag{2.3}$$

where ϵ_s is the semiconductor permittivity, N_d is the doping density, V is applied voltage [38].

2.2.2 Image force and surface states

In general, the barrier height of metal/semiconductor junctions are determined by both the metal and semiconductor work functions. However, the real barrier height is usually different from the value predicted by equation (2.2), because of the image force and specific interface conditions [40]. Assuming that an electron is at a distance x from the metal surface, a positive charge will be induced in the metal. Thus, the image force is defined as the attractive force between the electron and an equal positive charge located at $-x$. When an electric field is applied, it will lower the Schottky barrier. On the other hand, the semiconductor at the surface does not have the same band structure as in the bulk. At the boundary between the semiconductor and an oxide layer, which is almost always present at the surface, there are surface states. The surface states that change the barrier height have continuous distribution in energy within the energy gap. Considering the image force and surface states, the experimental data can be explained better than the simplistic model introduced above. However, it still cannot explain many properties of the Schottky barrier diodes. Usually the effective barrier height is still determined from experimental data.

2.3 Tunneling

In classical physics, it is impossible to explain the transmission of electrons through a barrier when the barrier potential energy is greater than the electron kinetic energy. However, quantum mechanics can explain such an observed transmission successfully [41]. In this section, a simple model of

electron tunneling through an ideal rectangular barrier is presented first; it is then extended to derive expressions for the current density. Next, An extremely important theory of Simmons' tunneling model in metallic junctions related to our experiments is presented. In the following, the temperature dependence of the tunneling within this model is described. The method to determine the barrier height in the tunneling effect is also discussed in this section.

2.3.1 One dimensional rectangular barrier

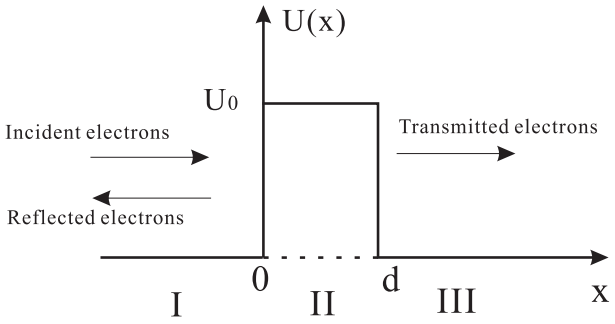

Figure 2.3: *The rectangular tunnel barrier*

In this section, a simple representation of quantum mechanical tunneling applies to electron transport through a barrier consisting of two metals separated by an insulator. In order to simplify the problem, we assume that the metals are identical, the interface is perfect, image potentials are negligible and interactions are elastic. Fig. 2.3 represents the rectangular barrier which describes this situation. Additionally, free electrons in metals can be considered to have a potential energy $U(x) = 0$, and the barrier has a potential $U(x) = U_0$ ($U_0 > 0$) acting over the region $0 \leq x \leq d$. When the particle energy E is smaller than U_0, the wave function $\psi(x)$ can be obtained by solving the time independent, one dimensional Schrödinger equation:

$$\left(-\frac{\hbar^2}{2m}\nabla^2 + U_0\right)\psi(x) = E\psi(x), \tag{2.4}$$

where $\hbar = h/2\pi$, h is Planck's constant and m the mass of the particle. The

general solution to the Schrödinger equation are:

$$\psi(x) = \begin{cases} A\exp(i\kappa_1 x) + B\exp(-i\kappa_1 x) & x < 0 \\ C\exp(i\beta x) + D\exp(-i\beta x) & 0 \leq x \leq d \\ E\exp(i\kappa_1 x) & d < x \end{cases} \tag{2.5}$$

with wave number κ_1 and β:

$$\kappa_1 = \sqrt{\frac{2mE}{\hbar^2}}, \quad \beta = \sqrt{\frac{2m(U_0 - E)}{\hbar^2}}. \tag{2.6}$$

At the boundaries of the potential barrier, both the wave functions and their differentials must be continuous. Solving equation (2.5), the constants B, C, D and F are found in terms of A. The probability of transmission T_p is given by the squared amplitude ratio $|E|^2 / |A|^2$ between the incident and the transmitted wave function and can be approximated by

$$T_p \approx \frac{16\beta^2\kappa_1^2}{(\kappa_1^2 + \beta^2)^2} e^{-2\beta d}. \tag{2.7}$$

Thus, the transmission decays exponentially with the barrier thickness d. Suppose that the left and the right electrodes are not identical, then equation (2.7) should be written as:

$$T_p \approx \frac{16\beta^2\kappa_1\kappa_2}{(\kappa_1^2 + \beta^2)(\kappa_2^2 + \beta^2)} e^{-2\beta d} \tag{2.8}$$

where κ_1 and κ_2 represent the wave numbers corresponding to the two electrodes.

2.3.2 WKB approximation

Now we consider the case when the metal electrodes are not identical, resulting in an asymmetric barrier as depicted in Fig. 2.4. The time independent, one-dimensional Schrödinger equation (2.4) is used with the same assumptions as above. However, the potential energy $U(x, V)$, is now a function of both distance x, and the applied potential V. The Wentzel-Kramers-Brillouin (WKB) approximation describes the effect of a varying potential within the barrier region [42]. This approximation involves solving the Schrödinger equation for the tunneling barrier, noting that it breaks

down at the classical turning points of the particles, and then interpolating solutions on either side of each turning point to produce a smooth wave function [41]. This allows the derivation of the transmission coefficient, as shown by equation (2.9)

$$T_p = \exp\left(\frac{-2}{\hbar}\int_0^d \sqrt{2m(U(x)-E)}dx\right). \tag{2.9}$$

2.3.3 Current density calculation

The current density which is obtained by the stationary state model is introduced here. This model is simple and self-contained. Following convention, if a positive bias V is applied over the junction, it will lower the Fermi level of the right hand electrode, see Fig. 2.4. Current may pass in either direction and $J = J_{12} - J_{21}$, where J is the total current density, J_{12} and J_{21} are the current densities from one to two and vice versa. J_{12} describes the integral of the electron charge multiplied by the group velocity, transmission coefficient T_p and Fermi-Dirac distribution functions that specify the transport occurring between a full and an empty state over all available states in k-space:

$$J_{12} = \frac{2}{(2\pi)^3}\iiint e\left(\hbar^{-1}\frac{\partial E}{\partial k_x}\right)T_p(F(E)[1-F(E+eV)])dk_x dk_y dk_z \tag{2.10}$$

where the factor 2 represents the spin degeneracy and $1/(2\pi)^3$ normalizes to the number of states per unit volume in k-space. J_{21} can be derived similarly. Then, the total current density can be calculated by changing the integration variable:

$$J = \frac{2e}{(2\pi)^3\hbar}\int_0^\infty dE_x[F(E)-F(E+eV)]\iint T_p dk_y dk_z. \tag{2.11}$$

2.3.4 Simmons Model

Simmons derived a simple theory for the current flow through a generalized barrier which is very similar to that introduced above [43–45]. The theory is applied to the situation of the rectangular barrier, where he assumed the mean barrier height as a constant $\bar{\varphi}$ (Fig. 2.4). His theory used the WKB approximation as the starting point. The barrier is assumed to be in the x

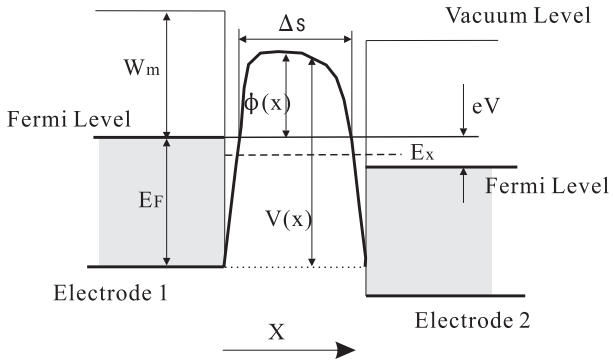

Figure 2.4: *General barrier of an insulating film between two metal electrodes. V is the applied positive voltage, Δs is the barrier thickness and W_m is the work function of the metal electrode [43].*

direction and the tunneling current density J is given by:

$$J = \frac{4\pi me}{h^2} \int_0^{E_m} D(E_x)dE_x \int_0^{\infty} [F(E) - F(E+eV)]dE_r, \tag{2.12}$$

where $E_r = E_y + E_z$, E_m is the maximum height of the barrier and $D(E_x)$ is the probability that an electron of an energy level E_x can penetrate the potential barrier between the electrodes.

Temperature independent J-V

If we only consider the low temperatures, the thermal current can be neglected and the tunneling current equation (2.12) becomes

$$J = J_0 \left\{ \bar{\varphi} \exp(-A\bar{\varphi}^{\frac{1}{2}}) - (\bar{\varphi} + eV) \exp[-A(\bar{\varphi} + eV)^{\frac{1}{2}}] \right\}, \tag{2.13}$$

where

$$J_0 = e/2\pi h(\beta\Delta s)^2, \quad A = ((4\pi\beta\Delta s)/h)(2m)^{\frac{1}{2}}. \tag{2.14}$$

In equation (2.14), Δs is the barrier thickness and β is a function of the barrier shape which can be usually set equal to unity. Equation (2.13) can be interpreted as a current density $J_0\bar{\varphi}exp(-A\bar{\varphi}^{\frac{1}{2}})$ flowing from the left electrode to the right electrode and a current density $J_0(\bar{\varphi}+eV)exp[-A(\bar{\varphi}+eV)^{\frac{1}{2}}]$ flowing from the right electrode to the left, resulting in a net current density J.

For very low voltage, a more convenient form can be deduced from equation (2.13) and written as:

$$J = J_{LV}\bar{\varphi}^{\frac{1}{2}}V\exp(-A\bar{\varphi}^{\frac{1}{2}}), \tag{2.15}$$

$$J_{LV} = [(2m)^{\frac{1}{2}}/\Delta s](e/h)^2. \tag{2.16}$$

Since eV is very small, $\bar{\varphi}$ is considered to be the zero voltage mean barrier height. Thus, in this case, equation (2.15) expresses J as a linear function of V.

Temperature dependent J-V

In order to consider the thermal behavior of the junction J-V characteristics, equation (2.12) becomes

$$J(V,T) = \frac{4\pi mekt}{h^3}\int_0^{E_m}\ln\left\{\frac{1+\exp[(E_F-E_x)/kt]}{1+\exp[(E_F-E_x-eV)/kt]}\right\} \cdot\exp(-A\left\langle\varphi(E_x)\right\rangle_{av}^{\frac{1}{2}})dE_x, \tag{2.17}$$

where $\left\langle\varphi(E_x)\right\rangle_{av}$ is the mean barrier height above E_x. From the integration of equation (2.17), we obtain

$$J(V,T) = (4\pi me/h^3B^2)[\pi Bkt/\sin(\pi Bkt)] \cdot\exp(-A\bar{\varphi}^{\frac{1}{2}})[1-\exp(-BeV)], \tag{2.18}$$

$$J(V,T)/J(V,0) = \pi Bkt/\sin(\pi Bkt) = CT/\sin(CT) \tag{2.19}$$

$$\approx 1+\frac{1}{6}(\pi Bkt)^2\cdots \tag{2.20}$$

where $B = A/2\bar{\varphi}^{\frac{1}{2}}$ and $C = \pi Bk$. From equation(2.19), we can determine the temperature dependence at a given voltage [46].

2.3.5 Determining the Schottky barrier height

In the tunneling experiments of F/SC/F structures, the barrier thickness (d) and the barrier height (φ) are important intrinsic parameters for tunneling characteristics. One of the methods to get these parameters is to use fits of the current-voltage (I-V) curve to Simmons formulas. Especially at low voltages, J can be expressed as a linear function of V as described in equation (2.15). However, it appears that in these fits the extracted parameters,

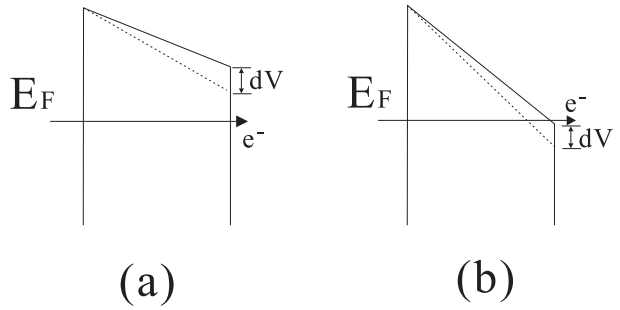

Figure 2.5: *Intuitive understanding of the $g(V)$ curve: (a) For an external voltage below the barrier height, only the average barrier height decreases for a small voltage increase. (b) If the external voltage is just higher than the barrier height, a small increase of the voltage also makes the tunneling length to decrease [47].*

i.e. the barrier thickness and barrier height, are always correlated and the independent evaluation of one of these parameters is impossible.

The other way to determine the barrier height directly and independently is introduced by Rottländer et al. [47, 48]. The method is to plot the logarithmic derivative of the conductivity g against the applied voltage. The logarithmic derivative of the conductivity is defined as:

$$g(V) = d[\ln I(V)/V]/dV. \tag{2.21}$$

The plot produces a cusp at a voltage of about 1.2 times the barrier height of the positively biased electrode, where the constant 1.2 is obtained from the numerical evaluation. Intuitively, this can be understood if one keeps in mind the following fact. For a sharp metal insulator interface, see Fig.2.5, if an external voltage at the positively biased electrode is below the barrier height, a small increment dV of the voltage only decreases the average barrier height. If an external voltage is just higher than the barrier height, then even a small voltage increment will decrease not only the barrier height but also the effective barrier width. Since the barrier width is more effective since the tunnel probability is roughly proportional to $\exp(-d\sqrt{m\varphi})$, the logarithmic derivative therefore increases. With a further increase of the external voltage, the effect of the reduction of the effective barrier width is less strong, and the derivative decreases again. Fig. 2.6 shows the simulations of

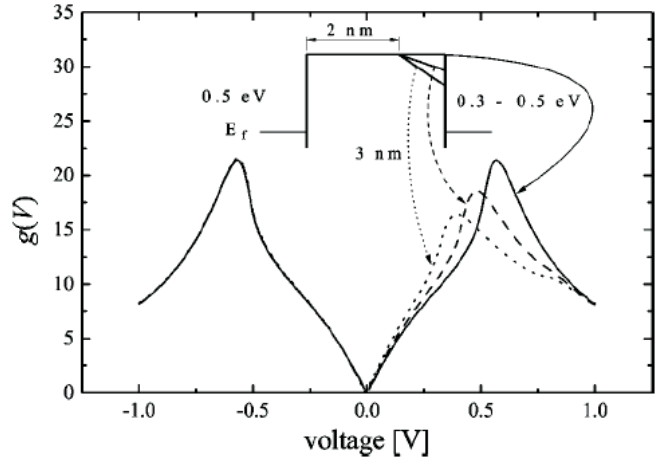

Figure 2.6: *Simulation of the logarithmic derivative $g(V)$ with a graded right interface, as shown in the inset. The position of the cusp clearly reflects the barrier height at the interface [47].*

the logarithmic derivative of conductivity based on a numerical evaluation of the tunnel equation with WKB approximation. When the central part of the junction remains at a height of 0.5eV, the height at the right interface is decreased to 0.4eV and 0.3eV. The cusps which can be found in the plot always appear at about 1.2 times the barrier height of the positively biased electrode. Consequently, the curves for negative bias voltage still remain essentially the same and for positive bias, the maximum is shifted to lower voltages. It should be noted that the barrier heights at the interface are probed, instead of the average height over the junction. Since this method reflects the barrier height directly, we have adopted this simple, physical approach to characterizing our barrier heights in this thesis.

2.4 Spin-polarized tunneling

The tunneling introduced above occurs in the non-magnetic metal /insulator /non-magnetic metal junctions. In 1970, Meservey and Tedrow et al. carried out an experiment to measure the spin polarization P of conduction electrons in magnetic metals [10]. Al_2O_3 was used as a tunnel barrier

and the polarization of the ferromagnetic electrons was detected using the Zeeman split quasi particle density of states in an Al superconductor. The experiment confirmed that the conduction electrons in magnetic metals were spin polarized and that the spin was conserved during the tunneling process. In 1975, Jullière introduced the idea to use a second magnetic metal as a spin detector [11]. The system was a Fe/α-Ge/Co magnetic tunnel junction and the tunnel conductance was lower when the magnetic moments of the ferromagnets were aligned in parallel compared to the antiparallel configuration. He also proposed a model for this effect based on spin polarization arguments.

2.4.1 Magnetic tunneling Junction

A MTJ is a junction consists of two ferromagnetic metal layers separated by a thin insulating barrier. The insulating layer is very thin that electrons can tunnel through the barrier if a bias voltage is applied between the two metal electrodes, as discussed in section 2.3. The most important property of a MTJ is that the tunneling transport is dependent on the relative orientation of the magnetization of the two ferromagnetic layers, which can be changed by an external magnetic field.

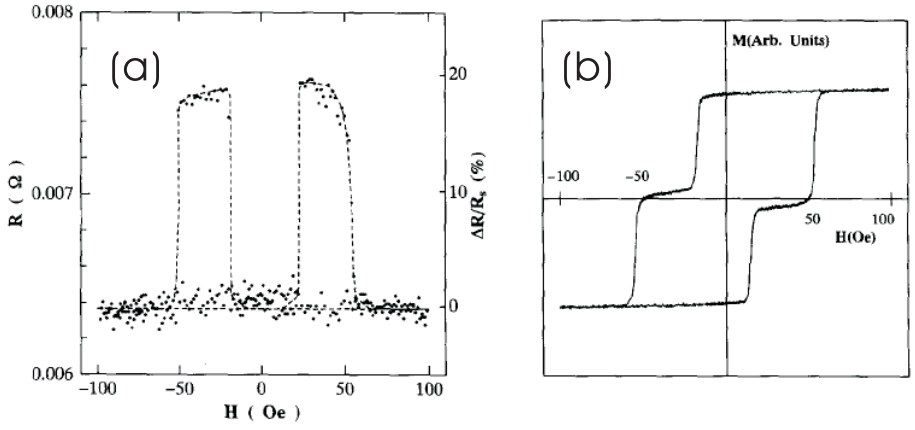

Figure 2.7: *(a) Magnetoresistance as a function of the magnetic field for Fe/Al_2O_3/Fe junction and (b) corresponding hysteresis loop [13].*

A typical hysteresis loop and magnetoresistance curve as a function of

the applied magnetic field for a MTJ is shown in Fig. 2.7. The plateaus in the hysteresis loop suggest that the ferromagnetic layers are able to be switched independently. The main change of the resistance corresponds to the plateaus in the hysteresis loop. Resistance is maximum when the magnetization of the two ferromagnetic layers is antiparallel, and is minimum for parallel alignment [13].

The phenomenon of large magnetoresistance in magnetic tunnel junctions introduced above is termed as tunneling magnetoresistance (TMR). It is defined as:

$$TMR = \frac{R_{max} - R_{min}}{R_{min}} = \frac{R_{AP} - R_P}{R_P}, \tag{2.22}$$

where R_{max} is the maximum resistance and R_{min} the minimum resistance recorded during a magnetic field sweep.

2.4.2 Jullière model

Jullière tried to propose a simple model to explain the observed changes in resistance with applied magnetic field [11]. Suppose we apply an external magnetic filed on a tunneling magnetic junction and the field is sufficiently high to saturate the ferromagnet. When the external filed is applied in one direction and subsequently reversed to the same magnitude in the opposite direction, the spin splitting of the DOS is reversed accordingly. This means that the application of an external field can also switch between majority and minority spin carriers. Based on this argument, Jullière proposed his model with two assumptions. The first was that the electron spin is conserved in the tunneling process. The second one was that the tunnel current can be divided into two separate spin channels. Spin-up electrons tunneling from one electrode are transmitted only to the spin-up band of the counter electrode and the same transport mechanism is for spin-down electrons. A simple band picture of this situation is depicted in Fig. 2.8.

From Jullière's assumptions, the current for parallel (P) and antiparallel (AP) magnetic configuration can be described as the sum of the currents in each spin channel in a similar way as for a parallel connected electric circuit:

$$j_P = j_P^{\uparrow} + j_P^{\downarrow}, \tag{2.23}$$

$$j_{AP} = j_{AP}^{\uparrow} + j_{AP}^{\downarrow}. \tag{2.24}$$

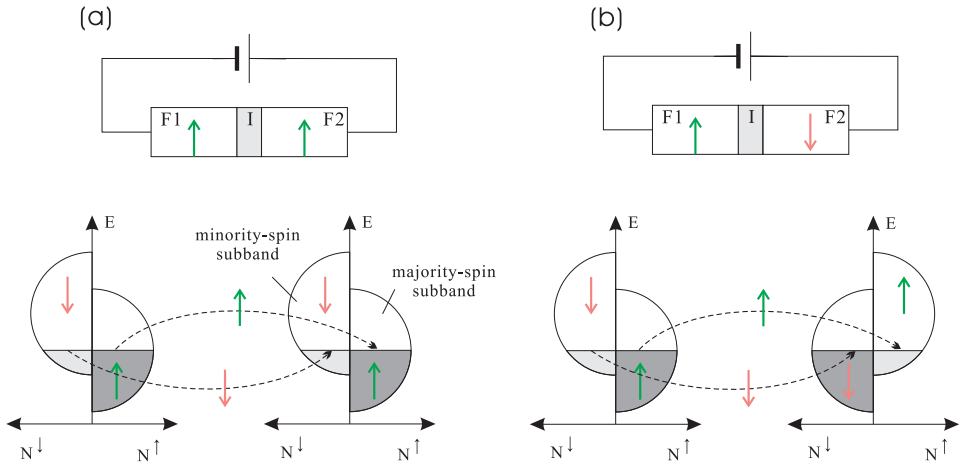

Figure 2.8: *Schematic illustration of electron tunneling in a F/I/F tunnel junction. (a) Parallel magnetic configuration: Spin-up carriers tunneling from the left electrode encounter a large number of unoccupied states in the spin-up band of the right electrode. The resistance is lower. (b) Antiparallel magnetic configuration: Spin-up carriers coming from left encounter a reduced number of unoccupied states in the right spin-up band resulting in a higher degree of scattering. The resistance becomes higher.*

A relative tunnel resistance can then be expressed as

$$\frac{R_{AP} - R_P}{R_P} = \frac{j_P - j_{AP}}{j_{AP}}, \tag{2.25}$$

where the relation $R = dV/dI$ has been used. Using the proportionality between the tunneling current and transmission coefficient T_p expressed in equation (2.8), the spin dependent tunnel currents in equation (2.23) can be written as

$$j_P \propto 16\beta^2 e^{-2\beta d}\left(\frac{\kappa_1^{\uparrow}\kappa_2^{\uparrow}}{(\beta^2+\kappa_1^{\uparrow})^2(\beta^2+\kappa_2^{\uparrow})^2} + \frac{\kappa_1^{\downarrow}\kappa_2^{\downarrow}}{(\beta^2+\kappa_1^{\downarrow})^2(\beta^2+\kappa_2^{\downarrow})^2}\right)$$
$$j_{AP} \propto 16\beta^2 e^{-2\beta d}\left(\frac{\kappa_1^{\uparrow}\kappa_2^{\downarrow}}{(\beta^2+\kappa_1^{\uparrow})^2(\beta^2+\kappa_2^{\downarrow})^2} + \frac{\kappa_1^{\downarrow}\kappa_2^{\uparrow}}{(\beta^2+\kappa_1^{\downarrow})^2(\beta^2+\kappa_2^{\uparrow})^2}\right)$$

In the limit of a high barrier $\beta >> \kappa(U_0 >> E)$, the relative tunnel current

can be reduced to

$$\frac{j_P - j_{AP}}{j_{AP}} = \frac{2(\kappa_1^{\uparrow} - \kappa_1^{\downarrow})(\kappa_2^{\uparrow} - \kappa_2^{\downarrow})}{(\kappa_1^{\uparrow} + \kappa_1^{\downarrow})(\kappa_2^{\uparrow} + \kappa_2^{\downarrow}) - (\kappa_1^{\uparrow} - \kappa_1^{\downarrow})(\kappa_2^{\uparrow} - \kappa_2^{\downarrow})}. \tag{2.26}$$

Substituting $\kappa_{1,2}^{\uparrow}$ by $N_{1,2}^{\uparrow}(E_F)$ and $\kappa_{1,2}^{\downarrow}$ by $N_{1,2}^{\downarrow}(E_F)$, which is valid for free electrons in parabolic bands, equation (2.26) becomes

$$\begin{aligned} \frac{j_P - j_{AP}}{j_{AP}} &= \frac{2(N_1^{\uparrow} - N_1^{\downarrow})(N_2^{\uparrow} - N_2^{\downarrow})}{(N_1^{\uparrow} + N_1^{\downarrow})(N_2^{\uparrow} + N_2^{\downarrow}) - (N_1^{\uparrow} - N_1^{\downarrow})(N_2^{\uparrow} - N_2^{\downarrow})} \\ &= \frac{2P_1P_2}{1 - P_1P_2}. \end{aligned} \tag{2.27}$$

The polarization P has been identified from equation (2.1). Thus the relative tunnel resistance is directly related to the polarization P_1 and P_2 of the magnetic electrodes, respectively [37]. More conventionally, the tunnel magnetoresistance ratio which is defined in equation (2.22) can be expressed as:

$$TMR = \frac{R_{AP} - R_P}{R_P} = \frac{2P_1P_2}{1 - P_1P_2}. \tag{2.28}$$

Since it is the interface polarization that is transmitted in the tunneling process, this expression might be used as a way to measure the interface polarization. Nevertheless, this should be done with caution because equation (2.28) only represents a simplified situation. In an ideal situation for the F/N/F magnetic tunneling junction with two iron electrodes, if we substitute the polarization $P = 40\%$ in the equation above, the TMR ratio of $\sim 38\%$ can be achieved.

2.4.3 Spin polarization measurement

The degree of spin polarization (P) is very important for many applications such as determining the magnitude of tunneling magnetoresistance in MTJs. However, in an actual tunneling junction, the measured polarization is not an intrinsic property, since it depends on the interface quality and the choice of the insulator material. The F/I/S junctions which were reviewed by Tedrow and Meservey et al. in 1994, established a sensitive technique for measuring spin polarization (P) of magnetic metal layers [49]. In such a junction, the Zeeman split quasi particle density of states in a superconductor was used as a detector.

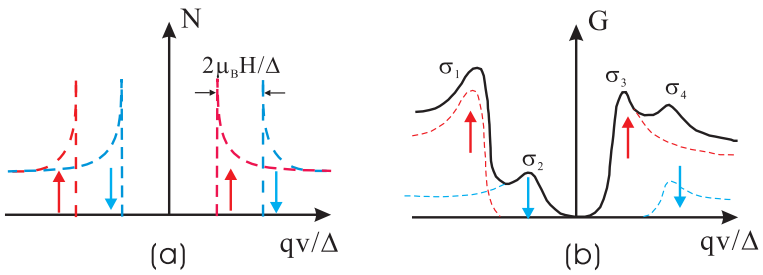

Figure 2.9: *Schematic illustration of electron tunneling in F/I/S junctions with applied magnetic field [6]. (a) Zeeman splitting of the BCS density of states as a function of applied bias. (b) Normalized spin-resolved conductance (dashed lines) and the total conductance (solid line) at finite temperature [6].*

Material	Polarization by tunneling at 0.4K (%)	
Fe	40 [49],	37 [50]
Co	35 [49],	35 [51]
Ni	23 [49],	8.5 [50]
$Co_{50}Fe_{50}$	47 [51]	
$Ni_{50}Fe_{50}$	45 [50]	

Table 2.1: *Polarization of the ferromagnets*

F/I/S tunneling conductance is shown in Fig. 2.9. For simplicity, we assume that the spin-orbit and spin-flip scattering can be neglected. Usually in such a junction, the common choice for I/S is Al_2O_3/Al. For each spin, the normalized BCS density of states is $N(E) = Re(|E|/2\sqrt{E^2 - \Delta^2})$, where Δ is the superconducting gap [6]. Because the quasiparticle energy is shifted as $E \rightarrow E \pm \mu_B H$ for spin parallel or antiparallel to the applied magnetic field H, where μ_B is the Bohr magneton, the BCS density of states is split as shown in Fig. 2.9(a). We assume the tunneling probability is different for each spin state and these values are constant within the region of interest, about 10^{-3}eV of the Fermi energy. Then, the normalized conductance is a sum of the conductance in the independent spin channels, see Fig. 2.9(b). The conductance peaks of σ_1, σ_2, σ_3 and σ_4 are defined on the diagram and

can be used to determine the polarization of the ferromagnet after equation

$$P = \frac{(\sigma_4 - \sigma_2) - (\sigma_1 - \sigma_3)}{(\sigma_4 - \sigma_2) + (\sigma_1 - \sigma_3)}. \tag{2.29}$$

Based on this technique, the spin polarization at the Fermi level in the ferromagnet could be determined. In the theoretical analysis, we assume that the spin-orbit and spin-flip scattering can be neglected. However, the actual measurement is sensitive to the fabrication processes. In particular, scattering sites in the barrier or interface can cause spin-flips and reduce the measured polarization. Table 2.1 shows the polarization values from literatures, a range of values have been observed for each ferromagnetic material.

Chapter 3

Device fabrication and test technology

In order to realize transport experiments through an epitaxial GaAs layer, ferromagnetic metal-semiconductor hybrid structures were prepared. The epitaxial growth of metals on semiconductors, for example Fe on GaAs, is well established [52]. However it is still a big challenge to grow semiconductors on metal substrates. In this work, we adopt the technology which was developed by Stephan Kreuzer [53] to sandwich the GaAs semiconductor layer between two ferromagnetic layers by chemical etching and epoxy bonding.

The fabrication technology which is called EBASE (epoxy bond and stop-etch) technique [54] and measurement methods employed during the course of this work are introduced in this chapter. Since the fabrication of a spin injection device is very similar to the magnetic tunneling junction, here we only discuss the growth steps of Fe/GaAs/Fe MTJs. The sample structure is introduced in section 3.1. Process flow is shown in section 3.2. The critical procedures for the device fabrication are then considered, followed by lithography, wet chemical etching, deposition of metal films, lift-off and epoxy bonding. Finally, the device measurement methods are introduced in section 3.4.

3.1 Semiconductor wafer

The semiconductor wafers in our experiments are grown by molecular beam epitaxy (MBE). MBE is a refined form of vacuum evaporation [55]. The molecular beams are produced by evaporation or sublimation from heated liquids or solids which are contained in crucibles. At the pressures used in MBE equipment, beams from various sources collide and interact chemically on the substrate to form an epitaxial film. Controlling the shutters attached to the vapor containing crucibles allows to start and stop a molecular beam in less than the time taken to grow a monolayer, which leads to the ability to produce complex multilayer structures with atomic precision.

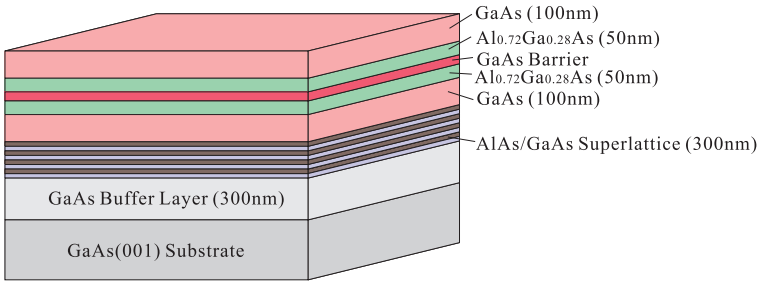

Figure 3.1: *Epitaxial structure of the wafers for the magnetic tunneling junctions. The tunneling barrier of GaAs is sandwiched between two double layers of 50nm AlGaAs and 100nm GaAs. The 300nm thick AlAs/GaAs superlattice acts as an etch stop layer.*

The wafers with epitaxial heterostructures for the device fabrication are grown on semi-insulating (SI) GaAs(001) substrates at a growth temperature of 630°C. The epitaxial structure of the wafer is shown in Fig. 3.1. A 300nm GaAs buffer layer is deposited first, followed by a digital superlattice consisting of 106 double layers of 0.57nm GaAs and 2.26nm AlAs, acting as an 300nm thick sacrificial $Al_xGa_{1-x}As$ etch stop layer with an Al content of 0.8. Finally the thin GaAs barrier is sandwiched between two 50nm $Al_{0.72}Ga_{0.28}As$ films and 100nm GaAs. The 50nm AlGaAs layer is used as a second etch stop layer, and the 100nm GaAs layer grown on top is to provide further stabilization and to prevent the thin GaAs barrier from oxidation. The function of the etch stop layers are discussed in section 3.3.2.

3.2 Process flow

The process flow of the fabrication of MTJs is introduced in this section. Fig. 3.2 shows the major processing steps schematically. The fabrication starts with the wafer which has been chemical-mechanically polished down to 150 μm. A lithography and selective etching step is followed by metal deposition and a lift-off procedure as shown in step (b) and (c) of Fig. 3.2. In these two steps, the first ferromagnetic metallic contact layer is deposited on the GaAs barrier surface. Then, the sample is epoxy bonded upside down onto a new SI GaAs(001) host substrate in step (d). The second metal contact is deposited after selectively etching the window into the insulating 100nm GaAs and 50nm AlGaAs, see step (e) and (f). Finally the mesa etching provides access to the first contact in step (g). The structure of the whole tunneling magnetic junction is shown in the last drawing (h). The detailed procedure and process parameters are discussed below and summarized in details in appendix A.

3.3 Critical processes in fabrication

In this section, the critical processes which affect the major quality of the tunneling junction are described. These start with a description of the lithography, chemical etching and carry through to the techniques of metal deposition and epoxy bonding. The selective etching which is the key process of EBASE technology is also emphasized here.

3.3.1 Photolithography

Photolithography is a technology to pattern the wafer surface for selective removal of a thin film or to define the exact dimensions of circuits. Although e-beam lithography provides the possibility to produce finer structures, this work involved only conventional photolithography using an ultra violet (UV) light source. In the course of this work, we use positive photoresist of Shipley 1805 for photolithography, which contains large amounts of sensitizers that dramatically slows down the dissolution rate of the resist in an alkaline developer. Since this sensitizer breaks down when exposed to UV-light, the exposed resist can then be removed using a developer solution.

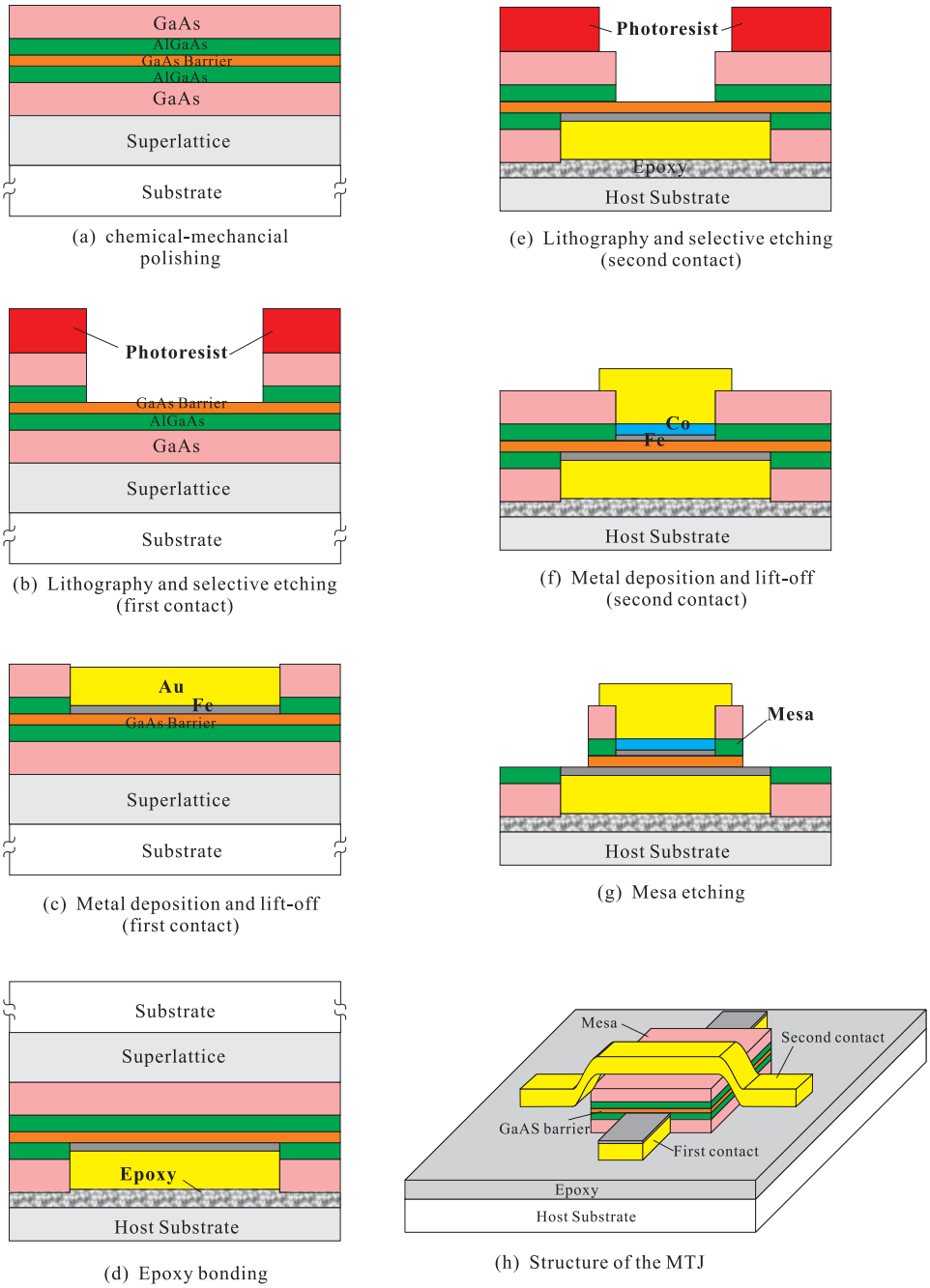

Figure 3.2: *Graphical summary of the major processing steps in the formation of a MTJ*

Purpose	Photomask	Exposure (sec)	Develop (sec)
Etching	Glass	11	40
	Plastic film	45	40
Liftoff	Glass	20	75
	Plastic film	120	75

Table 3.1: *List of lithography parameters*

In the first step, the samples are cleaned using acetone and propanol to remove any dirt and organic traces. The top surface of the wafer is then coated using a spinner with photoresist. The wafer is spun at the high speed of 4500rpm for 30 seconds to produce a thin uniform coating. In this case, the thickness of the photoresist is approximately 370nm. After spin coating, a short 'soft bake' at a temperature of 90°C for 2 minutes is performed to drive solvents out of the resist and to improve surface adhesion. The next step is to expose the resist through a mask using UV-light. The mask here is a glass plate coated with Cr, which is containing a copy of the pattern that blocks the UV-light. The last step is development, where the pattern exposed to UV-light is dissolved by Microposit 351 developer solution. Now, the remaining pattern on the wafer can be used for etching or deposition of a metallic layer.

The exposure and developing times of the photoresist are critical points for lithography, which depend on the photoresist material, photomask and purpose of the lithography. For the quick run samples, silver-halide plastic films which were exposed by laser beams are used as the photomask. The resolution of this kind photomask is typically 10μm. Since the film absorbs more UV energy, the exposure time should be much longer than that using a glass mask. Details of the lithography parameters are listed in Tab. 3.1.

3.3.2 Wet chemical etching

Wet chemical etching processes are an important part of semiconductor devices fabrication. In its simplest mode, chemical etching involves the dissolution of the material and the dissolved species have no changes in the chemical nature. Factors affecting etch rates of semiconductors include crystal orientations, temperature, humidity, strength of the etching solution as well as the morphology and the cleanness of the surface being etched. In

Material	Etching Solution	Etch Rate	Selectivity
GaAs	10 Citric Acid : 1 H_2O_2	210nm/min	yes
	1 NH_4OH : 3 H_2O_2	7.4 μm/min	no
	5 NH_4OH : 95 H_2O_2	8-9 μm/min	partially
$Al_{0.72}Ga_{0.28}As$	HF Acid (1%)	>150nm/min	yes
AlAs/GaAs supperlattice	HF Acid (10%)	>300nm/min	yes

Table 3.2: *List of chemical solutions and their approximate etch rates for wet chemical etching.*

this work, the epitaxial semiconductor layers on SI GaAs substrate have to be defined by window etching in order to deposit ferromagnetic metal on the thin GaAs barrier. In addition, the mesa etching of the stacked layers provides access to the bottom contact for the EBASE technique and leads to electrical isolation. Table 3.2 lists a host of chemical solutions which are used in the course of this work for various semiconductor etching.

Schematically shown in Fig. 3.2(b) is the process to reach the thin GaAs barrier by wet chemical etching. In the last step of lithography, the photoresist exposed to UV-light is dissolved in the developer solution leaving a 'window' for etching. The sample is first dipped in HCl (37%):H_2O=1:1 for 30 seconds to remove the native oxide. The 100nm GaAs layer is etched away by citric acid:H_2O_2 ($\sim$35%)=10:1 solution, the etching stops automatically on the surface of the underlying AlGaAs layer because of the selectivity of the etchant. The 50nm AlGaAs layer is then removed by 1% HF acid. The acid does not attack the GaAs barrier, leaving it for metallic evaporation and sputtering.

After the epoxy bonding of the sample with upside facing down to a new host GaAs substrate, the etching for the second contact is more complicated, see Fig. 3.2(d) and Fig. 3.2(c). Because the etch rates of highly selective etch solution is very low, we use a multistep etch process to remove the original GaAs substrate. A fast etch which provides fairly smooth surfaces is done in NH_4OH:H_2O_2 ($\sim$35%)=1:3 solution with an etch rate of 7.4μm/min. The mixture should be cooled in a water bath to prevent a violent exothermic reaction and stirred slowly to avoid gas bubbles sticking onto the sample surface. The etch process is stopped by etching time control at a distance of

about 30μm from the first sacrificial layer, the AlAl/GaAs superlattice. To reach the AlAs/GaAs superlattice layer a solution of NH_4OH:H_2O_2=5:95 is used. It has a high etch rate of about 8–9 μm/min and is selective to GaAs, but the selectivity is not sufficient to etch the GaAs completely without damaging the etch stop layer. The sample has to be removed from the etch solution immediately after reaching the sacrificial layer at some point (the color of the sample surface changes), which can be controlled easily by eye. The remaining parts of the GaAs substrate and GaAs buffer layer are then etched away by the high selective etchant of citric acid and hydrogen peroxide mixture solution, which takes on the order of 1-2 hours. Etching stops on the AlAs/GaAs superlattice, which can be removed by 10% HF acid [56].

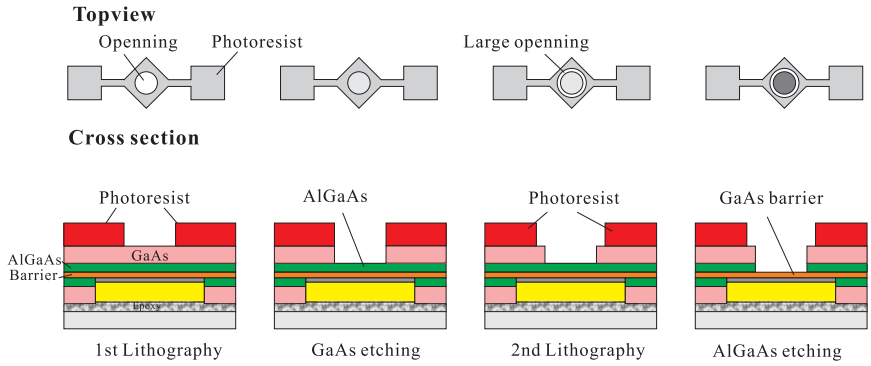

Figure 3.3: *Two-step etching of GaAs and AlGaAs before second contact deposition*

The etching process of the last 100nm GaAs and 50nm AlGaAs layers are described below. In order to protect the ferromagnetic layer of Fe from the attack of the chemical solution in the remaining processes, two-step etching is used here, see Fig. 3.3. After development of the photoresist, a small circle window ($\phi = 100\mu$m) is opened. The 100nm GaAs is etched away by a mixture solution of citric acid and hydrogen peroxide, just like the etching for the first metallic contact. Then the second exposure and development step is made again to open a large window, as can be seen in the top view of the sample in Fig. 3.3. The 50nm AlGaAs is then removed by dilute HF acid leaving the barrier for the metal deposition. The large opening in this process ensures that the edge of the ferromagnetic metal layer on the GaAs

barrier is covered by the later deposited Au film for electrical contact. The Au layer protects the ferromagnetic metal from attack by other chemicals in subsequent processes.

Selective etching

In the EBASE technology of this work, one of the key points is to etch away the 100nm GaAs and 50nm AlGaAs protective layers leaving the thin barrier not attacked to be sandwiched between two ferromagnetic metal layers. This achieved by the selective etching processes.

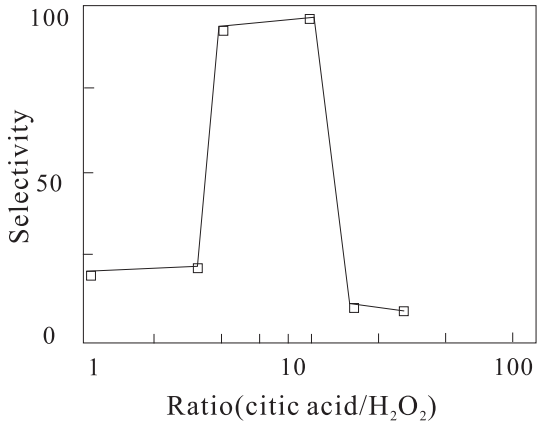

Figure 3.4: *Selectivity vs. volume ratio of citric acid to hydrogen peroxide [57].*

Selective etching refers to the different etch rates of the chemical solution between different materials to be etched. The selective etching of GaAs leaving AlGaAs not attacked is achieved by the citric acid and hydrogen peroxide mixture, where AlGaAs works as the etching stop layer. Fig. 3.4 shows the etching rates and selectivity for various ratios of citric acid/hydrogen peroxide. In this figure, the selectivity of the solution is defined as the ratio of the etching rates of GaAs to AlGaAs. When the citric acid-hydrogen peroxide mixture with a ratio of 10:1 is used, the etching rate is 210nm/min for GaAs and approximately 2.2nm/min for $Al_{0.3}Ga_{0.7}As$, hence the selectivity achieved is around 100 [57]. On the other hand, selective etching of AlGaAs leaving GaAs not attacked is done by HF acid. The etch rate of $Al_xGa_{1-x}As$ layer with an Al content of 0.4 in concentrated HF acid (48%)

is very slow, which is only around 1.5Å/hour at room temperature. And the etch rate for the pure GaAs layer is yet even slower. By contrast, an increase in aluminium concentration increases the etch rate by many orders of magnitude, hence the etching selectivity of HF acid could be $\gg 10^7$ [58].

3.3.3 Metal deposition

After completion of the mask, two different methods are used to deposit metals on the semiconductor GaAs barrier: thermal evaporation and DC sputtering.

Evaporation

Thermal evaporation is one of the most commonly used metal deposition techniques. It consists of vaporizing a solid material which is pure metal, eutectic or compound by heating it to sufficiently high temperatures and then re-condensing it onto a cooler substrate forming a thin film [59]. As the name implies, the heating is carried out by passing a large current through a filament container which has a finite electrical resistance. The shape of the container is usually a basket, boat or crucible and the choice of this filament material is dictated by the evaporation temperature and its inertness to alloying-chemical reaction with the evaporate material. This technique is also known as 'indirect' evaporation because a supporting material is used to hold the thermal evaporate species.

Once the metal is evaporated, its vapor collides with the surrounding gas molecules inside the evaporation chamber. As a result a fraction is scattered within a given distance during their transfer through the gas in the chamber. At 25°C, the mean free path for air is approximately 45 or 4500cm at a pressure of 10^{-4} or 10^{-6} torr, respectively. Therefore, pressure lower than 10^{-5} torr is necessary to ensure a straight line path for most of the evaporated species. For the distance from substrate to source, it is usually approximately 10 to 50cm in a vacuum chamber. Good vacuum is also a requirement for producing high quality deposits without any other contaminations.

An UNIVEX 550 evaporation system was used for the deposition of the metals referred to in this work. The sample is placed on a sample holder which is positioned upside down in a vacuum chamber. On the bottom of

the chamber there are source boats where different metals: iron (Fe), gold (Au) and chromium (Cr) can be put inside. The materials of the boat are tantalum (Ta) or tungsten (W) due to their high melting point. As high electrical current is passed through the boat, the material is evaporated to get deposited on the sample. The deposition of the ferromagnetic metal Fe in this work is carried out in a vacuum circumstance below 5×10^{-6} mbar with a deposition rate of 0.1–0.3Å/s. The film thickness is *in-situ* controlled by a quartz crystal microbalance. During metal deposition, the junction properties strongly depend on the velocity of evaporated particles. It is found that electron gun evaporation which produces particles with high kinetic energy will damage the thin GaAs barrier.

Sputtering

The interface quality in thermal evaporation is questionable, because the vacuum is not high enough to prevent the oxidation of the GaAs surface and the interface cannot be pretreated before deposition as well. Sputtering is now introduced to deposit ferromagnetic metal layers on GaAs barriers achieving high quality interfaces.

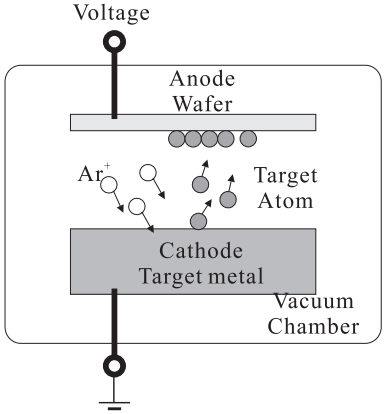

Figure 3.5: *Schematic of the DC sputtering system*

The basic principles of sputtering involves knocking an atom or molecule out of a target material using accelerated ions from an excited plasma, these knocked-out atoms or molecules subsequently condense on the substrate either in its original or in a modified form [59]. In a sputtering chamber, the

electric field accelerates electrons to collide with Ar atoms which produce Ar^+ ions and more electrons and a characteristic purple or blue plasma. These charge particles are then accelerated by the electric field where the electrons move towards the anode and the Ar^+ ions towards the cathode (for example Fe in our work). When ions knock the target, one of the effects of this impact is to eject atoms of the target, known as sputtering. Under the proper condition, the sputtered atoms will travel through space until they arrive and condense on the sample surface. Fig. 3.5 shows such a sputtering system.

The materials to be sputtered in this work are made into targets and placed at the bottom of the high vacuum chamber, while the sample is inverted and placed onto the substrate table, which is controlled by stepping motors. During deposition, the table is shifted and rotated to make the sample facing the target directly. There is a shutter which separates the target and the sample providing means of controlling the deposition thickness.

The sputtering procedure is initialized by evacuating the chamber to a pressure lower than 5×10^{-8} mbar. Ar, being a noble gas which does not react with either the target or the semiconductor sample, is then introduced into the chamber at a flux of 7sccm and a chamber pressure around 1.4×10^{-4} mbar is maintained. It was found that the higher power levels the higher kinetic energy of the deposited atoms, destroy the thin GaAs barrier. Therefore, the power for the ferromagnetic metal sputtering in this work was kept as low as 5W. In sputtering, the metal deposition is isotropic, which can cause problems in the lift-off procedure. With Shipley photoresist and careful control of the deposition thickness of the metal layer, a sharp edge of the pattern on the sample can be achieved.

Before the growth of the ferromagnetic metal contact, the surface of the substrate can be treated with hydrogen plasma in our sputtering system. The plasma is used as an efficient means to produce active hydrogen atoms. If the hydrogen atoms react with the substrate forming volatile hydride compounds, the surface of the substrate will be etched [60, 61]. In this way, the native oxide layer on the GaAs barrier in our work can be etched away in the hydrogen plasma, leaving a clean surface prior to the deposition of the ferromagnetic metals. The etching process before sputtering in this work is usually carried out in the vacuum chamber for 30 minutes. For optimal etching, H_2 gas flows into the chamber at a rate of 4sccm and a pressure

as low as $\sim 6.6 \times 10^{-6}$mbar. The discharge current for hydrogen plasma etching is 20mA for anode biases of 0.4KV (inner) and 0.6KV (external). Again high plasma powers can cause damage to the GaAs barriers.

3.3.4 Lift-off process

In the lift-off process, the photoresist is first deposited and patterned on the sample surface. The metal is then deposited on top using evaporation or sputtering. As a last step, the sample is put in a strong solvent that removes the resist. Material deposited on top of the resist is hence removed, leaving behind only the material deposited directly on the sample surface. The whole process is shown in Fig. 3.6(a). In this work, acetone is used as a solvent to remove the photoresist.

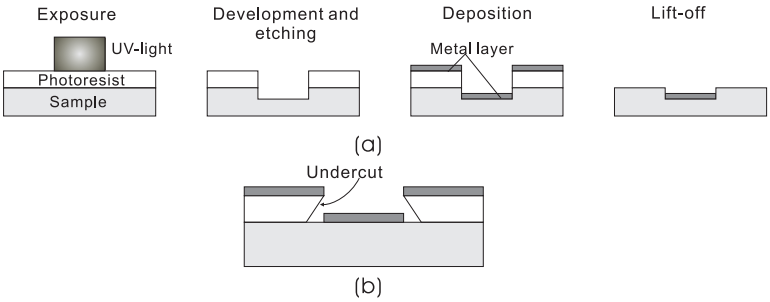

Figure 3.6: *(a)Schematic procedure of the lift-off process (b)Undercuts of the photoresist after chlorobenzene soaked and hard-baking*

The drawback of the standard process introduced above is that the photoresist may be hard to remove, if a thick or adhesive metallic layer, such as Cr was deposited. In order to improve the removal and get sharp edges of the patterns, the exposed photoresist is soaked in a chemical solution of chlorobenzene. Immediately following this treatment a 'hard bake', i.e. heating the sample for 3 min at 90°C to further increase adhesion to the sample surface and improve the resistance to the subsequent developing is performed. Such a treatment can slow the dissolution rate of the top surface of the resist resulting in undercuts after developing, which causes poor coverage of the metal on the sidewall of the photoresist and makes it easier to be immersed and swelled by acetone, see Fig. 3.6(b). For especially adhesive metallic layers on photoresist, ultrasonic agitation in warm acetone can be

used to remove resist 'ears' at the edge of a structure. However, long time ultrasonic agitations may also damage the metal layer which was deposited on the sample surface.

3.3.5 Epoxy bonding

Since the ferromagnetic metal layers are deposited on both sides of the GaAs thin barrier, the epoxy bonding process, shown in Fig. 3.2(d), is essential in EBASE technology applied in this work. After the front side processing is complete, the sample is ready to be adhered to the new host substrate by epoxy. It is important to use a new host substrate whose lateral dimensions are smaller than those of the original sample. If the new host substrate is smaller enough, the epoxy for adhesion can be squeezed out from the edges and will not interfere with subsequent backside lithographic process. In our work, the size of the host substrate is 4mm×4mm while the sample is 5mm×5mm. Mbond 600 epoxy is used as the bonding material. A small drop of epoxy is placed on the front side of the active wafer, and the host substrate is placed smooth side down on the epoxy. In epoxy bonding, gentle pressure is applied downward to the host substrate and push it back and forward forcing the layer of epoxy to become relatively thin. The sample is then baked in an oven.

It is found that the temperature for the baking should be carefully controlled. At high temperature, the iron may easily diffuse into the GaAs barrier decreasing the spin-polarized tunneling effect. Therefore, baking at a low temperature of 80°C for 4 hours is applied through the whole course of this work.

3.4 Measurement set-up

A wide range of testing techniques is used to obtain data for our spin-polarized tunneling and spin injection devices. This section outlines these methods.

Electronic measurement

Prior to the measurements, the sample is mounted on a chip carrier with PMMA and the device contact pads are wire-bonded to the chip carrier con-

tacts using gold wire. Measurements are made using a standard four-point technique. The I-V characterization set-up consists of a probe station and a Hewlett-Packard HP4155A Semiconductor Parameter Analyzer. The analyzer has programmable voltage source/monitor units (SMU) and voltage monitor units (VMU). Each SMU can be programmed to operate in three modes: voltage source or current monitor (V), current source or voltage monitor (I) and common ground (COM). Programming of the SMUs involving sweeping the voltage/current or holding these ports at a constant value allows to perform a wide range of operations on the device under test. For the HP analyzer, the maximum current which can be sourced is 100mA while the minimum measurable current is 5×10^{-13}A.

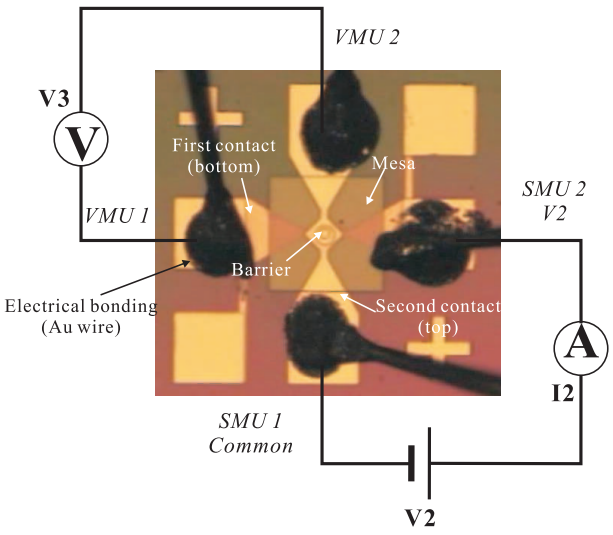

Figure 3.7: *Schematic diagram of the tunneling magnetic junction with four contacts*

A schematic diagram of the Fe/GaAs/Fe tunneling magnetic junction with four-point probes for I-V characterization is shown in Fig. 3.7. A voltage ($V2$) is applied on the top and bottom contacts, the current ($I2$) is passed through the GaAs barrier; the second set of probes are then used to measure the voltage ($V3$) drop on the junction, enabling the tunneling resistance of the magnetic junction to be obtained.

Magnetic characterization of thin films

The ferromagnetic response of the material used in this work is measured by the Superconducting Quantum Interference Device (SQUID) magnetometer. The SQUID uses the properties of electron-pair wave coherence and Josephson junctions to detect very small magnetic fields, with a resolutions down to 10^{-11}G or below [62].

Low temperature and high magnetic field measurements

The low temperature measurements are conducted in an Oxford instrument sorption pumped ^{4}He cryostat with a temperature range from 1.5K to 200K. In the cryostat the applied field B is generated by a superconducting solenoid with a range from -10T to +10T. For the measurements, the chip carrier is mounted on the variable temperature insert (VTI) and put into the cryostat. Temperature and magnetic field in the film plane are changed by a programmable controller. The I-V characterization and the magnetoresistance at low temperatures are measured by the HP analyzer.

Chapter 4

Temperature dependence of the TMR effect

The magnitude of the TMR effec in our early experiments in the Fe/GaAs/Fe junctions was very low. In order to understand this phenomenon, the temperature dependence of the spin-polarized tunneling is studied and introduced in this chapter. First we give the experimental results providing some hints to explain the low TMR effect. Next the fabrication of Fe/GaAs/Fe/Co junctions is explained and the TMR effect as well as I-V characteristics are measured at different temperatures. A theoretical model including spin dependent tunneling and spin independent tunneling to describe the temperature dependence, which was proposed by Shang et al., is introduced. Finally, we try to interpret the experimental data by this theoretical model which allows us to characterize the junction quality.

4.1 Hints for low TMR effect

The early experiments showed a TMR effect of 0.21% in the Fe/GaAs/Fe junctions [30, 53]. By optimization of the fabrication parameters and careful control of the curing temperature during epoxy bonding, the TMR ratios for barriers of varying thicknesses are measured systematically. Fig. 4.1 shows our recent measurements of the TMR effect for different barrier thicknesses. From the curve in Fig. 4.1, we find there is no obvious dependence between the TMR effect and the thickness. For the barrier thickness of 8nm, the

maximum TMR effect of 1.41% is observed under a bias of 10mV. However, this ratio is still much smaller than the value predicted by the Jullière's model as outlined in section 2.4.2.

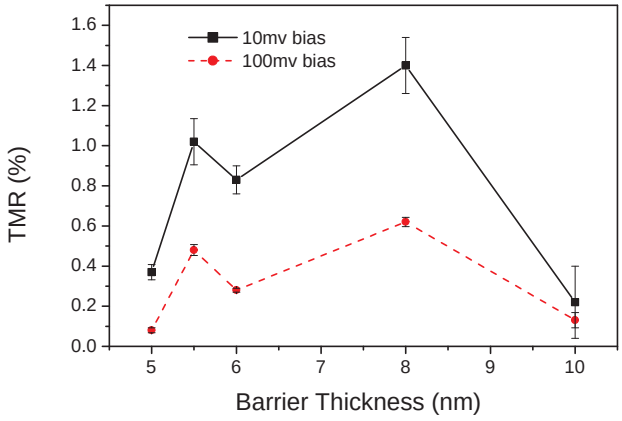

Figure 4.1: *TMR ratio at 4.2K as a function of GaAs barrier thickness for Fe/GaAs/Fe junctions. The measurements are carried out under a bias of 100mV and 10mV, respectively. Curves are only a guide to the eye.*

In order to improve the TMR effect, the ferromagnetic film in the junctions was also grown by metal-MBE. As mentioned in the last chapter, the sacrificial and stop-etching layers on the GaAs barrier are removed by wet chemical etching before the growth. Argon plasma etching and high temperature annealing was used as the pre-treatment to obtain a clean and flat surface for the MBE growth. However, no TMR effect could be detected in these experiments. This was probably due to destruction of the thin barrier by the pre-treatment. Based on this, a step backwards was taken. Fig. 4.2(a) shows the TMR effect of tunneling magnetic junctions, whose ferromagnetic metal layers are deposited by MBE on the GaAs barrier without any pre-treatment. For comparison, the TMR effect of the junction with thermal evaporation is also shown in this figure. The TMR effect increases from 0.28% to 0.74% (still less than 1%) for the barrier thickness of 6nm under a bias of 100mV at the measurement temperature of 4.2K. This experimental finding indicates that even growth of the ferromagnetic layer in a high vacuum system, the TMR ratio can not be improved significantly.

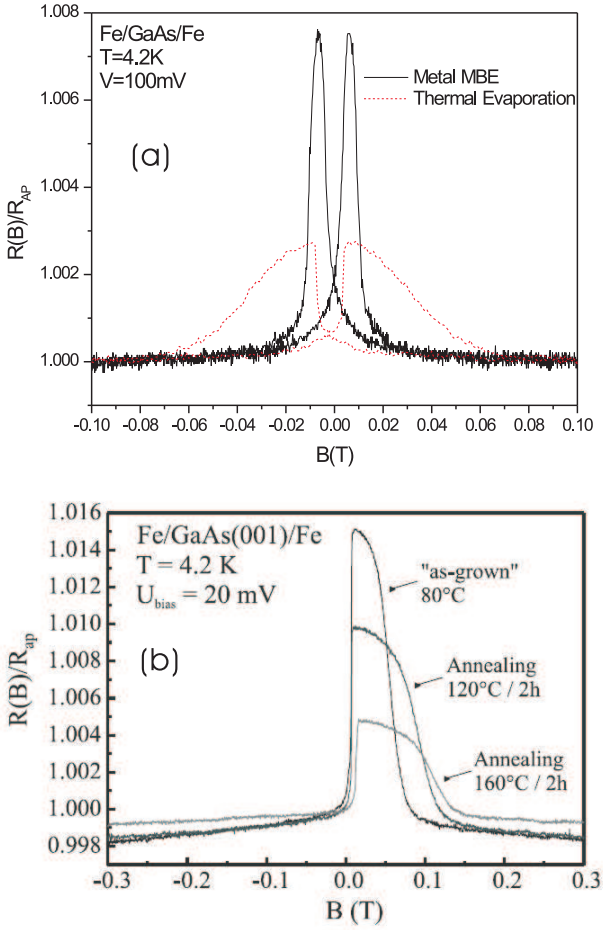

Figure 4.2: *(a) Magnetoresistance versus magnetic field for MTJs in which ferromagnetic metal layers are grown by MBE and thermal evaporation, respectively. (b) Magnetoresistance decreases after annealing [31].*

Annealing experiments in Fe/GaAs/Fe junctions have been discussed by Zenger et al. [31], see Fig. 4.2(b). The initial value of the TMR effect was around 1.4%, and it decreased to 1.0% after the annealing at 120°C for 2h. A second annealing step at 160°C for 2h led to a further decrease of the TMR ratio to 0.4%. After a last annealing step carried out at 200°C for 2h, the TMR effect vanished completely. In addition, a significant reduction of the

resistance of the tunnel junction after annealing was also observed where the resistance was only 10% of its initial value after the three steps of annealing. The sensitivity of the TMR effect in the annealing experiments indicates that the layer intermixing or impurity interdiffusion plays an important role in such tunnel junctions.

In order to understand the low TMR effect in such structures, and the relevant transport mechanisms across ferromagnet-semiconductor interfaces, the temperature dependence of TMR effect is studied and discussed in this chapter. A theoretical model including two current contributions has to be taken into account [63]. The experimental data allow us to separate transport mechanisms between direct elastic tunneling and spin-independent conductance and to characterize the Fe-GaAs interface quality.

4.2 Sample preparation and test results

In the previous experiments on Fe/GaAs/Fe magnetic tunnel junctions, the same ferromagnetic layers (Fe) with different thickness were used [30]. When the temperature was increased, the difference of coercive fields vanished because domain walls are released from their local energy minima by thermal excitations. Thus, temperature dependent phenomena could not be studied. In this work, we try to use an additional Co layer to magnetically bias one of the Fe films [64] and measure the temperature dependence of the magnetoresistance in Fe/GaAs/Fe/Co tunneling junctions.

In order to fabricate the Fe/GaAs/Fe/Co magnetic tunneling junction, we use the EBASE technique. Since the basic fabrication processes were introduced in the chapter 3, we only emphasize some special steps below. After the 100nm GaAs and 50nm AlGaAs layers are selectively removed by the citric acid and 1% HF respectively, a 12nm Fe layer was sputtered on the GaAs barrier as a soft-magnetic electrode at a pressure of $< 5 \times 10^{-8}$mbar. The deposition rate was 2.6Å/min. For the second contact, a 12nm Fe layer was sputtered on the other side of the GaAs barrier. After the deposition of Fe, a 50nm Co layer was sputtered to pin the Fe layer so that different coercivities of the two magnetic electrodes could be obtained. Due to the extreme selectivity of HF ($\geq 10^7$), the tunneling barrier thickness of the junction is precisely defined by MBE growth only [58]. After the sample fabrication, the electric and magnetotransport properties of the junction

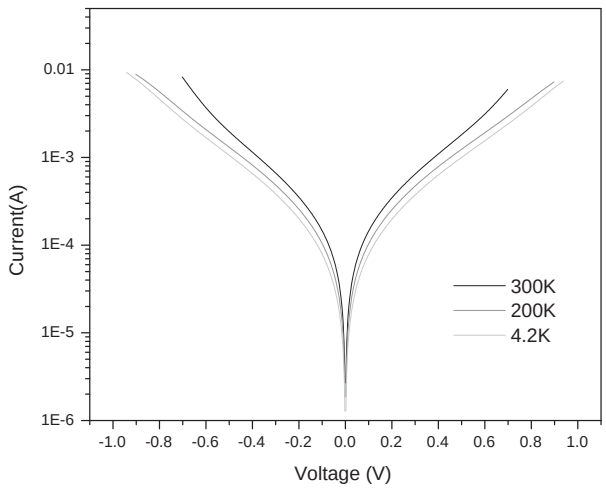

Figure 4.3: *I-V characteristics of a Fe/GaAs/Fe/Co magnetic tunnel junction with a barrier thickness of 8nm. Measurements are taken at 300K (black), 200K (gray) and 4.2K (light gray), respectively.*

have been studied at various temperatures.

Fig. 4.3 shows the *I-V* measurement results of the Fe/GaAs/Fe/Co tunneling junction with a 8nm GaAs barrier. The *I-V* characteristics show a pronounced nonlinear behavior, which can be attributed to tunneling. Fig. 4.4a shows the magnetic hysteresis loops at 4.2K and 100K for the Fe/GaAs/Fe tunnel junction using a Co layer to magnetically bias one of the Fe films. The magnetization of the two Fe layers reverse direction separately, with coercive fields ∼25Oe for the Fe itself and ∼300Oe for the Fe with Co pinning. In the magnetic field range between these coercivities, the ferromagnets' magnetizations can be switched to anti-parallel. In Fig. 4.4(b), a series of magnetoresistance curves of these MTJs versus the applied magnetic fields under 20mV applied voltage at different temperatures are shown. As the applied magnetic field increases from the negative saturation field to the positive saturation field, one can notice an increase (or decrease) of the resistance at the magnetic filed of 25Oe (or 300Oe). It coincides reasonably well with the magnetization reversal of the soft layer from the parallel (P) to the antiparallel (AP) configuration with respect

to the magnetization of the hard magnetic layer, showed as the plateaus of the magnetic hysteresis loops in Fig. 4.4(a). As showed in Fig. 4.4(b), with increasing temperature, the TMR ratio decreased from 1.41% at 4.2K to 1.00% at 100K. The resistance of the tunneling junction is found to decrease when the temperature is changed, from 1712Ω at 4.2K to 1437Ω at 100K.

4.3 Temperature dependence model of the TMR effect

Different mechanisms have been proposed to describe the temperature dependence of the TMR effect in recent years [14,65,66]. The model proposed by Shang et al. includes several important factors which is used to interpret the temperature dependence of the spin-polarized tunneling [63]. According to Shang's work, the Jullière model has to be modified by assuming that in addition to the conductance due to direct elastic tunneling, a second spin independent conductance G_{SI} is present. The total conductance is then:

$$G(\theta) = G_T[1 + P_1(T)P_2(T)\cos(\theta)] + G_{SI}, \tag{4.1}$$

where θ is the angle between the direction of magnetizations in the two electrodes, e. g., $\theta = 0\,^\circ$ for parallel and $\theta = 180\,^\circ$ for anti-parallel magnetic configuration, respectively. G_T is the pre-factor for direct elastic tunneling, while P_1 and P_2 denote the effective electron spin polarizations of the two ferromagnets. With regard to temperature dependence in equation (4.1), there are three candidates: G_T, $P(T)$ and G_{SI}.

First, the temperature dependence of G_T is considered. As discussed in section 2.3.4, the elastic direct tunneling varies with T due to broadening of the Fermi distributions in the electrodes. From equation (2.19), one can obtain

$$G_T = G_0 CT/\sin(CT), \tag{4.2}$$

where G_0 is a constant and C is expressed as

$$C = 1.387 \times 10^{-4} d/\sqrt{\phi}. \tag{4.3}$$

In equation (4.3), the barrier width(d) is given in Å and the barrier height(ϕ) is given in eV [45,46]. Second, the variation of electrode polarization is considered. Magnetization versus temperature has been extensively studied,

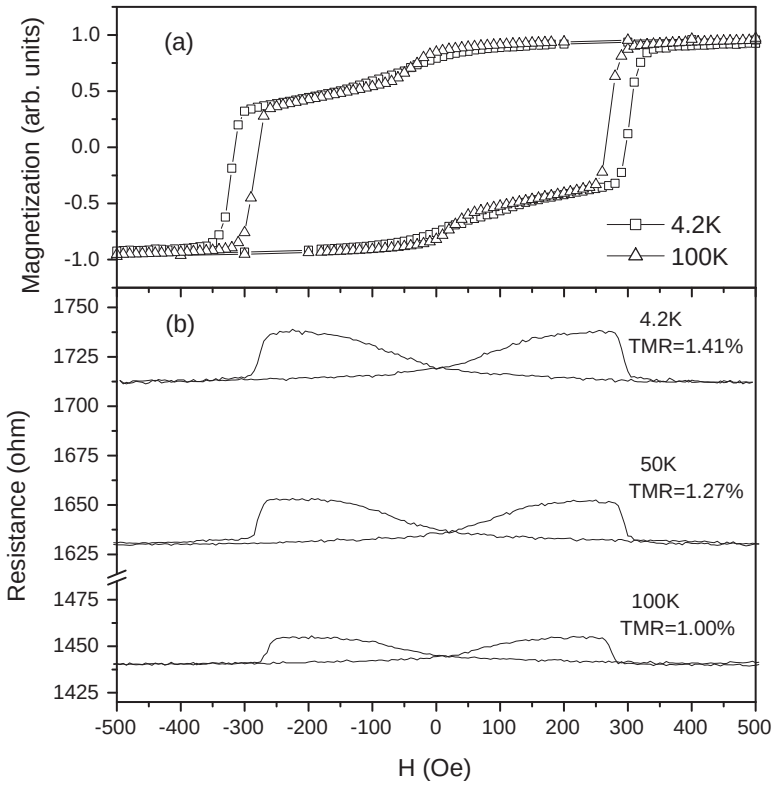

Figure 4.4: *(a) SQUID magnetization measurements of the Fe/GaAs/Fe/Co magnetic tunnel junction at 4.2K and 100K. With the pinning of the Co layer, the coercivity of the Fe layer changed from 25Oe to 300Oe at 4.2K. The coercivity of the Fe layer was decreased to 250Oe when the temperature increased to 100K. (b) Magnetoresistance of the junction plotted as a function of the magnetic field in the film plane with an applied voltage of 20mV at different temperatures.*

and is described fairly well by Bloch's law for temperature far below the Curie temperature. This produces a term proportional to $T^{3/2}$ in the magnetization, which has been experimentally confirmed for bulk samples, ultrathin films, and surface magnetization as well [67–69]. Thus, the polarization

can be expressed as

$$P(T) = P_0(1 - \alpha T^{3/2}), \tag{4.4}$$

where P_0 is the spin polarization of the electrodes at $T = 0$K. The material-dependent spin wave parameter α is different for bulk samples or surfaces, and is generally larger for the latter due to surface exchange softening. It has also been observed that both P_0 and α are very sensitive to surface contaminations [49]. Third, the spin-independent conductance G_{SI} is assumed by Shang et al. to be a function of T, of the form:

$$G_{SI} = ST^{\gamma'}. \tag{4.5}$$

It depends on S and γ' constants, which are related to hopping processes and the number of defects in the barrier.

4.4 Experimental data analysis

In order to interpret the temperature dependence of the magnetoresistance and to analyze the interface quality between ferromagnetic metals and semiconductors, the resistances of the tunneling junction with parallel and antiparallel configuration measured at different temperatures are used.

With equation (4.1), the TMR can be described as

$$TMR = \frac{G_{max} - G_{min}}{G_{min}} = \frac{2P^2(T)}{1 - P^2(T) + G_{eff}}, \tag{4.6}$$

where $P_1(T) = P_2(T) = P(T)$ is assumed since the same Fe electrodes are used in our tunneling junctions. G_{max} and G_{min} are the conductances at parallel and anti-parallel configurations, respectively. And G_{eff} is defined as

$$G_{eff} = G_{SI}/G_T. \tag{4.7}$$

Thus, for the non-vanishing G_{SI}, the TMR ratio is always smaller than the value predicted by Jullière. In order to analyze the temperature dependent of magnetoresistance, all the parameters of G_{eff} and $P(T)$ in equation (4.6) should be determined.

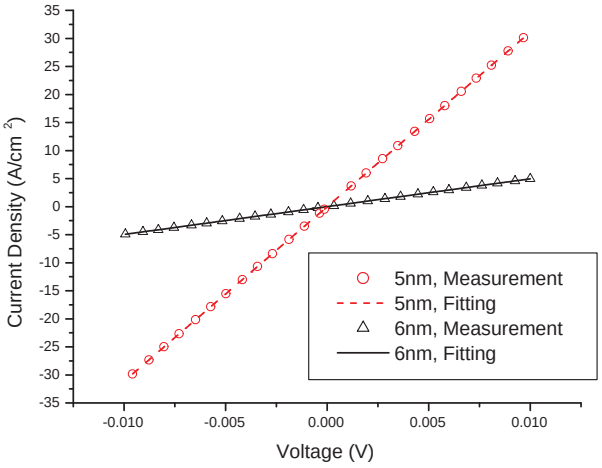

Figure 4.5: *$J(V)$ curves and Simmons fitting results of the tunneling junctions with 5nm and 6nm GaAs barriers. The $J(V)$ curves are measured at low voltage bias at room temperature.*

4.4.1 Determination of the Fe/GaAs Schottky barrier height

The conductance of elastic tunneling depends on the constant C, which is a function of the barrier width (d) and the barrier height (ϕ) described in equation (4.2). The experimental investigations of J-V characteristics on magnetic tunnel junctions can be resorted to the description WKB model, such as those of Simmons [43] and Brinkman [70] to extract barrier height. Another technique is proposed by Rottländer et al. [47, 48], which is to plot the logarithmic derivative of the conductivity plotting g against the applied voltage, as explained in section 2.3.5.

Simmons model fitting

The barrier height can be derived by fitting of the current density-voltage (J-V) curve to the Simmons formulas. Especially for low voltages, J can be expressed as a linear function of V, as described in equation (2.15) in section 2.3.4[1].

[1] In equation (2.15), the barrier width (d) is labeled as the barrier thickness of Δs

Barrier thickness after MBE(Å)	Barrier thickness from fitting(Å)	Barrier height from fitting(eV)
50	50.9	0.63
55	56.8	0.60
60	59.8	0.63
80	78.0	0.58

Table 4.1: *Schottky barrier height and thickness extracted from Simmons fitting*

The J-V curves of the magnetic tunnel junctions with various GaAs barrier thickness are shown in Fig. 4.5. We performed a fit of the $J(V)$ response measured at room temperature according to the Simmons model. Two adjustable parameters are used in the fit: the barrier height (ϕ) and the effective barrier width (d). The fitting results are also shown in Fig. 4.5 as the dashed and solid lines. The detailed parameters of the other magnetic tunnel junctions are listed in table 4.1. The effective barrier thicknesses are very similar to the nominal GaAs thicknesses grown by MBE, due to the high selectivity of the chemical etchant mentioned in last chapter. The barrier height varies from 0.58eV to 0.63eV, which may be caused by different surface conditions.

Logarithmic plotting

The barrier height and barrier thickness extracted from the Simmons model are always correlated and the independent evaluation of one of these parameters is impossible. As introduced in section 2.3.5, the logarithmic derivative of the I-V curves provides an alternative access to extract the height of tunnel barriers in magnetic tunneling junctions.

The I-V curve of the magnetic tunnel junction with a 8nm GaAs barrier measured at room temperature is shown in Fig. 4.6. In order to get the barrier height, we also plot the logarithmic derivative of the conductivity g against the applied voltage in the figure, where $g(V) = d\ln[I(V)/V]/dV$. It was shown that the $g(V)$ curve produces a cusp at a voltage of about 1.2 times the barrier height of the positively biased electrode [47]. In Fig. 4.6, a cusp can be seen at a voltage around 0.73V ($\phi = 0.61$eV), when Fe-GaAs is positively biased. The barrier height derived here is almost the same as

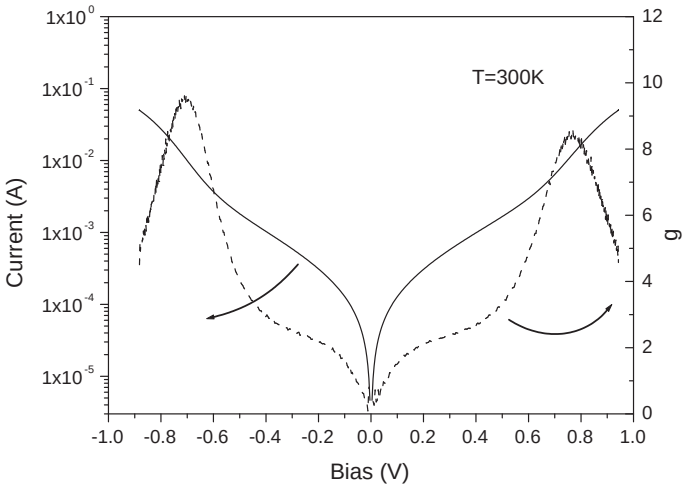

Figure 4.6: *I-V curve (solid line) measured at $T = 300K$ on the Fe/GaAs/Fe/Co tunnel junction. The barrier height is determined by means of the $g(V) = d\ln[I(V)/V]/dV$ curve (dashed line). Since the position of the cusp of $g(V)$ curve corresponds to the barrier height at the Fe-GaAs interface, one finds a barrier height for this sample of 0.61eV.*

the value extracted from Simmons fitting. If we substitute $d = 8$nm and $\phi = 0.61$eV in equation (4.3), the constant $C = 1.41 \times 10^{-2}\mathrm{K}^{-1}$ for the tunneling magnetic junction is obtained.

4.4.2 Determination of $P(T)$ and G_{eff}

In order to analyze the temperature dependence of magnetoresistance using the theoretical model, we try to determine the parameters G_0 and P_0 first. From equation (4.1), we find for $T = 0$K that G is only proportional to the two ground-state parameters G_0 and P_0, where

$$G_{max}(0) = G_0(1 + P_0^2), \tag{4.8a}$$

$$G_{min}(0) = G_0(1 - P_0^2). \tag{4.8b}$$

The Maximum and minimum conductance values versus temperature are plotted in Fig. 4.7. The low temperature measurements allow us to extrap-

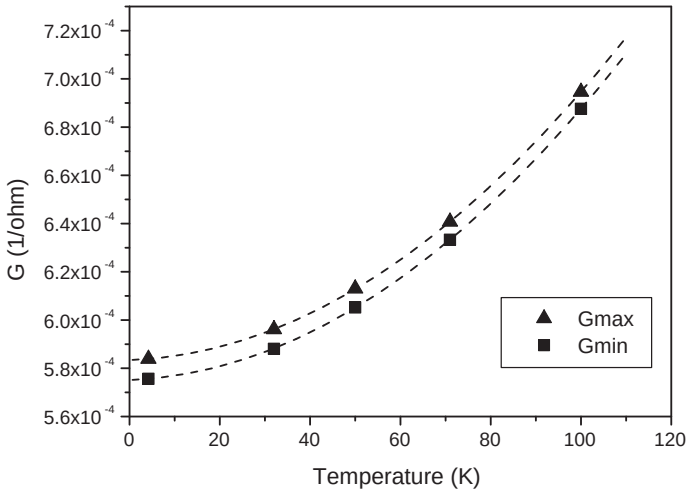

Figure 4.7: *Maximum and minimum conductance of a MTJ versus temperature. Dashed lines are fitted to the experimental data to extract the parameters G_0 and P_0.*

olate both the minimum and maximum conductance to $T = 0$K and we obtain $G_0 = 5.79 \times 10^{-4} \pm 9.41 \times 10^{-8}\Omega^{-1}$. The spin polarization (P_0) of the Fe film is $8.44 \pm 0.01\%$.

Next we consider the parameter α and the spin-independent conductance G_{SI}. We notice that $\Delta G = G_{max} - G_{min}$ does not contain G_{SI} and $G_{av} = (G_{max} + G_{min})/2$ does not contain $P(T)$ as well. For our barrier parameters, according to equation (4.2), G_T at $T = 100$K is only a few percent higher than at $T = 0$K. To a good approximation, G_T can be assumed as a constant G_0. Consequently, ΔG and G_{av} can be written as:

$$\Delta G(T) = 2G_0[P_0(1 - \alpha T^{3/2})]^2, \tag{4.9a}$$

$$G_{av} = G_0 + ST^{\gamma'}. \tag{4.9b}$$

Examination of equation (4.9a) reveals that a plot of $(1-\sqrt{\Delta G/2G_0}/P_0)$ vs. $T^{3/2}$ should be a straight line of slope α. Such a plot for the junction under study is shown in Fig. 4.8a and leads to the spin wave parameter α of $8.0 \pm 0.2 \times 10^{-5}\mathrm{K}^{-3/2}$. Similar analysis is applied for equation (4.9b). A plot

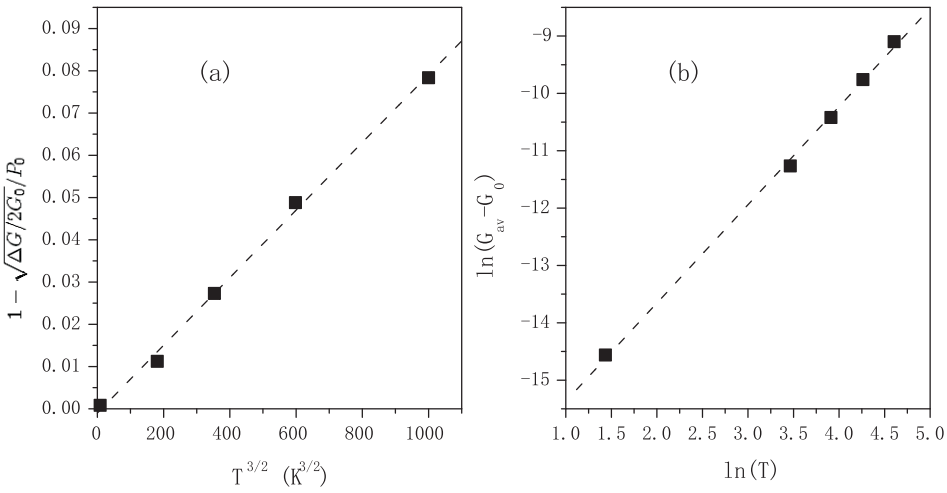

Figure 4.8: *(a) The* $(1-\sqrt{\Delta G/2G_0}/P_0)$ *vs.* $T^{3/2}$ *plot for a Fe/GaAs/Fe /Co MTJ. (b) The logarithm of* $(G_{av}-G_0)$ *as a function of* $\ln(T)$ *for the same junction. The dashed lines represent linear fittings to obtain the spin wave parameter* α *and the parameters* S *and* γ'*.*

of the logarithm of $(G_{av}-G_0)$ as a function of $\ln(T)$ is shown in Fig. 4.8b. The experimental data were fitted with a linear function, as indicated by the dashed line, yielding $S = 3.86 \pm 0.56 \times 10^{-8}\Omega^{-1}\mathrm{K}^{-\gamma'}$ and $\gamma' = 1.71 \pm 0.04$.

The temperature dependence of TMR is shown in Fig. 4.9. The theoretical curve (solid line) with the parameters obtained as described above is also plotted in this figure. It is clear that the theoretical model allows us to describe the experimental data quite well.

4.5 Discussion

The parameters to characterize the temperature dependence of spin-polarized tunneling and junction quality are summarized in table 4.2. For comparison, the values for a $Co/Al_2O_3/Co$ junction from reference [71] are also listed in the same table. The value of $8.44 \pm 0.01\%$ for the spin polarization of Fe at $T = 0K$ is much less than the value of $\sim 40\%$ expected from the band structure of Fe [36]. However, for the $Co/Al_2O_3/Co$ junction, the polarization which is obtained from the experimental data is almost the same as the ideal value for a Co layer. Moreover, we find that the spin wave related

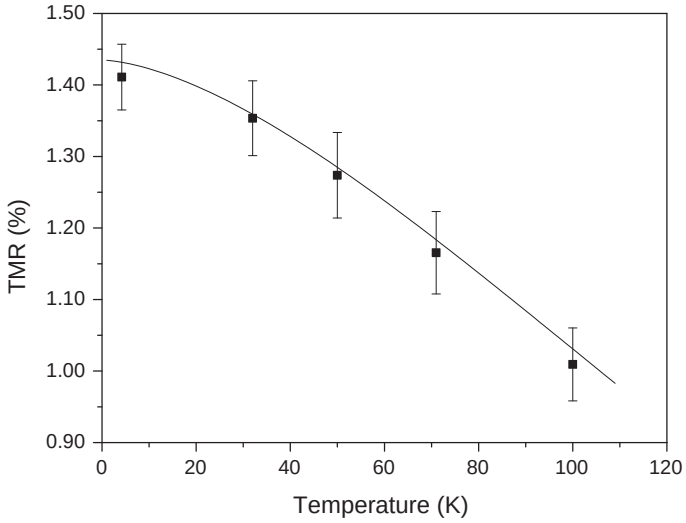

Figure 4.9: *Temperature dependence of the TMR effect of a Fe/GaAs/Fe/Co junction (squares). The solid line represents the theoretical fitting with parameters obtained.*

reduction α is almost one order of magnitude larger for bulk Fe [69]. The parameter α is responsible for the temperature dependence of the electron spin polarization at the ferromagnet's surface. It depends largely on the junction interface quality, and can be more than two times as large as the corresponding bulk value. The low spin polarization P and high value of α in our junction means a high degree of disorder at the interface resulting in a considerable decrease of P with increasing temperature. It can be explained by the oxidation of the surface of the GaAs barrier, which occurs when the sample is etched and exposed to the air before it is transferred to the sputtering chamber. Additionally, interdiffusion between Fe and GaAs occurs. When As diffuses into the Fe layer, it forms antiferromagnetic Fe_2As clusters at the interface and decreases the spin polarization of Fe [72, 73].

Next, for the spin independent part G_{SI}, we found a parameter γ' of 1.71 for the junction under study. According to the Glazman and Matveev model [74], the hopping through chains of N localized states has a power law dependence on T, as shown in equation. (4.5) with an exponent $\gamma'(N) =$

Parameters		Fe/GaAs/Fe	Co/Al_2O_3/Co [71]
$P(T)$	P_0	$8.44 \pm 0.01\%$	$32 \pm 1\%$
	$\alpha(\mathrm{K}^{-3/2})$	$8.0 \pm 0.2 \times 10^{-5}$	$1.0 \pm 0.08 \times 10^{-5}$
G_{SI}	$S(\Omega^{-1}\mathrm{K}^{-\gamma'})$	$3.86 \pm 0.56 \times 10^{-8}$	$2.0 \pm 0.5 \times 10^{-6}$
	γ'	1.71 ± 0.04	4/3

Table 4.2: *List of parameters to characterize the temperature dependence of spin-polarized tunneling and junction quality. For comparison, the values for a Co/Al_2O_3/Co junction from reference [71] are also listed here.*

$N - [2/(N+1)]$. The value for γ' was determined to 4/3 for junctions with Al_2O_3 barriers, which means that the spin independent transport is indeed dominated by a hopping process over only one intermediate trapped state. On the contrary, the value for γ' in our junction of 1.71, which leads to $N > 2$, can be attributed to the participation of more than two localized states during tunneling through the GaAs barrier [75]. These additional localized states can be caused by the diffusion of Fe into the GaAs barrier. As a consequence, the spin independent contribution to the tunneling conductance increases at higher temperatures and decreases the whole TMR effect.

Our study of the temperature dependence of the magnetoresistance in magnetic Fe/GaAs/Fe/Co junctions shows that the experimental data can be described by a model which contains direct elastic tunneling and hopping conductance via trapped states. Simulation of the experimental data employing a theoretical model allows us to characterize the junction quality and the spin polarization P, the spin wave parameter α and the spin-independent conductance G_{SI} can be extracted. The analysis suggests that apart from the conductivity mismatch problem, it is important to find an effective way to prevent oxidation of the barrier surface and interdiffusion between the ferromagnetic electrode and the semiconductor for the fabrication of high quality ferromagnet-semiconductor hybrid structure.

Chapter 5

Surface pretreatment in Fe/GaAs/Fe junctions

In this chapter we try to discuss the possibility of using surface pretreatment to improve the interface quality as well as to enhance the TMR effect in Fe/GaAs/Fe magnetic tunnel junctions. As noted in the last chapter, the temperature dependence of the TMR effect shows that the low TMR effect in our junctions can be attributed to the oxidation of the barrier surface and the interdiffusion between the ferromagnetic contact and the semiconductor barrier. In order to improve the interface quality, the surface pretreatment is applied in our experiments. The study of the epitaxial growth of Fe on the sulphur-passivated GaAs substrate is introduced here. Next we discuss the results of spin-polarized tunneling through a sulphur-passivated GaAs barrier. Using hydrogen plasma etching to improve the TMR effect is also briefly introduced in this chapter.

5.1 Introduction

III-V compounds, especially GaAs, are widely used in today's micro electronics. However, one of the principal problems compared to Si technology is the poor surface electronic properties due to native oxidation. Studies of Fe growth on GaAs substrates indicated also that the average film magnetization decreased dramatically at the interface. This can be explained by interdiffusion between Fe and GaAs and formation of Fe_2As clusters at the

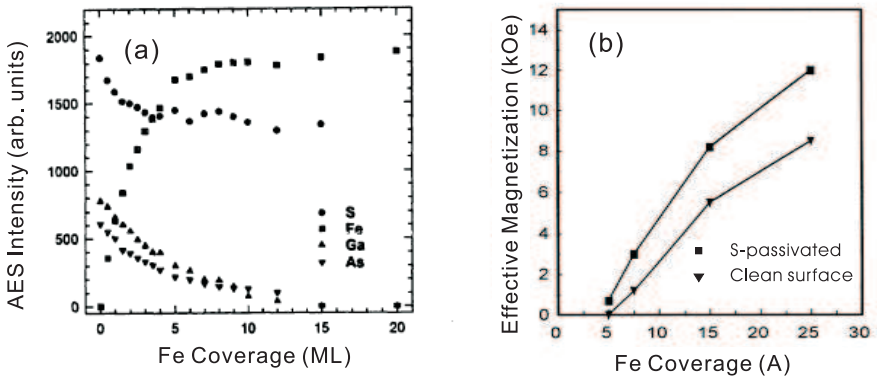

Figure 5.1: *(a) The change of the S, Ga, As and Fe concentration during Fe deposition [78]. (b) The effective magnetization as a function of the film thickness of Fe coverlayers grown on S-passivated GaAs and a clean surface [79].*

interface [73, 76].

In order to improve the magnetic properties at the interface, it is necessary to find a way to prevent As diffusion into the Fe overlayer or to inhibit the formation of Fe-As. Among various techniques for surface modification, the sulphur passivation is one of the most promising methods [77]. The *ex situ* S-passivation of GaAs surface results in the formation of a stable sulfide overlayer which gives the system remarkable stability against oxidation by air. Thus, quite a number of works have been performed on the epitaxial growth of Fe films on S-passivated GaAs substrates, with the goal to prevent interdiffusion and maintain the high quality of the interface [78, 79].

Fig. 5.1 shows the experiments attempting to grow Fe overlayers on a passivated surface. The change of the element composition in the Fe overlayer which was deposited on S-passivated GaAs suface is shown in Fig. 5.1(a). The data are measured by Auger electron spectroscopy (AES). The Fe signal increases steadily with deposition and saturates at a point of approximately 7ML. The Ga and As signals decrease exponentially, which becomes undetectable for Fe coverage larger than 15ML. This experiment suggests that neither As nor Ga will diffuse through the Fe overlayer if the GaAs substrate is S-passivated [78]. Fig. 5.1(b) shows the effective magnetization as a function of Fe coverage on S-passivated GaAs and a surface without passi-

vation. With increasing thickness, the effective magnetization also increases. For corresponding film thickness, the magnetization of the Fe layer on the GaAs without pre-treatment is much lower than that grown on S-passivated GaAs. This further verifies that S-passivation on GaAs surface can prevent the interdiffusion and increase the magnetization of the Fe overlayers [79].

Although these investigations showed that the S-passivated has the advantages to prevent the interdiffusion between the semiconductor and Fe during the epitaxial process, there is still no direct experiment has been performed to study the passivation effect in spin tunneling or spin injection.

5.2 Sample preparation

In our experiment, we use a chemical solution of $(NH_4)_2S$ to treat the semiconductor surface resulting in a S-passivated GaAs barrier. The common fabrication steps of the sample preparation are illustrated in chapter 3, only the special steps are described here.

The sulfide treatment is carried out before the evaporation of the first magnetic metal layer. After the AlGaAs protection layer has been removed, the sample is treated for 20 min at 65°C in an aqueous ammonium sulphide $(NH_4)_2S$ solution. The residual solution is removed from the sample by rinsing with de-ionized water and dry blowing with N_2 gas. Since the epoxy used in the experiments chemically reacts with a sulfide solution, only one side of the GaAs barrier is S-passivated.

5.3 Tunneling through sulphur-passivated GaAs barriers

5.3.1 Barrier height

The sample structure under studied is depicted in the inset of Fig. 5.2(b). The temperature dependence of the I-V curves are shown in Fig. 5.2(a). The tunneling current through the barrier decreases, when the temperature increases. In order to derive the barrier height of Fe/GaAs with or without GaAs pre-treatment, we also plot the logarithmic derivative of the conductivity g against the applied voltage in Fig. 5.2(b), where $g(V) = d\ln[I(V)/V)]/dV$. As we introduced in section 2.3.5, from I-V

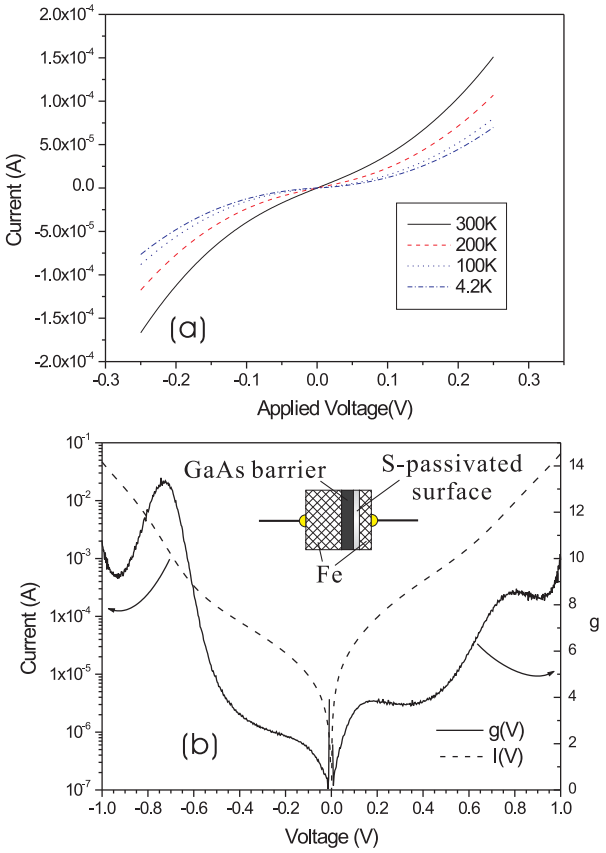

Figure 5.2: *(a) The temperature dependence of I-V characteristics on magnetic tunneling junction with 6nm S-passivated GaAs barrier. (b) I-V and $g(V)$ curves on the same junction at room temperature. The junction structure is shown in the inset. Determining the barrier height by means of the $g(V) = d\ln[I(V)/V)]/dV$ curve, one finds the barrier height of 0.62eV for Fe/GaAs and 0.67eV for the barrier with S-passivated GaAs, respectively.*

curve taken at 300K, it is possible to calculate the $g(V)$ curve. In this curve, a cusp can be seen at voltage of around 0.74V (0.62eV), when the Fe/GaAs junction without pretreatment is positively biased. It is almost the same as we find using Simmons fitting, see section 4.4.1. As the other side of GaAs

barrier was treated using the $(NH_4)_2S$ solution, a thin sulphide composite layer forms on the semiconductor surface, which can stabilize the surface states and prevent the oxidation, thus, reducing the Fermi level pinning effect [80]. Accordingly, we find the cusp shifted to a higher voltage of 0.80V when the Fe/GaAs junction with pre-treatment is positively biased. This measurement convinces the passivation of GaAs has increased the Schottky barrier height from 0.62eV to 0.67eV at the Fe/GaAs interface.

5.3.2 The TMR effect

The tunneling magnetoresistance loop of a MTJ with a passivated barrier, measured at 4.2K for an applied voltage of 100mV, is displayed in Fig. 5.3(b). For comparison, the TMR curve without passivation is also shown in the same figure. The coercive field of iron films of two different thicknesses is strikingly different. Fig. 5.3(a) shows the SQUID magnetometer result of 4nm and 20nm iron films. At low temperature, the thinner iron film can pin the domain wall more effectively and display thereform a larger coercive field. In the TMR curve in Fig. 5.3(b) the maxima coincide reasonably well with the plateaus of the magnetization curve shown in Fig. 5.3(a). Compared with the junction without passivation, the TMR ratio with sulfide passivated barrier dropped from 0.20% to 0.11%, using the definition that $TMR = (R_{AP} - R_P)/R_P$, where R_P (R_{AP}) is the resistance for parallel (antiparallel) magnetization orientation in the contacts. The dc bias dependencies of the TMR effect at 4.2K for the above junction with and without passivation are shown in Fig. 5.4. The TMR effect decreases noticeably as the dc bias increases and the TMR values are consistently lower at all applied voltages for the passivated junction.

5.3.3 Discussion

Although the experiments of epitaxial growth of Fe layers on the S-passivated substrate show that the chemical inertness of the passivated surface could prevent the interdiffusion between ferromagnetic metal and semiconductor, resulting in the growth of a Fe film with higher magnetization. In passivated magnetic tunnel junctions, we find a decrease of TMR ratio. We suggest that there is a competing mechanism which is responsible for the decrease of TMR ratio in such a MTJ: the S overlayer increases the spin-

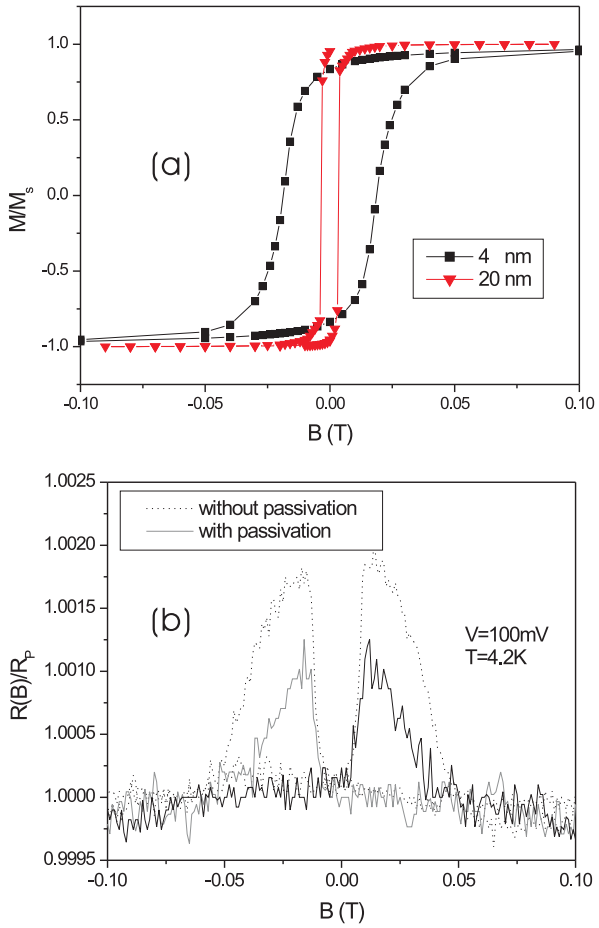

Figure 5.3: *(a) SQUID measurements of hysteresis loops of Fe films with different thicknesses. The coercivity of a 4nm film is larger than that of a 20nm Fe layer. (b) Magnetoresistance measurements for the junction with or without S-passivation at 4.2K under 100mV bias. The GaAs barrier is 6nm thick. After sulfide passivation, the TMR ratio decreases from 0.20% to 0.11%.*

flipping scattering at the Fe/GaAs interface. In the presence of spin-flip scattering of the passivation layer, the improvement of the magnetization of iron is more than compensated. Thus, the TMR ratio of tunnel junctions

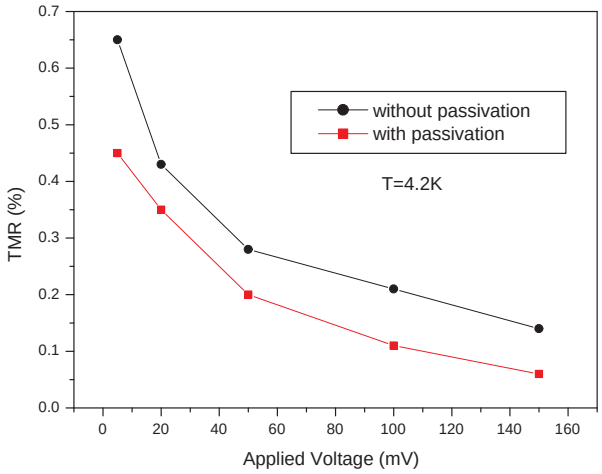

Figure 5.4: *Comparison of the voltage dependence of TMR traces with and without S-passivated GaAs barrier. The measurements were carried out at a temperature of 4.2K. The lines in the figure are a guide to the eye.*

with passivated GaAs barriers drops.

Hydrogen plasma etching

Another surface pretreatment experiment was performed by Juergen Moser in our group. The hydrogen plasma etching process was used before the growth of the ferromagnetic metal contact in the sputtering system. The details of the sputtering process with hydrogen plasma etching has been introduced in section 3.3.3. In principle, the plasma is used as an efficient means to produce active hydrogen atoms. Since the hydrogen atoms will chemically react with the material to form volatile hydride compounds, the material placed in the hydrogen plasma will be etched away [60, 61]. In this way, the native oxide layer, which is responsible for spin-flip processes, can be etched away leaving a clean surface for the deposition of the ferromagnetic metals.

Compared to the spin-polarized tunneling in a reference sample without surface pre-treatment, the experiments show that the TMR ratio of

the Fe/GaAs/Fe junctions increases from 1.3% ($P = 8.0\%$) to 5.6% ($P = 16.5\%$), when H_2 plasma etching is applied on both sides of the GaAs barrier. Since H_2 plasma etching can effectively increase the spin polarization in the ferromanets, this kind of surface pre-treatment was adopted in the fabrication of the spin injection devices.

Chapter 6

Theories of spin injection

As the ferromagnetic metals have a high Curie temperature and significant spin polarization even at room temperature, they are ideally suitable as spin injectors in semiconductor spintronic devices. However, efforts to inject spin polarized electrons from ferromagnets into semiconductors have so far resulted in low efficiencies indicating that the spin transport across the interface is not straightforward. In this chapter, the theoretical work on the spin injection will be discussed. The fundamental difficulties involved in the spin injection across the ferromagnetic metal-semiconductor interface, which can be overcome by introducing an interface resistance are analyzed. Spin injection through the space-charge region in magnetic p-n junctions is also discussed in this chapter.

6.1 Introduction to the spin injection model

The theories of spin injection across a ferromagnet/normal metal (F/N) interface, which also can be applied to a ferromagnet/semiconductor (F/SC) interface, have been studied by Johnson and Silsbee [81], van Son [82], Schmidt [9], Rashba [23], Valet and Fert [83], and others.

The theory to describe the spin injection is based on the assumption that spin-scattering occurs on a much slower timescale than other electron scattering events. With this assumption, two electrochemical potentials $\mu_\uparrow$ and $\mu_\downarrow$ which may not be equal can be defined for both spin orientations at any point in the device. If the current flow is one dimensional, e.g. in the

x direction, the electrochemical potentials are connected to the current via the conductivity σ, the diffusion constant D and the spin-flip time constant τ_{sf} by the following drift-diffusion equations:

$$\frac{\partial \mu_{\uparrow,\downarrow}}{\partial x} = -\frac{e j_{\uparrow,\downarrow}}{\sigma_{\uparrow,\downarrow}} \tag{6.1}$$

$$\frac{\mu_{\uparrow} - \mu_{\downarrow}}{\tau_{sf}} = \frac{D \partial^2 (\mu_{\uparrow} - \mu_{\downarrow})}{\partial x^2} \tag{6.2}$$

where D is a weighted average of the different diffusion constants for both spin orientations defined as $D = (\sigma_{\downarrow} D_{\uparrow} + \sigma_{\uparrow} D_{\downarrow})/\sigma$.

Starting from these equations, straightforward algebra results in a splitting of the electrochemical potentials at the boundary of the two materials, which is proportional to the total current density at the interface. The difference between the electrochemical potentials $(\mu_{\uparrow} - \mu_{\downarrow})$ decays exponentially inside the materials which approaches zero at $\pm\infty$

$$\mu_{\uparrow}(\pm\infty) - \mu_{\downarrow}(\pm\infty) = 0. \tag{6.3}$$

Spin-flip length ($L_{sf} = \sqrt{D\tau_{sf}}$) describes a typical length scale of the decay of the electrochemical potential difference in the material. For semiconductors, the spin-flip length L_{sf}^{SC} can exceed that of the ferromagnetic L_{sf}^{F} by several orders of magnitude, pointed out in reference [17]. In the limit of infinite L_{sf}^{SC}, this leads to a splitting of the electrochemical potentials at the interface which stays constant throughout the semiconductor. If the semiconductor extends to infinity, equation (6.1) in combination with equation (6.3) imply a linear and parallel slope of the electrochemical potentials for spin-up and spin-down in the semiconductor. This forbids the injection of a spin-polarized current if the conductivities of both spin channels in the semiconductor are equal. At the same time, over a length scale of the order of the spin-flip length in the semiconductor, the ferromagnetic contact influences the electron system of the semiconductor. Thus, if a second ferromagnetic contact applied at a distance smaller than the spin-flip length, it may lead to a considerably different behavior which is depending on its spin-polarization.

6.2 The F/N junction

Here we follow the approach from Smith et al. [84] to describe the spin injection across a ferromagnet/normal metal (F/N) interface. We consider the flow of electrons along the x direction in the junction, which consists of a metallic ferromagnet (region $x < 0$) and a paramagnetic metal or a degenerate semiconductor (region $x > 0$). The two regions, F and N, form a contact at $x = 0$, as depicted in Fig. 6.1. As we assume no strong spin-flip scattering at the interface, the individual current components for the two spin types are continuous at the interface. On the other hand, we also assume that an interface conductance is existing and the current flow at the interface can be described as

$$j^0_{\uparrow,\downarrow} = G_{\uparrow,\downarrow}(\Delta\mu_{\uparrow,\downarrow}/e) \tag{6.4}$$

where $j^0_{\uparrow,\downarrow}$ is the current density at the interface, $G_{\uparrow,\downarrow}$ is the interface conductance ($1/G_{\uparrow,\downarrow}$ is the interface resistance), and $\Delta\mu_{\uparrow,\downarrow}$ is an interfacial discontinuity in electrochemical potential for electrons of two spin types. Without loss of generality, if we assume a perfect interface without interface resistance which means the interface conductance is infinite, the electrochemical potentials $\mu_{\uparrow,\downarrow}$ and $j_{\uparrow,\downarrow}$ are continuous. On the contrary, for finite values of $G_{\uparrow,\downarrow}$, there is a discontinuity of $\mu_{\uparrow,\downarrow}$ at the interface. We define:

$$j_\uparrow = \eta j \qquad j_\downarrow = (1-\eta)j \tag{6.5}$$

$$\sigma_\uparrow = \alpha'\sigma \qquad \sigma_\downarrow = (1-\alpha')\sigma \tag{6.6}$$

were j is the total electron current density ($j = j_\uparrow + j_\downarrow$) and σ is the total conductivity. Because the steady state current is constant, η is continuous at the interface whereas α' is not continuous.

Solving equation (6.2) with the boundary conditions of equation (6.3) gives

$$(\mu_\uparrow - \mu_\downarrow) = A\exp(x/L^F_{sf}), \qquad \text{if } x < 0 \tag{6.7a}$$

$$(\mu_\uparrow - \mu_\downarrow) = B\exp(x/L^N_{sf}). \qquad \text{if } x > 0 \tag{6.7b}$$

Equation (6.4) for the interfacial discontinuity in the electrochemical potential gives a relation between the coefficients A and B,

$$B - A = ej\left[\eta\left(\frac{1}{G_\uparrow} + \frac{1}{G_\downarrow}\right) - \frac{1}{G_\downarrow}\right] \tag{6.8}$$

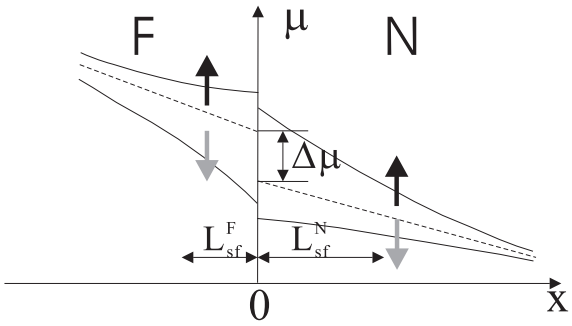

Figure 6.1: *Spatial variation of the electrochemical potential in a F/N junction with a spin-selective resistive interface. Due to current conversion, the average electrochemical potential (dashed line) will have a discontinuity at the interface [83].*

where η is evaluated at the interface. Equation (6.1), evaluated at the two sides of the interface gives

$$\frac{ej}{\sigma_F}\left[\frac{\eta-\alpha'_F}{\alpha'_F(1-\alpha'_F)}\right]=\frac{A}{L^F_{sf}}, \tag{6.9a}$$

$$\frac{ej}{\sigma_N}\left[\frac{\eta-\alpha'_N}{\alpha'_N(1-\alpha'_N)}\right]=\frac{B}{L^N_{sf}}. \tag{6.9b}$$

Equation (6.8) and (6.9) can be solved and result in the injected current spin polarization

$$\begin{aligned}\frac{j_\uparrow-j_\downarrow}{j} &= 2\eta-1\\ &= \frac{(2\alpha'_F-1)R_F+(2\alpha'_N-1)R_N+(1/G_\downarrow)-(1/G_\uparrow)}{R_F+R_N+(1/G_\downarrow)+(1/G_\uparrow)}\end{aligned} \tag{6.10}$$

with

$$R_{F,(N)}=\frac{L^{F,(N)}_{sf}}{\sigma_{F,(N)}\alpha'_{F,(N)}(1-\alpha'_{F,(N)})} \tag{6.11}$$

for the ferromagnet and normal metal, respectively. The preceding equations can be simplified if we define

$$\rho_{\uparrow,\downarrow}=2[1-(+)\beta]\rho^*_F, \qquad \text{for the F region} \tag{6.12a}$$

$$\rho_{\uparrow,\downarrow}=2\rho^*_N, \qquad \text{for the N region} \tag{6.12b}$$

where $\rho_{\uparrow,\downarrow}$ is the resistivity of the spin-up (down) channel in the ferromagnetic (F) and non-magnetic metal (N) regions [83]. For the F region, the resistivity ρ of bulk metal is expressed as

$$\rho = (1 - \beta^2)\rho_F^*. \tag{6.13}$$

The interface resistances of the two spin types are

$$r_{\uparrow,\downarrow} = 2r_b^*[1 - (+)\gamma], \tag{6.14}$$

where r_b^* is the interface resistance and γ is the spin selectivity. The important parameters in the spin injection are

$$r_F = \rho_F^* \times L_{sf}^F, \tag{6.15}$$

$$r_N = \rho_N^* \times L_{sf}^N. \tag{6.16}$$

Thus, equation (6.10) is given by the simple expression[1]

$$(SP)_I = \frac{j_\uparrow - j_\downarrow}{j} = \frac{\beta r_F + \gamma r_b^*}{r_F + r_N + r_b^*}. \tag{6.17}$$

By examining equation (6.17), we can both recognize some possible limitations and deduce several experimental strategies for effective spin injection from ferromagnets into semiconductors. For a perfect ohmic contact ($r_b^* = 0$), the resistance of the F region is far smaller than that of the N region ($r_F \ll r_N$), which implies inefficient spin injection with $(SP)_I \approx \beta r_F / r_N \ll 1$. This problem is called the conductivity mismatch pointed out by Schmidt et al. in 2000 [9]. As can be seen in equation (6.17), if a spin-selective resistive contact such as a tunnel or Schottky contact exists and $r_b^* \gg r_F, r_N$, it would contribute to an effective spin injection with $(SP)_I \approx \gamma$, dominated by the magnitude of γ and not by the ratio r_F/r_N.

6.3 The F/N/F junction

The above analysis of the F/N junction can be extended to a F/N/F junction in which two infinite F regions (labeled by $F1$ and $F2$) are separated by

[1]The substitutions are $(1/G_\uparrow + 1/G_\downarrow) \to 4r_b^*$; $(1/G_\downarrow - 1/G_\uparrow) \to 4\gamma r_b^*$; $(2\alpha'_F - 1) \to \beta$; $R_F \to 4r_F$; $R_N \to 4r_N$; $(2\alpha'_N - 1) \to 0$, respectively.

a N region of thickness t_N. If we only consider the situation $t_N \ll L_{sf}^N$, the resistance difference ΔR between the parallel and the antiparallel configuration of the magnetic moments of the two ferromagnets can be expressed as

$$\Delta R = \frac{2(\beta r_F + \gamma r_b^*)^2}{(r_b^* + r_F) + \frac{1}{2} r_N [1 + (r_b^*/r_N)^2] t_N / L_{sf}^N}. \tag{6.18}$$

The resistance $R^{(P)}$ for the parallel magnetic configuration is

$$\begin{aligned} R^{(p)} &= 2(1-\beta^2) r_F + r_N \frac{t_N}{L_{sf}^N} + 2(1-\gamma^2) r_b^* \\ &+ 2 \frac{(\beta-\gamma)^2 r_F r_b^* + r_N (\beta^2 r_F + \gamma^2 r_b^*) \tanh(t_N / 2L_{sf}^N)}{(r_F + r_b^*) + r_N \tanh(t_N / 2L_{sf}^N)}. \end{aligned} \tag{6.19}$$

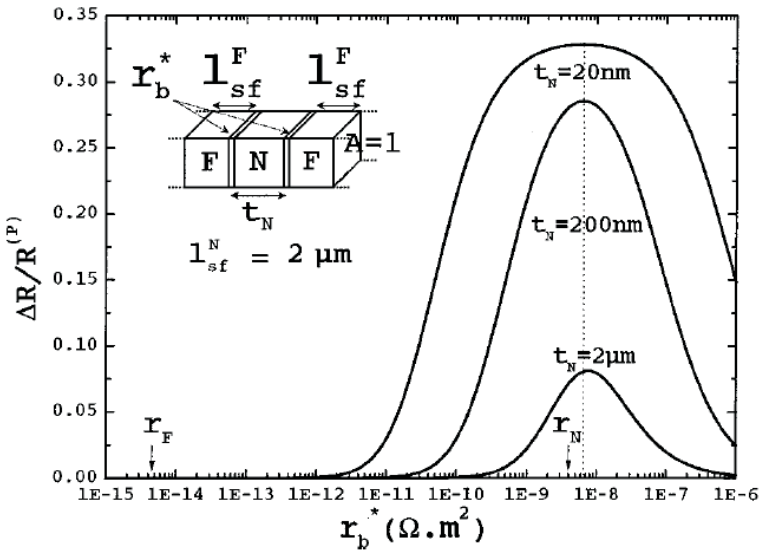

Figure 6.2: *Magnetoresistance versus interface resistance r_b^* of F/N/F structures. The geometry of the structure is shown in the inset [83].*

If we do not consider interface resistance and N is a semiconductor, we are in the limit $r_N \gg r_F$. From equations (6.18) and (6.19), the magnetoresistance can be written as

$$\frac{\Delta R}{R^{(P)}} = 8\beta^2 \left(\frac{r_F}{r_N} \frac{L_{sf}^N}{t_N} \right)^2, \tag{6.20}$$

which means a strong reduction of $\Delta R/R^{(P)}$ as was emphasized by Schmidt et al. [9]. If we consider the case of a F/SC/F structure with an interface resistance, the magnetoresistance as a function of r_b^* is shown in Fig. 6.2. From the figure, we find that achieving a large magnetoresistance requires correlated values of the interface resistance r_b^* and thickness t_N. To obtain a large magnetoresistance, r_b^* should be chosen only in a narrow range of

$$r_N \frac{t_N}{L_{sf}^N} < r_b^* < r_N \frac{L_{sf}^N}{t_N}. \tag{6.21}$$

The highest magnetoresistance within this range is expressed by the following equations:

$$\Delta R \simeq 2\gamma^2 r_b^*, \tag{6.22}$$

$$\frac{\Delta R}{R^{(P)}} \simeq \frac{\gamma^2}{1-\gamma^2}. \tag{6.23}$$

6.4 The magnetic p-n junction

6.4.1 Magnetic semiconductors

By examining equation (6.17), we find that even in the absence of the interface resistance, effective spin injection into a semiconductor can be achieved if the resistance mismatch is reduced, e.g. by using a magnetic semiconductor as a spin injector. Magnetic semiconductors are semiconductors doped with magnetic ions carrying a net spin. The interaction among these spins leads to a ferromagnetic state below the Curie temperature. This type of materials has a lattice structure similar to that of the undoped semiconductor, which allows the preparation of all semiconductor spin injection devices. As a result of that, the field of diluted magnetic III-V semiconductors, especially GaMnAs, has received considerable interest.

The ferromagnetic semiconductor $Ga_{1-x}Mn_xAs$ was introduced by Ohno et al. in 1996 [85, 86]. In order to introduce high concentrations of Mn beyond the solubility limit into GaAs, which is necessary to induce magnetic cooperative phenomena, low temperature ($< 300°C$) molecular beam epitaxy was employed. In GaMnAs, Mn ions produce magnetic moments as well as holes. Mn represents a shallow acceptor state and leads therefore to a high concentration of holes [87]. Although a detailed theory of ferromagnetism in GaMnAs has not been established yet, the Curie temperature may

be derived by use of a mean field theory of ferromagnetism in zinc blende magnetic semiconductor [88]. In a model based on this mean field theory, the Curie temperature of GaMnAs increases with the increase of both the Mn ions and the free hole concentration. It also has been found that the Curie temperature of as-grown GaMnAs epilayers can be further improved by low temperature annealing. The Curie temperature of GaMnAs in recent experiments is not yet sufficient high for applications at room temperature, but progress in this area is rapid and room temperature ferromagnetism seems to be reasonable.

The epitaxial growth of ferromagnetic semiconductors allows the integration of ferromagnetism with nonmagnetic semiconductors. For example, spin-polarized tunneling has been studied and a high TMR ratio of 290% has been found in a GaMnAs/GaAs/GaMnAs trilayers [89, 90]. GaMnAs was also used as the spin injector in spin LED experiments. Since GaMnAs is p-type, a hole spin injection was first demonstrated by Y. Ohno et al. in 1999 [28]. Eletron injection is also possible by the use of interband spin tunneling from a p-type ferromagnetic semiconductor [29]. Furthermore, magnetic p-n junction diodes have been proposed and theoretically analyzed, whose electronic properties depend on the spin polarization of the carriers [91–94]. The details of the spin injection through the space-charge region in such magnetic p-n junction diodes are introduced in the next section.

6.4.2 Spin injection through the depletion layer

In a magnetic p-n junction, the depletion layer is formed at the interface. The spin injection through the space-charge region in magnetic p-n junctions was discussed in details by Fabian and Žutić et al. [91–94]. The p-n junction is depicted in Fig. 6.3. The p region is magnetic and it has a spin-split conduction band with the Zeeman splitting $2q\zeta = qg\mu_B B$ (μ_B is the Bohr magneton). The n region is non-magnetic, but electrons in this region can be spin polarized by an external spin source, such as circularly polarized light or a magnetic electrode. The I-V characteristic of the junctions is determined by the interplay between the equilibrium spin polarization $p_{n0} = \tanh(q\zeta/k_BT)$ in the p region and the non-equilibrium spin polarization δP_n in the n region.

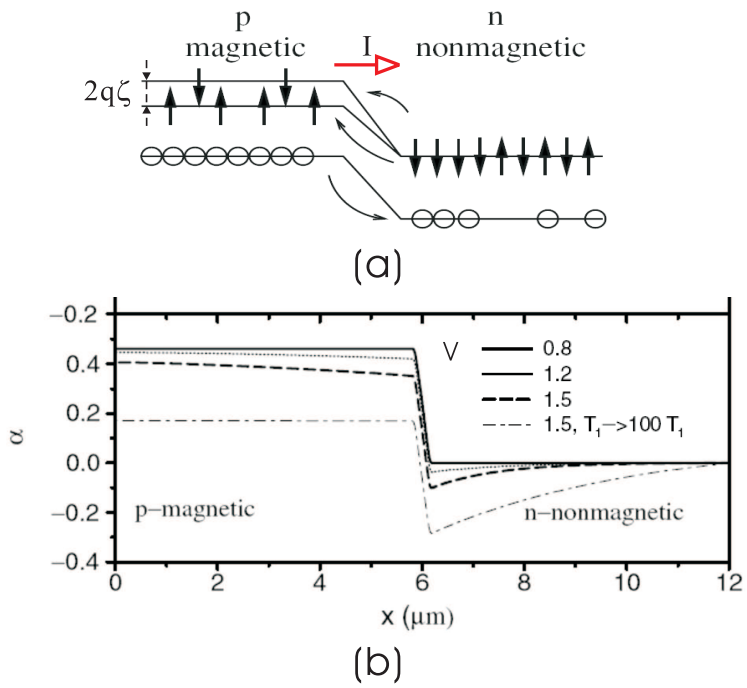

Figure 6.3: *Spin injection through the space-charge region of a magnetic p-n junction. (a) Nonequilibrium spins in the n region can be injected into the magnetic p region (note the split band) only at high bias. Solid circles are spin-polarized electrons and open circles are unpolarized holes. (b) Calculated spin polarization profiles for different forward bias. The largest injection in the graph is for a bias V of 1.5V, assuming spin relaxation time of* $100\tau_{sf}$ *[93].*

The dependence of the electric current j on $q\zeta$ and δP_n is shown in Fig. 6.3(b), which is obtained by a numerical calculation [93] solving the drift-diffusion, continuity, carrier recombination and spin-relaxation equation. It is found that at small bias, there is no spin injection. This is the normal limit of diode operation, in which the injected carrier density through the depletion region is still small compared to the equilibrium carrier density. Only with increasing bias (typically above 1V), spins are efficiently injected.

Magnetic p-n junctions can display a GMR-like effect. The current

$$j_n \sim n_0(\zeta)[\exp(qv/k_BT)(1 + \delta P_n P_{n0}) - 1] \tag{6.24}$$

depends strongly on the relative orientation of the nonequilibrium spins and the equilibrium magnetization [6]. When $\delta P_n \neq 0$, the current will depend on the sign of $\delta P_n P_{n0}$. Thus, for parallel and antiparallel relative orientations, the electrons across the depletion layer may experience a different barrier resulting in a change of current. The basic concepts of this effect are applied to design our spin injection experiments for detecting nonequilibrium spins in the non-magnetic semiconductors.

Chapter 7

Interface resistivity of the Fe/GaAs Schottky barrier

As we discussed in the last chapter, the conductivity mismatch is the intrinsic obstacle for effective spin injection into semiconductors [9]. In order to overcome the conductance mismatch problem, Schottky barriers or tunneling barriers inserted between the ferromagnetic metal and semiconductor producing an interface resistance have been proposed by Rashba and Schmidt et al. [23, 24].

In this chapter, the measurement results of the interface resistivity in Fe/GaAs Schottky barriers will be presented. First, the current transport mechanisms through the Schottky barrier are introduced, followed by the calculation of the depletion layer width and the Fermi level of the barrier for different GaAs doping densities. Next, the sample preparation of the Fe/GaAs Schottky barrier is explained. Finally, we give a discussion of the *I-V* characteristics as well as of the interface resistivity using heavily doped barriers density. This chapter serves as the base for the device design for spin injection experiments.

7.1 Current transport mechanisms in the Schottky barrier

Schottky barriers have been studied for many years and several theories are proposed to describe the mechanisms of current flow. In 1938, both

Schottky and Mott independently suggested a model to explain this phenomena [38, 39]. After that, Crowell and Sze employed Schottky's diffusion model and Bethe's thermionic emission theory to describe the Schottky barrier [38]. Padovani and Stratton analyzed tunneling currents in Schottky barriers using field and thermionic-field emission with a one-dimensional WKB approximation [95]. Recently, Sassen et al. tried to analyze a Schottky diode using the transfer matrix method in GaAs, which required numerical analysis [96].

7.1.1 Thermionic emission model

The thermionic model of electron transport in Schottky barriers is valid when the interface barrier presents a substantial important impediment to the current flow [38, 39]. It assumes that electrons have sufficient energy to go over the barrier, see Fig. 7.1. The current can be expressed as

$$J = J_{st}\left[\exp\frac{qV}{nk_BT} - 1\right], \tag{7.1}$$

where J_{st} is the saturation current density, given by

$$J_{st} = A^*T^2\exp\frac{-q\varphi}{k_BT}. \tag{7.2}$$

Here, φ is the Schottky barrier height and A^* is the Richardson constant. In equation (7.1), n is the ideality factor, which gives a measure of the quality of the junction. For an ideal Schottky barrier, $n = 1$, however, larger values are obtained due to the presence of non-ideal effects or components to the current through the junction.

7.1.2 Thermionic-field emission and field emission

For a moderately to heavily doped semiconductor or for operation at low temperatures, the current due to quantum mechanical tunneling of carriers through the barrier will become the dominant transport process [95].

Thermionic-field emission

In Schottky barriers on highly doped semiconductors the depletion region becomes so narrow that electrons can tunnel through the barrier near the

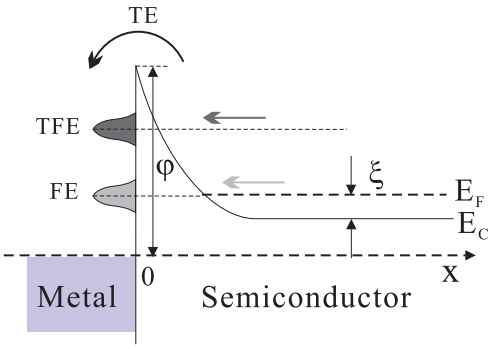

Figure 7.1: *Schematic band energy diagram of a metal/n-semiconductor contact with forward bias showing the three major current transport mechanisms: thermionic emission (TE), thermionic-field emission (TFE) and field-emission (FE).*

top, see Fig. 7.1. This process is called thermionic-field emission. The current-voltage characteristics of a Schottky diode in the case of thermionic-field emission can be calculated by evaluating the product of the tunneling transmission coefficient and the number of electrons as a function of energy. Integration over the states in the conduction band yields

$$J = J_{stf} \exp \frac{qV}{E_0}, \tag{7.3}$$

where J_{stf} is tunneling saturation current density for thermionic-field emission and E_0 is a tunneling constant which can be described as

$$E_0 = E_{00} \coth \frac{E_{00}}{k_B T}. \tag{7.4}$$

The tunneling saturation current density is a complicated function of temperature, barrier height and semiconductor parameters. In the notation of Padovani and Stratton [95], E_{00} is a tunneling parameter inherently related to material properties of the semiconductor and is given by

$$\begin{aligned} E_{00} &= \frac{qh}{4\pi} \left(\frac{N_d}{m^* \epsilon_s} \right)^{1/2} \\ &= 1.85 \times 10^{11} \left[\frac{N_d(cm^{-3})}{(m_n/m_e)(\epsilon_s/\epsilon_0)} \right]^{1/2} (eV), \end{aligned} \tag{7.5}$$

where h is Planck's constant and N_d is impurity doping concentration.

Field emission

In degenerate semiconductors, especially in semiconductors with a small electron effective mass, such as GaAs, electrons can tunnel through the barrier near the Fermi level. Such a mechanism is called as field emission. This happens when E_{00} becomes much greater than k_BT. The current-voltage characteristics in this regime are given by

$$J = J_{sf} \exp \frac{qV}{E_{00}}, \tag{7.6}$$

where J_{sf} is tunneling saturation current density for field emission. The effective resistance of the Schottky barrier in the field-emission regime is quite low.

Reverse I-V characteristic

When a reverse bias is applied over the barrier, the probability for an electron to tunnel from the metal into the semiconductor is increased. If field emission and thermal-field emission are the dominant forward conduction mechanisms, they will also be the dominant mechanisms for the reverse characteristics. The I-V relationship can thus be expressed as:

$$J = J_s \exp(-qV/\varepsilon'), \tag{7.7}$$

where J_s is the saturation current with a reverse bias and

$$\varepsilon' = E_{00}[E_{00}/k_BT - \tanh(E_{00}/k_Bt)]^{-1}. \tag{7.8}$$

From the equations above, the current under a reverse bias has an exponential dependence on the applied voltages.

7.2 Depletion layer and Fermi level of Fe/GaAs Schottky barrier

7.2.1 Depletion layer width

As introduced in section 2.2, the conduction band electrons which cross over into the metal leave a positive charge of ionized donors behind, so the semiconductor region near the metal gets depleted of mobile electrons.

According to the Poisson equation, the width of the depletion layer can be written as $W = [2\epsilon_s/qN_d \times (\varphi - V)]^{1/2}$, where φ is the barrier height, ϵ_s is the dielectric permittivity of the semiconductor and N_d is impurity doping concentration. For a Fe/GaAs Schottky barrier without applied voltage V and $\epsilon_s = \epsilon_r\epsilon_0$, where ϵ_0 is the permittivity of vacuum and for GaAs $\epsilon_r = 13.18$, the depletion layer width can be calculated by

$$W = 3.816 \times 10^{10} \sqrt{\frac{\varphi(V)}{N_d(cm^{-3})}}(nm), \tag{7.9}$$

which only depends on the barrier height and donor concentration [38].

7.2.2 Position of the Fermi level

If the donor concentration N_d is increased in a semiconductor, the Fermi energy E_F in the energy gap is shifted towards the conduction band. When the impurity concentration becomes high enough, the top of the impurity band merges into the conduction band. The detailed calculation of the Fermi level position for the doped n-GaAs is discussed in this section.

For a degenerately doped semiconductor, the electron density n_0 in the conduction band is given by

$$n_0 = N_c \times F_{1/2}\left(\frac{E_F - E_C}{k_B T}\right), \tag{7.10}$$

where N_c is the effective density of states for the conduction band and $F_{1/2}(\eta)$ is the Fermi integral expressed as

$$N_c = 2\left(\frac{m_n k_B T}{2\pi\hbar^2}\right)^{3/2}, \tag{7.11}$$

$$F_{1/2}(\eta) = \frac{2}{\sqrt{\pi}} \int_0^\infty \frac{x^{1/2}}{1 + \exp(x - \eta)} dx. \tag{7.12}$$

When a semiconductor contains dopants at a concentration N_d, we find the ionized donor density N_d^+ as

$$N_d^+ = \frac{N_d}{1 + g_d \exp[(E_F - E_d)/k_B T)]}, \tag{7.13}$$

where g_d is the donor degeneracy factor and E_d is the donor level energy. In the simplest case $g_d = 2$ because of two possible values for the electron

$N_d(\mathrm{cm}^{-3})$	1×10^{16}	1×10^{17}	3×10^{18}
$E_F - E_C(\mathrm{eV})$	-0.099	-0.046	0.009
Depletion layer width(nm)	296	93	17

Table 7.1: *List of Fermi level and depletion layer width of Fe/GaAs Schottky barrier with different doping densities. Si is used as the dopant for n-type GaAs.*

spin. The charge neutrality condition gives the relationship between the free electron density and the ionized impurity density:

$$n_0 = N_d^+. \tag{7.14}$$

Substitution with equation (7.10) and equation (7.13) leads to

$$N_d = N_c \left[1 + 2\exp\left(\frac{E_F - E_C}{k_B T}\right)\exp\left(\frac{E_C - E_d}{k_B T}\right)\right] F_{1/2}\left(\frac{E_F - E_C}{k_B T}\right), \tag{7.15}$$

which can be solved numerically for non-degenerated and degenerated semiconductors [38].

7.2.3 Numerical evaluation

The calculated band diagrams for Fe/GaAs Schottky barriers with doping densities $N_d = 1 \times 10^{16}\mathrm{cm}^{-3}$ (top graph), $N_d = 1 \times 10^{17}\mathrm{cm}^{-3}$ (middle graph) and $N_d = 3 \times 10^{18}\mathrm{cm}^{-3}$ (bottom graph) are depicted in the Fig. 7.2. The detailed depletion layer width and the position of Fermi level of Fe/GaAs Schottky barrier with different doping concentrations are listed in the Tab. 7.1. For the heavily doped GaAs ($N_d = 3\times10^{18}\mathrm{cm}^{-3}$), the Fermi level is shifted above the conduction band edge and the depletion layer width is as narrow as 17nm. For this highly doped degenerate semiconductor, electrons near the Fermi level can tunnel through the barrier easily, hence the field-emission becomes the dominant transport mechanism.

7.3 Sample preparation

In the experiments, we use GaAs epitaxial layers with different doping density on semi-insulating substrates. The homogeneous doping density and

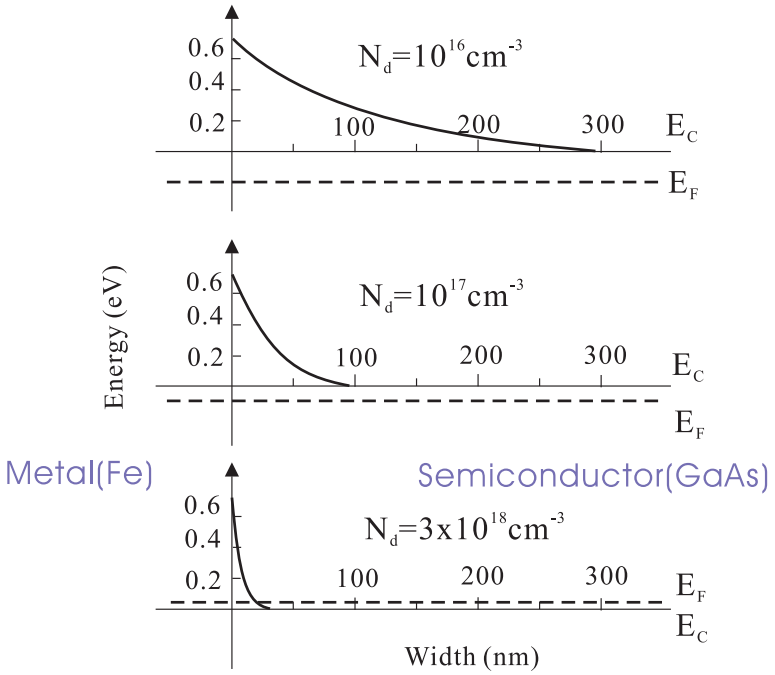

Figure 7.2: *Band diagram of Schottky barriers for Fe/GaAs junctions of different doping densities. As the doping density increases, the depletion layer width becomes thinner and the Fermi level merges with the conduction band.*

the related bulk resistivity of the GaAs at low temperature of 4.2K are measured with van der Pauw technique, which is a combination of a resistivity measurement and a Hall measurement.

The ferromagnetic layer of Fe is deposited on the GaAs to form the Fe/GaAs Schottky barrier. In order to reduce the effect of series resistances (R_s), Ni/AuGe is deposited on the wafer using the same geometry as for the Fe/GaAs barrier. A schematic diagram of doped n-GaAs with a Fe/GaAs Schottky barrier prepared for interface resistivity measurements is shown in Fig. 7.3.

The ohmic contact on the n-type GaAs layer is fabricated by using a Ni/AuGe system [97]. Because the annealing procedure at high temperatures for the ohmic contact preparation may destroy the Fe/GaAs Schottky barrier, the Ni/AuGe contact is prepared first. The wafer is cleaned with

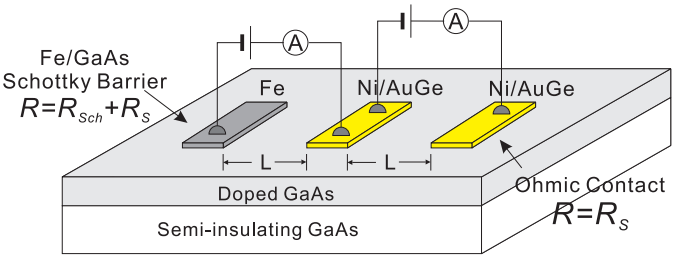

Figure 7.3: *Schematic diagram of the interface resistivity measurements of Fe/GaAs Schottky barrier. R_{Sch} and R_s stand for the resistance of Schottky barrier and series resistance.*

acetone and propanol in the standard cascade rinse procedure. After lithography, the oxidation layer on the GaAs layer is etched away in the diluted HCl acid. A 150nm AuGe alloy is deposited and followed by 40nm Ni. Using a lift-off process, the metal on the photoresist is removed and the wafer is annealed at the temperature of 350°C for 120sec and at 400°C for 20sec to form the ohmic contact. In the next step, employing lithography and another lift-off process, a 20nm ferromagnetic layer of Fe is deposited on the GaAs surface to form the Fe/GaAs Schottky barrier. A 150nm gold film is deposited as an electrical contact layer, which is also used to prevent the Fe layer from oxidation. The contact area in the experiments is $3.675 \times 10^{-4}\text{cm}^2$.

7.4 Measurement results and discussion

Fig. 7.4 shows the logarithmic I-V plot of the manufactured Fe/GaAs contact at room temperature. As shown schematically in Fig. 7.3, the total resistance (R) across the Schottky barrier is $R_{Sch} + R_s$, where R_{Sch} is the resistance of the Schottky barrier only and R_s is the series resistance. The series resistance R_s is measured between the two ohmic contacts, which can be subtracted in order to obtain the experimental data of Fig. 7.4. As the figure shows, the measured I-V curves vary with the doping density of GaAs. At a highly doped metal-semiconductor barrier, the field emission becomes the dominant transport mechanism.

The temperature dependence of the I-V characteristics is studied for moderately and heavily doped Fe/n-type GaAs Schottky barriers. A set

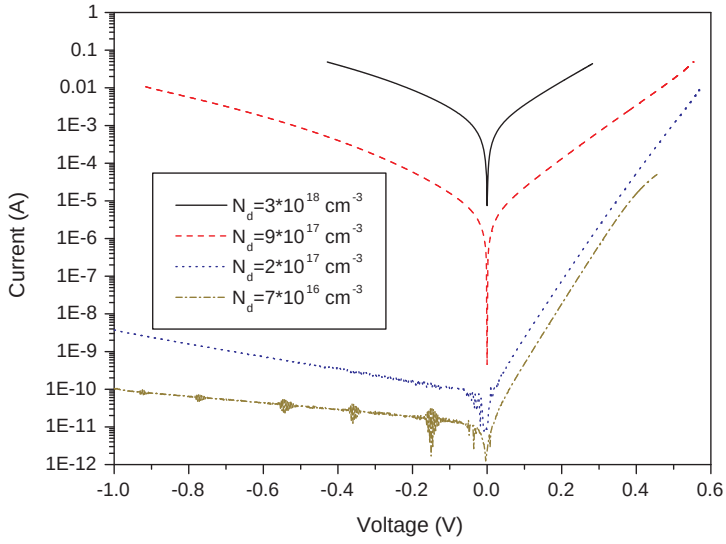

Figure 7.4: *I-V characteristics of the Fe/GaAs Schottky barriers with different doping densities.*

of experimental I-V characteristics of the Fe/GaAs Schottky barrier with the doping density of $2 \times 10^{17}\text{cm}^{-3}$ is shown in the Fig. 7.5(a). The linear dependence of the logarithm of the current on the applied bias is observed at all temperatures. Using equation (7.3), E_0 for each temperature can be determined by measuring the slope of the characteristic. Fig. 7.5(b) is a plot of E_0 as a function of the temperature together with the predicted curve given by the equations (7.4) and (7.5). In the calculation, $m^* = 0.068$ as the effective mass of GaAs [98] and a carrier concentration of $2 \times 10^{17}\text{cm}^{-3}$, assuming that all the dopants are ionized, were used. From the experimental data and the fitting curve, we can find that in this region of doping density thermionic-field emission is the dominant transport mechanism.

Fig. 7.6 shows the temperature dependence of the I-V characteristic of the heavily doped Fe/GaAs Schottky barrier with a doping density of $3 \times 10^{18}\text{cm}^{-3}$. As expressed by equation (7.6), for field-emission as the dominant transport mechanism, E_{00} follows from the slope of the logarithmic plot of the I-V characteristic. Since E_{00} is only determined by the doping density,

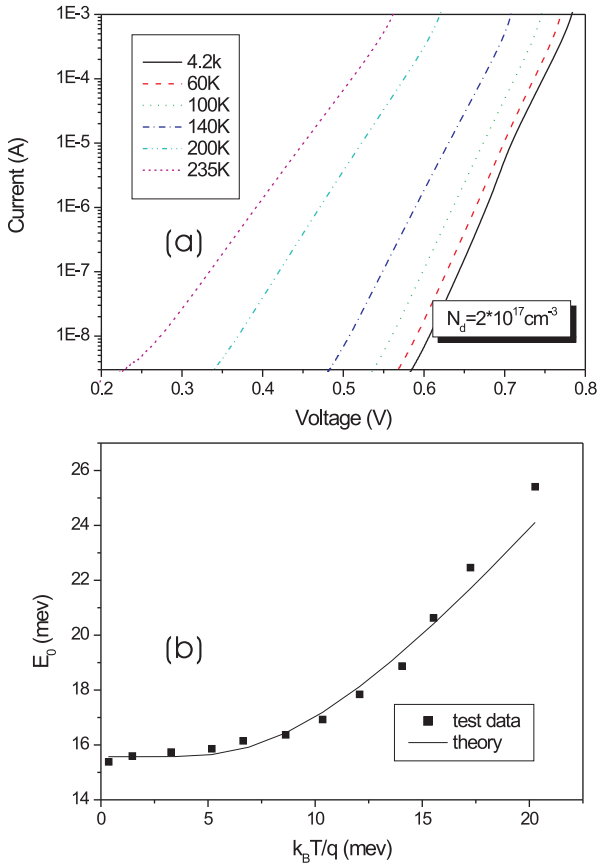

Figure 7.5: *(a) Temperature dependence of the forward I-V characteristics of the Fe/GaAs Schottky barrier with a doping density of* $2 \times 10^{17}\,cm^{-3}$*. (b) Experimental values of* E_0 *as a function of temperature extracted from the data in the above figure. The solid line represents the theoretical temperature dependence.*

the slope will not vary with the temperature. We indeed find the same slope in the forward I-V curves in this figure and conclude that the current transport through this Schottky barrier is mostly due to field-emission.

The measurement of the resistivity of bulk GaAs with different doping densities at 4.2K is shown as squares in Fig. 7.7. The resistivity (ρ_N^*) of

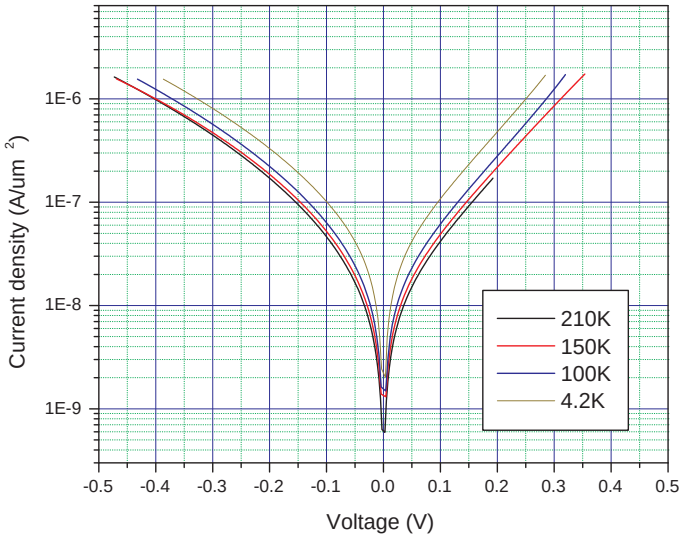

Figure 7.6: *Temperature dependence of I-V characteristics of a heavily doped Fe/GaAs Schottky barrier with a doping density of* $3 \times 10^{18} cm^{-3}$*. The same slope of all forward I-V curves indicates that the current transport is due to field-emission.*

the bulk GaAs is determined by the van der Pauw technique. The dashed line represents the linear fitting results of the resistivity at low temperature. In the experiments, we find the resistivity $\rho_N^* = 0.4\Omega\cdot$cm in GaAs with a doping density of 10^{16}cm^{-3}. The correlated r_N, which is the product of the resistivity and the spin diffusion length defined as $r_N = \rho_N^* \cdot L_{sf}^N$ see equation (6.16), is also shown in the figure (right axis). Here we use $L_{sf}^N = 2\mu$m for the GaAs sample [99].

The interface resistance as a function of applied bias of the Fe/GaAs barrier with a high doping density of $3 \times 10^{18}\text{cm}^{-3}$ was extracted from the *I-V* curves introduced above and was shown as the solid line in the same figure (top and right axis).

As we discussed in section 6.3, for the spin injection in a F/N/F junction, in order to obtain a large magnetoresistance ratio, r_b^* should be chosen only

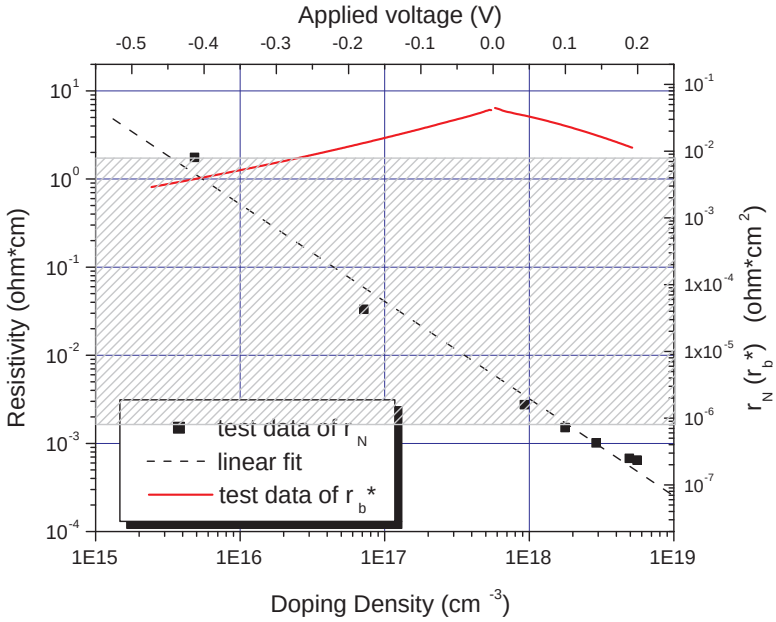

Figure 7.7: *Schematic Fert's conditions for spin injection in a F/N/F junction with Fe/GaAs Schottky barriers. Squares are the test data of the resistivity (ρ_N^*) of the bulk GaAs of different doping densities. Dashed line represents the linear fitting. The correlated r_N of the bulk GaAs is shown according to the right y-axis. Solid line shows the interface resistivity of the Fe/GaAs Schottky barrier with a doping density of $3 \times 10^{18} cm^{-3}$. The shadow region shows the range of Fer's conditions to obtain large magnetoresistance, where $t_N = 20nm$ and $L_{sf}^N = 2\mu m$.*

in a narrow range of

$$r_N \frac{t_N}{L_{sf}^N} < r_b^* < r_N \frac{L_{sf}^N}{t_N}.$$

The shadow region in the figure shows the range of this condition, assuming a transport length $t_N = 20$nm. Furthermore, since electrons have longest spin life times in GaAs at a doping density near 10^{16}cm^{-3} [18], we use $r_N = 8 \times 10^{-4}\Omega\cdot\text{cm}^2$. The solid line which represents the test data of interface resistance reaches the shadow area when a proper bias is applied

on the Fe/GaAs Schottky barrier.

From the calculation and experiments presented, we find that increasing the bulk doping density decreases the depletion region width and changes the interface resistance. Fig. 7.7 shows that if we control the transport length on the scale of nanometers, the interface resistance of the Fe/GaAs barrier with a high doping density can meet Fert's condition for efficient spin injection into semiconductors. Although the detailed theoretical mechanism of spin injection through the Schottky barrier has not been clarified yet, the interface resistance measurements in our experiments can serve as a guide for designing spin injection experiments.

Chapter 8

Spin injection experiments

In this chapter, we demonstrate the fabrication of a novel magnetic p-n junction diode, in which the spin injection between ferromagnetic metals and semiconductors is measured all-electrically. First, we discuss the sample design and introduce the sample structure and fabrication procedure. Next, the I-V characteristic and the spin injection phenomena of the magnetic p-n junction diode are discussed. The experimental results of spin injection in a Fe/GaAs/Fe structure are also introduced in this chapter.

8.1 Spin injection in a magnetic p-n junction diode

8.1.1 Device design

The design of the magnetic p-n junction diode is based on the analysis and proposal from Žutić and Fabian et al. [91, 93] introduced in section 6.4. In the magnetic p-n junction structure, the depletion layer is formed at the interface. The spin polarized carriers can be injected through the space-charge region when the bias over the magnetic p-n junction is increased above the high injection limit. A schematic drawing of the band diagram for such a magnetic/nonmagnetic semiconductor p-n junction in contact with a ferromagnetic metal is presented in Fig. 8.1.

The device performs as follows: a positive bias is applied between the p-GaMnAs and the ferromagnetic Fe layers. This places the magnetic p-n junction in forward direction and the Fe/GaAs Schottky barrier in reverse direction. Consequently the spin-polarized electrons are injected from Fe into

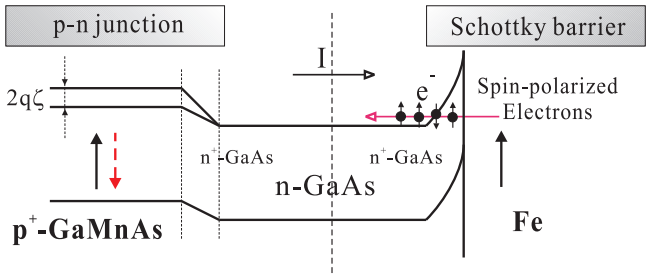

Figure 8.1: *Band diagram of a magnetic p-n junction diode with a Fe/GaAs Schottky barrier. The p region (left) is a magnetic GaMnAs layer, indicated by the spin splitting of the conduction band. Under applied forward bias, the spin-polarized electrons are injected from Fe (right) to n-GaAs region (middle) and then drift to the p region. Up and down arrows indicate the magnetizations of the two electrodes.*

the bulk n-GaAs via the Schottky contact, thereby overcoming the conductance mismatch between ferromagnetic metals and semiconductors [9,23,83]. The spin-polarized electrons in n-GaAs drift then across the depletion layer into p-GaMnAs under the applied voltage. If the relative magnetizations of the two magnetic electrodes are changed from parallel to antiparallel, the magnetic p-n junction diode should display a GMR-like effect.

8.1.2 Layer sequence of the semiconductor wafer

The preparation of the hybrid structure is started from the semiconductor heterostructure, which was grown on a semi-insulating(s.i.) GaAs substrate by molecular beam epitaxy at a growth temperature of 630 °C. It has the following layer sequence: GaAs(001) substrate(s.i.)/ 300nm GaAs buffer layer/ 300nm AlAs-GaAs superlattice/ 100nm GaAs/ 50nm $Al_{0.72}Ga_{0.18}As$/ 15nm n^+-GaAs(3×10^{18}cm^{-3})/ 50nm n-GaAs(1×10^{16}cm^{-3})/ 10nm n^+-GaAs(3×10^{18}cm^{-3})/ 60nm p-$Ga_{0.94}Mn_{0.06}As$, as shown in Fig. 8.2.

In the sample structure, the 50nm n-GaAs is used as transport region for spin-polarized electrons. The 10nm n^+-GaAs layer with a Si doping density of 3×10^{18}cm^{-3} leads to a small depletion region between p-GaMnAs and the bulk n-GaAs layer. The other 15nm n^+-GaAs is used to control the Schottky barrier interface resistivity between Fe and GaAs, as discussed in the last chapter. The 60nm layer of p-GaMnAs was grown at low temperature, as

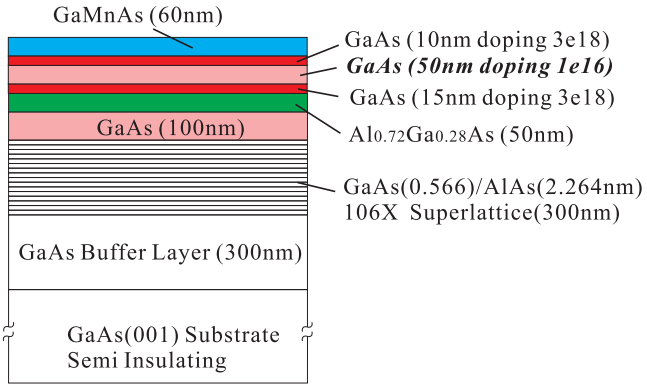

Figure 8.2: *Epitaxial structure of the wafer for the magnetic p-n junction diode. The 300nm thick AlAs/GaAs superlattice acts as an etch stop layer.*

required for high-quality GaMnAs growth.

8.1.3 Sample fabrication

In order to realize the device, we use the epoxy bonding and stop-etching technique (EBASE) [30, 31], which relies on the highly selective etching of GaAs and $Al_xGa_{1-x}As$ by suitable wet chemical etchants. The fabrication steps of the sample involve conventional optical lithography and lift-off procedures as introduced in chapter 3 and the detailed steps can be found in the appendix. Here we only emphasize some special procedures.

In the magnetic *p-n* junction diode, a 100nm Au film deposited on the GaMnAs layer is used as the metallic contact for the soft magnetic electrode. Before deposition of the second contact, the GaAs semiconductor surface is treated with H_2 plasma to remove the oxidation layer. After mesa etching, a thick SiO_2 film was deposited for electrical isolation. The sample structure of the whole device with four-point measurement is shown in Fig. 8.3 schematically.

8.1.4 Magnetic properties of GaMnAs

The hysteresis loop and Curie temperature of the *p*-$Ga_{0.94}Mn_{0.06}As$ layer used in our work were measured by means of superconducting quantum interference device (SQUID). The GaMnAs layer was grown at a low tem-

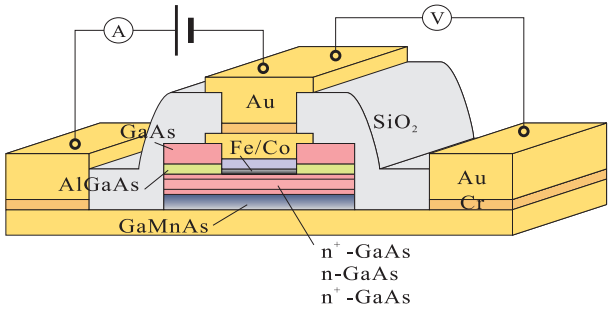

Figure 8.3: *Magnetic p-n junction diode geometry for four-point measurements. The transport region of GaAs is sandwiched between GaMnAs and Fe/Co layers, which are used as soft and hard magnetic electrodes, respectively.*

perature around 250°C and the thickness of the layer is 60nm. Fig. 8.4(a) shows the magnetization curve versus magnetic field at 10K. The Magnetic field is applied in the plane and along the [110] direction. The sharp, square hysteresis loop, indicates a well-ordered ferromagnetic structure and a coercivity of around 3mT. The temperature dependence of the magnetization is depicted in Fig. 8.4(b). Since the GaMnAs layer has not been annealed, it has a relatively low Curie temperature of around 65K.

8.1.5 Spin injection results and discussion

The electric and magneto-transport properties of the ferromagnet based magnetic *p-n* junction were studied at a temperature of 4.2K. The sample was mounted in an insert of a ^{4}He cryostat with a superconducting coil and the magnetic field was aligned in the plane of the hybrid structure.

The *I-V* curves of the magnetic *p-n* junction diode measured at room temperature and 4.2K are shown in the inset of Fig. 8.5. If we look closer at the logarithmic plot of the current vs. applied voltage, different slopes of the curve can be found. The device studied here can be treated as a stack of a *p-n* junction and a Schottky diode. For the *p-n* junction, the current can be expressed as:

$$J = J_{s1}[\exp(qV_1/k_0T) - 1], \tag{8.1}$$

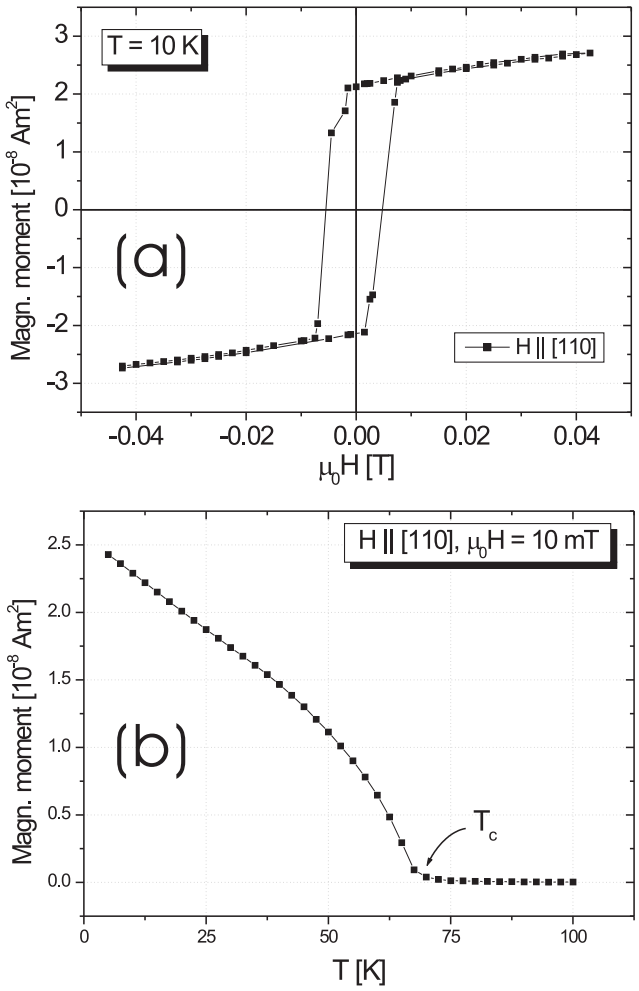

Figure 8.4: *(a) Hysteresis loop of GaMnAs determined by SQUID. The easy axis is in the plane and the coercivity of the GaMnAs layer is 3mT. (b) Temperature dependent magnetization of the GaMnAs layer (Curie temperature ≈65K).*

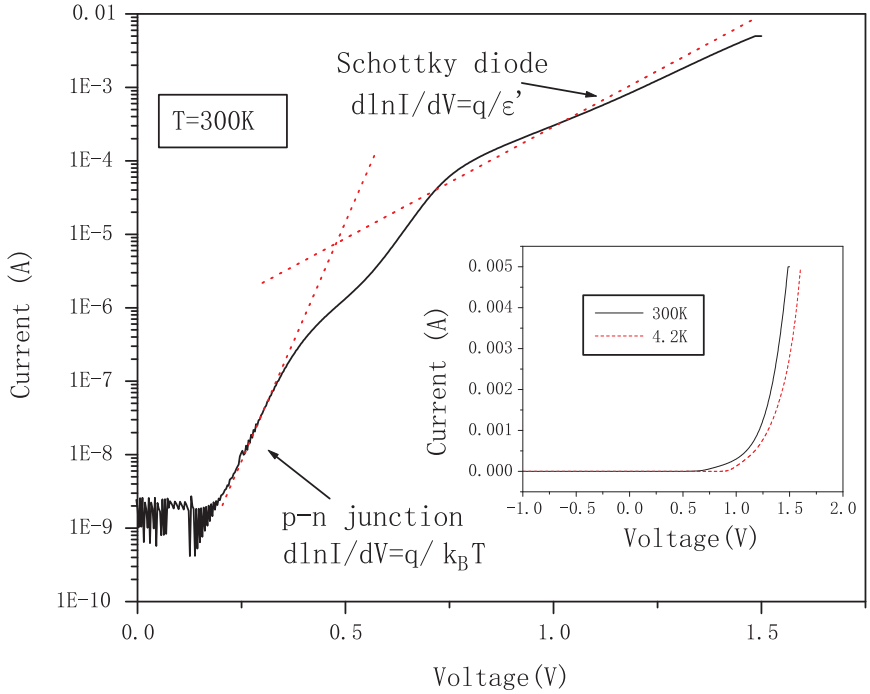

Figure 8.5: *Logarithmic plot of the forward I-V characteristic of the magnetic p-n junction diode at room temperature. The dotted lines represent the theoretical slopes of the curve, for an I-V characteristic dominated by the p-n junction or Schottky diode, respectively. The inset shows the I-V curves of the device at 4.2K (dashed line) and room temperature (solid line).*

and for the Schottky diode:

$$J = J_{s2} \exp(qV_2/\varepsilon'), \tag{8.2}$$

where J_{s1}, V_1 and J_{s2}, V_2 are the saturation current densities and biases for the p-n junction and the Schottky diode, respectively. Here we consider thermionical-field emission as the major contribution to the I-V characteristic of the Schottky diode under reverse bias, because heavily doped n^+-GaAs with a doping density of $N_d = 3 \times 10^{18}\text{cm}^{-3}$ was used in the device [95]. From the definitions: $\varepsilon' = E_{00}[E_{00}/k_BT - \tanh(E_{00}/k_Bt)]^{-1}$, $E_{00} = (qh/4\pi)[N_d/m^*\epsilon_r\epsilon_0]$, we obtain $\varepsilon' = 78.5\text{meV}$, which is three times as large as k_BT at room temperature.

At low voltage, the resistance of the Schottky barrier is much lower than that of the *p*-*n* junction. Consequently, the *I*-*V* characteristic is dominated by the *p*-*n* junction with a slope equal to q/k_BT as shown in Fig. 8.5. When the voltage is increased, the resistance of the Schottky barrier becomes comparable to the *p*-*n* junction and cannot be neglected, and at high voltage, the slope equals to q/ε' when the Schottky diode dominates the *I*-*V* curve.

Fig. 8.6(a) shows the magnetic hysteresis loops at 10K for the GaMnAs(60nm) and Fe(12nm)/Co(50nm) layers. Using a Co layer to magnetically bias the Fe film, the coercivity of the 12nm Fe layer is 30mT, while the GaMnAs layer has the coercivity of 3mT. In the magnetic field range between these coercivities, the ferromangets' magnetization can be switched to anti-parallel orientation. Shown in Fig. 8.6(b) is the magnetoresistance curve of the device versus applied magnetic field at 4.2K. The negative magnetoresistance curve coincides reasonably well with the distinct coercive fields of the magnetization curve. With forward applied bias of 1450mV, a negative magnetoresistance of 1.02% is found.

Temperature dependence of magnetoresistance is shown in Fig 8.7. The measurements were taken at various temperatures with an applied bias of 1400mV. As the Curie temperature of the GaMnAs layer in the *p*-*n* junction diode is as low as 65K, the magnetoresistance drops with increasing temperature. For temperatures above 35K, the noise is so large that the resistance change between the parallel and antiparallel configurations cannot be separated.

The bias voltage dependence of the magnetoresistance was also studied and the results are shown in Fig. 8.8. Magnetoresistance can only be found with high forward bias on the device. This is an agreement with the theoretical analysis on the magnetic *p*-*n* junction which shows that there should be no spin injection at small biases, because the injected polarized carrier density is then much smaller than the equilibrium carrier density. It was found that typically for a bias above 1V, the spin-polarized carriers can be injected across the depletion layer [91]. Furthermore, we also find there is a peak of the negative magnetoresistance of 1.2% at 1400mV bias. This effect is due to the interface resistance which was analyzed by Fert [83], see section 6.3. In his theoretical calculation, the highest magnetoresistance is obtained in the limit $r_N(t_N/l^N_{sf}) \ll r^*_b \ll r_N(l^N_{sf}/t_N)$, where r_N is the product of the semiconductor resistivity and the spin diffusion length(l^N_{sf}), t_N is

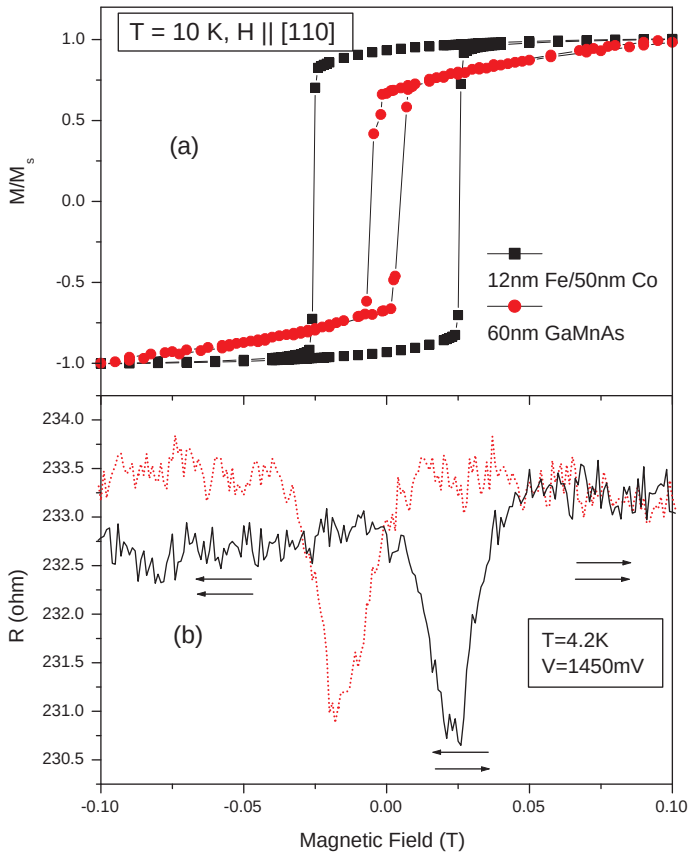

Figure 8.6: *(a) SQUID measurements of the GaMnAs and Fe/Co films at 10K. With the pinning of the Co layer, the coercivity of the Fe layer is 30mT, while the coercivity of the GaMnAs layer is 3mT. The magnetic field is applied in the plane. (b) Magnetoresistance of the device plotted as a function of the magnetic field in the plane. The magnetic alignments of the electrodes are indicated by arrows. The solid line represents a magnetic field sweep from negative towards positive saturation. With applied voltage of 1450mV, the negative magnetoresistance of 1.02% is found at 4.2K.*

the semiconductor transport length and r_b^* is the interface resistance. Since the resistivity of GaMnAs and GaAs are almost the same, the interface re-

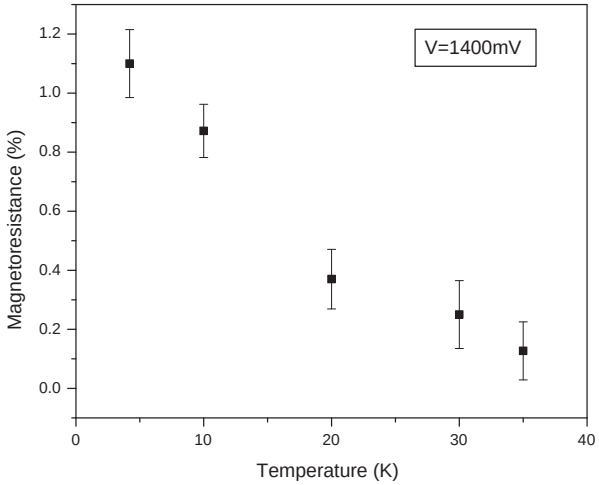

Figure 8.7: *Magnetoresistance ratio versus temperature. The applied voltage is 1400mV.*

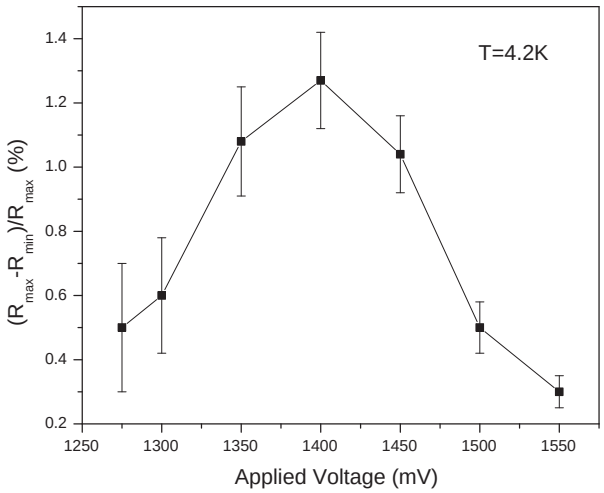

Figure 8.8: *Magnetoresistance ratio versus voltage measured at 4.2K.*

sistivity is dominated by the Schottky barrier between Fe and GaAs. When the voltage applied on the Fe/GaAs Schottky barrier is varied, the interface resistivity increases or decreases accordingly, hence the magnetoreistance reaches the maximum value.

8.2 Spin injection in a F/SC/F structure

So far spin injection phenomena were studied in the magnetic *p-n* junction diode, where the magnetic semiconductor GaMnAs is used as the detector for the injected spin-polarized electrons. Devices with two ferromagnetic metal contacts which serve as spin injector and detector are more challenging. In this section we report our experimental findings of spin-polarized transport in a ferromagnet/semiconductor/ferromagnet (F/SC/F) device with controlled Schottky barriers between the ferromagnetic metals and the semiconductors.

8.2.1 Sample design and structure

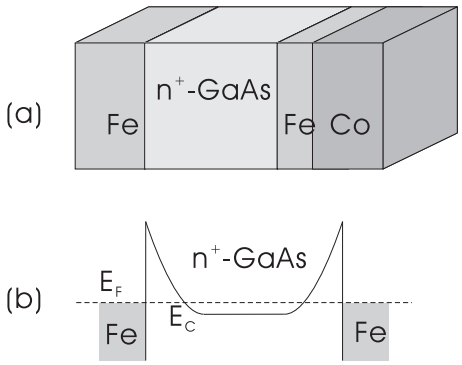

Figure 8.9: *(a) The geometry of the spin injection device of a Fe/GaAs/Fe structure. (b) Band-energy schemes for the spin injection device. When a bias is applied on the device, the spin-polarized electrons are injected from the ferromagnetic metal into the GaAs semiconductor and detected by the other ferromagnet.*

The geometry of the spin injection device is shown in Fig. 8.9(a). We use ferromagnetic metal layers of Fe as the injector and detector. In order to con-

GaAs transport width(nm)	Doping profile	With H_2 plasma etching	Magneto-resistance ratio
30	n^+	yes	no
50	n^+	no	no
	n^+	yes	0.07%
80(30/20/30)	$n^+/10^{16}cm^{-3}/n^+$	yes	no

Table 8.1: *List of spin injection measurements on Fe/GaAs/Fe structures. n^+ means that the doping density is around $3 \times 10^{18} cm^{-3}$.*

trol the magnetization configuration between these two ferromagnetic layers, a Co layer was deposited for magnetic pinning. Employing the EBASE technology which was introduced in chapter 3, the transport region of GaAs is sandwiched between the two ferromagnetic metal layers. In our structure, the current is transported perpendicular through the ferromagnetic metal and semiconductor. According to the calculation and analysis of Fert et al. [83], if the semiconductor thickness (t_N) is small enough, there is fairly broad range for the magnetoresistance to approach its highest value. Our perpendicular structure (different from 'lateral device') provides the possibility to control the transport region of the semiconductor on the scale of nanometers.

Again, the Schottky barriers between Fe and GaAs are used to overcome the conductance mismatch problem. As we discussed in chapter 7, since the interface resistivity of the Schottky barrier between highly doped GaAs and Fe can meets the requirements for efficient spin injection, the doping density of the semiconductor in our device has to be carefully controlled. The band diagram of the device is shown in Fig. 8.9(b). The Fermi energy is below the conduction band in the semiconductor because of the heavily doping.

8.2.2 Spin injection results and discussion

The experimental results performed using different surface treatment and different doping profiles are summarized in Tab. 8.1. From the analysis in chapter 7, the doping density of the GaAs was chosen as $3 \times 10^{18} cm^{-3}$. Since the depletion layer width between Fe and GaAs is around 17nm, the trans-

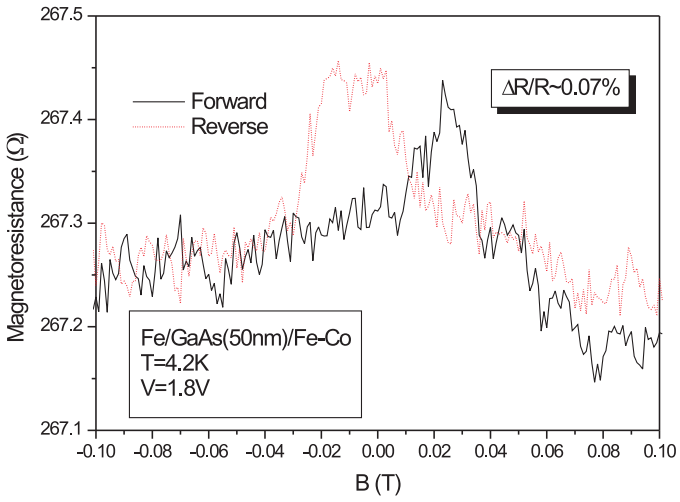

Figure 8.10: *Magnetoresistance as a function of the external magnetic field in the plane of the Fe/GaAs/Fe structure. The measurements are taken at 4.2K with an applied bias of 1.8V.*

port region of GaAs should be larger than that value. A spin injection signal could only be found in the device with 50nm homogeneous heavily doped GaAs. Fig. 8.10 shows the variation of the injector-detector resistance of the spin injection device at 4.2K under a large bias of 1800mV. By sweeping the applied magnetic field, the magnetization configuration of the Fe and Fe/Co layers are changed due to the different coercivity of the contacts. When the magnetic field is swept from negative to positive, between 3mT and 30mT, the magnetization of the ferromagnetic contacts are expected to be antiparallel. Otherwise, they are parallel. For the antiparallel case, a small but clear magnetoresistance rise of 0.07% could be recorded.

From the theoretical calculation [83], the magnetoresistance in a F/SC/F junction can be expressed as (see equation (6.23)):

$$\frac{\Delta R}{R^{(P)}} \simeq \frac{\gamma^2}{1-\gamma^2},$$

where γ is the spin polarization of the interface resistance, which is P in the usual notation of spin dependent tunneling. From the magnetoresis-

tance ratio of 0.07%, we obtain a spin polarization of 2.6% at the interface of Fe/GaAs/Fe structure. The magnetoresistance can only be found when a large bias, around 1.8V, is applied on the junction. This is in agreement with the observation of spin filtering across a NiFe/GaAs interface according to the configuration of the photon helicity with respect to the magnetization in the NiFe, when the barrier is under reverse bias up to 2V [100, 101]. Furthermore, as we discussed in the last chapter, the large bias on the Fe/GaAs Schottky barrier can decrease the interface resistance and fulfill the Fert conditions for spin injection in F/SC/F structures.

The comparison of spin injection in the samples with 50nm barriers with or without hydrogen plasma etching before the sputtering of the ferromagnetic contact layers shows the importance of surface pre-treatments. On the other hand, the missing of the spin injection signal in the inhomogeneous doped sample indicates that the doping profile is also one of the key aspects to improve the spin injection efficiency in F/SC/F structures. Although the calculations about spin injection at a Schottky contact from Albrecht and Smith et al. find that a depletion region is highly undesirable for spin injection [102], the detailed mechanism of spin injection through Schottky barriers, for example the effect of recombination in the space charge region, is still not clear. There are still many issues waiting for clarify of the straightforward spin injection in such a F/SC/F structure.

Summary

The goal when the research was started was the realization of the spin injection in F/SC/F junctions, where GaAs is chosen as the transport region and the Fe layers are chosen as the metallic ferromagnetic injector and detector for the actual device. In order to understand the spin transport at the Fe/GaAs interface, the spin-polarized tunneling was studied first in Fe/GaAs/Fe magnetic tunneling junctions. Next the interface resistance of the Fe/GaAs Schottky barrier, which was suggested to overcome the conductance mismatch problem, was measured as a guide for the design of a spin injection device. Finally, the magnetic *p*-*n* junction diode and F/SC/F junctions were fabricated, and the spin injection was studied in these devices.

This thesis starts with the first chapter dedicated to the introduction of the fundamental concepts required to understand the physics of spin-polarized tunneling in magnetic tunneling junctions, especially in Fe/GaAs/Fe junctions. The ferromagnetism, Schottky barrier at the interface of metal and semiconductor are introduced. The mechanisms for tunneling and the basics of magnetic tunneling junctions including the Jullière model are also presented.

With regards to the spin transport at the interface of a ferromagnetic metal and a semiconductor, the spin-polarized tunneling in Fe/GaAs/Fe magnetic tunneling junctions was investigated. Our early experiments showed the TMR effect is much lower than the value predicted by Jullière's model. In order to understand this phenomenon, the temperature dependence of the spin-polarized tunneling was studied. The TMR effect of Fe/GaAs/Fe/Co junctions as well as the *I*-*V* characteristics were measured at different temperatures. A theoretical model including spin dependent tunneling and spin independent tunneling to describe the temperature dependence of the TMR effect, which is proposed by Shang et al., was adopted for the analysis. In-

terpretation of the experimental data by the theoretical model allows us to characterize the junction quality and to explain the parameters spin polarization P, spin wave parameter α and spin-independent conductance G_{SI}. The study shows that the oxidation of the semiconductor surface and the interdiffusion between Fe and GaAs are key issues to increase the TMR effect in such a junction.

In order to improve the interface quality in the ferromagnet-semiconductor hybrid structures, it is important to find an effective way to prevent the oxidation of the barrier surface and interdiffusion between the ferromagnetic electrode and the semiconductor. Since the study of the epitaxial growth of Fe on sulphur-passivated GaAs shown that the chemical inertness of the passivated surface could prevent the oxidation and the interdiffusion of semiconductor material, the spin-polarized tunneling through such a sulphur-passivated GaAs barrier was studied to clarify the passivation effect. Our experiments show that the sulfide passivation increases the barrier height of 0.62eV to 0.67eV. However, the TMR effect decreases at all applied voltages. On the other hand, the experiments using hydrogen plasma etching to remove the native oxide layer on the GaAs barrier surface showed that it can effectively increase the spin polarization at the ferromagnet interface. Hence, this kind of surface pre-treatment was adopted in the fabrication of spin injection devices.

The fundamental concepts and theoretical model required to understand the physics of spin transport in hybrid ferromagnet and non-magnetic material system, and in semiconductor heterostructure in particular are reviewed. The difference in conductivities between a metal and a semiconductor represents the basic obstacle to effective spin injection, which can be overcome by introducing an interface resistance. Spin injection in a F/SC/F structure requires to fulfill the Fert's conditions. Effective spin injection into a semiconductor can also be achieved if the resistance mismatch is reduced by using a magnetic semiconductor as a spin injector. The theoretical analysis and numerical calculation of the spin injection through the space-charge region in magnetic p-n junctions shows that the spin-polarized electrons can only be injected when the bias applied over the junction is increased to the high injection limit (typically above 1V).

Before performing the spin injection experiments, we measured the interface resistivity of Fe/GaAs Schottky barrier. The current transport mecha-

nisms through the Schottky barrier, which are thermionic emission, thermionic-field emission and field emission, were introduced, followed by the calculation of the depletion layer width and the Fermi level of the Schottky barrier with different doping densities in GaAs. Fe/GaAs Schottky barriers were fabricated and the *I-V* characteristics as well as the interface resistivities were measured. From the calculation and the experiments, we find that increasing the bulk doping density decreases the depletion region width and changes the interface resistance. If we can control the transport length on the scale of nanometers, the interface resistance of a Fe/GaAs barrier with high doping density can meet Fert's condition for efficient spin injection into semiconductors. The measured interface resistance serves as a guide for designing spin injection experiments with respect to the interface properties and device structure.

Experimentally, we studied spin injection in a magnetic *p-n* junction diode and a Fe/GaAs/Fe structure. The interface resistance of Fe/GaAs was used to overcome the conductance mismatch in these devices and the surface pretreatment by hydrogen plasma etching was used to increase the spin polarization of the ferromagnetic contact layer. A negative GMR-like effect was found in the magnetic *p-n* junction diode with large bias, when the relative magnetizations of the two magnetic electrodes are changed from parallel to antiparallel. In the F/SC/F structures, Fe serves as the spin injector and detector while GaAs is transport channel. A spin injection signal could only be found in the device with a 50nm homogeneous heavily doped GaAs channel under a large bias of 1800mV. A small but clear magnetoresistance ratio of 0.07% was found, indicating a surface spin polarization of 2.6% in the Fe/GaAs/Fe structure.

Appendix: processing steps for device fabrication

Ideal sample size for processing: 5mm×5mm
Host substrate size: 4mm×4mm

Basic process

Chemical-mechanical polishing(CMP)

- Measure the thickness of the wafer
- Stick the wafer on the glass holder with wax at a temperature of 150°C, the epitaxial side facing to the glass
- Clean all the wax out of the edge of the wafer with acetone, heat the glass with wafer to 150°C again to flatten the wax underneath
- Prepare the polishing solution: 10% Br in methanol and set up the polishing pad
- Polish, adding the polishing solution every 30 seconds. The etch rate is around 50μm/min
- Stop etching when the wafer thickness is around 150μm
- Heat the holder to 150°C and take the wafer off. Clean the wafer with acetone and propanol.
- Cover the wafer with photoresist using spin coating, the parameter for spin coating is 2000rpm, 30sec, 'soft bake' at 90°C for 2 min

- Cut the wafer into 5mm×5mm pieces

Standard cascade rinse

- 1 min in acetone, which is heated to 90°C
- Rinse with acetone and leave in acetone for another 30sec, room temperature
- Repeat last step
- Rinse with acetone and leave in propanol waiting for next step

Spin coating of photoresist

- Set spin coating parameter
- Put the sample from propanol on the holder of spinner
- Dry the sample with N_2 gas
- Put a drop of liquid photoresist onto the sample
- Spin the sample and make coating
- Soft-baking

Lithography for etching

- Start the exposure machine and set exposure time
- Put photomask on the mask holder, adjust the focus of the microscope
- Put the sample on the sample holder, align the sample to the pattern on the mask
- Exposure with exact time
- Make up the developing solution
- Develop with exact time and rinse the sample to stop the developing
- Dry the sample with N_2 gas

Lithography for lift-off

- Start the exposure machine and set exposure time
- Put photomask on the mask holder, adjust the focus of the microscope
- Put sample on the sample holder, align the sample to the pattern on the mask
- Exposure with exact time
- Soak the sample in chlorobenzene
- Hard-baking
- Make up the developing solution
- Develop with exact time and rinse the sample to stop the developing
- Dry the sample with N_2 gas

Etching of GaAs and AlGaAs layers

- Etch the sample in HCl(37%):H_2O=1:1 for 30sec to remove the native oxide layer on GaAs
- Etch the sample in citric acid:H_2O_2($\sim$35%)=10:1 for 2.5min to remove 100nm of GaAs
- Etch the sample in 1% HF acid for 30sec to remove 50nm of AlGaAs

Two-step etching of GaAs and AlGaAs layers

- Etch the sample in HCl(37%):H_2O=1:1 for 30sec to remove the native oxide layer on GaAs
- Etch the sample in citric acid:H_2O_2($\sim$35%)=10:1 for 2.5min to remove 100nm of GaAs
- Do 'lithography for etching' again, open large window of photoresist
- Etch the sample in 1% HF acid for 30sec to remove 50nm of AlGaAs

Etching of GaAs substrate and GaAs/AlAs superlattice

- Fix sample on the glass with wax to protect the metallic side, the new host substrate facing to the glass
- Etch the sample in HCl(37%):H_2O=1:1 for 30sec to remove the native oxide layer on GaAs
- Etch the sample in NH_4OH :H_2O_2(∼35%)=1:3, the etching time is determined by: $Time$(min)=[$Thickness$(μm)−30]/7.4
- Etch the sample in NH_4OH:H_2O_2=5:95, etching time guided by color change of the surface
- Etch the sample in citric acid:H_2O_2(∼35%)=10:1, 1-2 hours
- Etch the sample in 10% HF acid for 1min to remove 300nm GaAs/AlAs superlattice layer
- Take off the sample from the glass and do standard cascade rinse

Evaporation

- Start the evaporation machine: UNIVEX 550
- Fix the sample on the holder
- Vacuum the chamber below 5×10^{-6} mbar
- Evaporate the metal and control the film thickness, deposition rate: Fe 0.1-0.3Å/s, Au 1.5Å/s, Cr 0.5Å/s

Sputtering with H_2 plasma etching

- Fix the sample on the holder, put the holder into exchange chamber
- Vacuum the exchange chamber for 30 min
- Insert the holder into the main chamber and rotate the sample to face the target metal using stepping-motor
- H_2 plasma etching: H_2 4sccm, power 20mA, Anode 0.4KV(inner)/0.6KV(ext), time 30min

- Control the flow of Ar to 7sccm
- Sputtering the metal and control the film thickness, power for sputtering: Fe 5W, Co 10W, Au 50W

Lift-off

- Put the sample into acetone
- Heat at 90°C for several minutes
- Scratch the photoresist along the sample edge and peel off the film by acetone rinse
- Ultrasonic agitation of the acetone for several seconds, if the resist 'ears' at the edge of a structure can not be removed

Epoxy bonding onto a new host substrate

- Standard cascade rinse
- Mount the sample on the small glass with wax, the metallic side facing upside
- Glue the sample and the new host substrate face to face with MBond 600
- Bake the sample with applied pressure at 80°C for 4 hours
- Take off the sample from the glass
- Put the sample into acetone heated at 90°C for 2 minutes
- Standard cascade rinse

PECVD of SiO_2

- Start PECVD machine
- Load recipe 'Aufheizen auf 95°C' to pre-heat the sample holder table
- Put sample on the table, open the valves of N_2O and SiH_4 gas suppliers

- Choose recipe of 'dom 08481 SiO_2-Oxford', set parameters as: temperature 100°C, pressure 1000mbar, step time 2.5min (deposition rate: 40nm/min)
- Start the deposition
- Take out the sample after the deposition is finished

A. Processing steps for tunneling magnetic junctions

1. Sputtering of the first contact

- Thin down the wafer to 150μm using chemical-mechanical polishing
- Measure the thickness of the sample
- Standard cascade rinse
- Spin coating of photoresist: Shipley 1805, coating: 4500rpm, 30sec; soft baking: 90°C, 2min
- Lithography for etching: exposure: 11sec; developing solution: 1 Microposit: 4 H_2O; developing time: 40sec
- Etching of GaAs and AlGaAs layers
- Sputtering with H_2 plasma etching: Fe 12nm, Au 150nm
- Lift-off

2. Epoxy bonding and etching

- Standard cascade rinse
- Epoxy bonding onto a new host substrate
- Etching of GaAs substrate and GaAs/AlAs superlattice

3. Sputtering of the second contact

- Standard cascade rinse
- Spin coating of photoresist: Shipley 1805, coating: 4500rpm, 30sec; soft baking: 90°C, 2min
- Lithography for etching: exposure: 11sec; develop solution: 1 Microposit: 4 H_2O; developing time: 40sec
- Two-step etching of GaAs and AlGaAs layers
- Sputtering with H_2 plasma etching: Fe 12nm, Co 50nm, Au 120nm
- Lift-off

4. Mesa etching and evaporation of Cr/Au

- Standard cascade rinse
- Spin coating of photoresist: Shipley 1805, coating: 4500rpm, 30sec; soft baking: 90°C, 2min
- Lithography for etching: exposure: 11sec; developing solution: 1 Microposit: 4 H_2O; developing time: 40sec
- Etching of 100nm GaAs, etching time: 40sec
- Etching of 50nm AlGaAs, etching time: 25sec
- Etching of GaAs thin barrier, etching time: 10sec
- Standard cascade rinse
- Spin coating of photoresist: Shipley 1805, coating: 4500rpm, 30sec; soft baking: 90°C, 2min
- Lithography for lift-off: exposure: 20sec; developing time: 75sec
- Evaporation: Cr 10nm, Au 200nm
- Lift-off

5. Gold wire bonding for testing

- Standard cascade rinse
- Spin coating of photoresist: Shipley 1805, coating: 4500rpm, 30sec; soft baking: 90°C, 2min
- Cut the sample into small pieces, each with four test patterns
- Standard cascade rinse
- Fix the small piece on the chip carrier with PMMA, baked at 90°C for 1min
- Au wire electrical bonding, connect the pattern to the chip carrier

B. Processing steps for magnetic p-n junction diodes

1. Evaporation of the first contact

- Thin down the wafter to 150μm using chemical-mechanical polishing
- Measure the thickness of the sample
- Standard cascade rinse
- Spin coating of photoresist: Shipley 1805, coating 4500rpm, 30sec; soft baking 90°C, 2min
- Lithography for lift-off: exposure 45sec; developing solution 1 Microposit:4 H_2O; developing time 40sec
- Evaporation of Au: Au 150nm, using 'plasma pre-sputtering' for 1min in order to roughen the GaMnAs surface
- Lift-off

2. Epoxy bonding and etching

- Standard cascade rinse
- Epoxy bonding onto a new host substrate
- Etching of GaAs substrate and GaAs/AlAs superlattice

3. Sputtering of the second contact

- Standard cascade rinse
- Spin coating of photoresist: Shipley 1805, coating 4500r/min, 30sec; soft baking 90°C, 2min
- Lithography for etching: exposure 55sec; develop solution 1 Microposit:4 H_2O; developing time 80sec
- Two-step etching of GaAs and AlGaAs layers
- Sputtering with H_2 plasma etching: Fe 12nm, Co 50nm, Au 120nm
- Lift-off

4. Mesa etching and evaporation of Cr/Au

- Standard cascade rinse
- Spin coating of photoresist: Shipley 1805, coating 4500rpm, 30sec; soft baking 90°C, 2min
- Lithography for etching: exposure 55sec; developing solution 1 Microposit:4 H_2O; developing time 80sec
- Etching of 100nm GaAs, etching time 40sec
- Etching of 50nm AlGaAs, etching time 25sec
- Etching of 75nmGaAs, etching time 40sec
- Standard cascade rinse
- Spin coating of photoresist: Shipley 1805, coating 4500rpm, 30sec; soft baking 90°C, 2min
- Lithography for lift-off: exposure 2min; developing time 80sec; chlorobenzene 1.5 min; hard-baking 3 min
- PECVD of SiO_2: 160nm
- Lift-off: by ultrasonic agitation

- Spin coating of photoresist: MAP 1215, coating 6000rpm, 5sec(acceleration), 30sec; soft baking 90°C, 9min
- Lithography for lift-off: exposure 5.5min; developer AR300-47; developing time 25sec; without chlorobenzene soaking and hard-baking
- Evaporation: Cr 10nm, Au 200nm
- Lift-off

5. Gold wire bonding for testing

- Standard cascade rinse
- Spin coating of photoresist: Shipley 1805, coating 4500rpm, 30sec; soft baking 90°C, 2min
- Cut the sample into small pieces, each with four test patterns
- Standard cascade rinse
- Fix the small piece on the chip carrier with PMMA, baked at 90°C for 1min
- Au wire electrical bonding, connect the pattern to the chip carrier

Publications

Peifeng Chen, Juergen Moser, Marcus Zenger, Dieter Weiss and Werner Wegscheider. *'Temperature dependence of spin polarized tunneling through epitaxial GaAs barriers'.* To be submitted.

Peifeng Chen, Juergen Moser, Philipp Kotissek, Janusz Sadowski, Marcus Zenger, Dieter Weiss and Werner Wegscheider. *'All-electrical measurement of spin injection in a magnetic p-n junction diode'.* To be submitted.

P. Kotissek, M. Bailleul. P. Chen, W. Wegscheider and G. Bayreuther. *'Remanent optical detection of electric spin injection through an FeCo/GaAs Schottky barrier'.* To be submitted.

Posters:

Juergen Moser, Marcus Zenger, Peifeng Chen, Werner Wegscheider and Dieter Weiss. *'Tunneling Through Single-Crystal GaAs(001) Barriers With Sputtered Fe-Contacts'.* Presented at DPG 2005.

P. Kotissek, M. Bailleul. P. Chen, W. Wegscheider and G. Bayreuther. *'Fe on GaAs(110) cleaved edges-magnetic, electrical and optical investigations towards spin injection'.* Presented at DPG 2005.

Marcus Zenger, Juergen Moser, Peifeng Chen, Stephan Kreuzer, Werner Wegscheider and Dieter Weiss. *'Tunneling Through Single-Crystal GaAs(001) Barriers'.* Presented at DPG 2004.

Bibliography

[1] G. A. Prinz
Magnetoelectronics
Science 282, 1998, 1660.

[2] D. Weiss
Seminconductors put spin in spintronics
Physics World, March, 2000, 23.

[3] J. De Boeck and G. Borghs
Magnetoelectronics
Physics World, 12, 1999, 27.

[4] D. Loss and D. Di Vincenozo
Quantum computation with quantum dots
Phys. Rev. A, 57, 1998, 120.

[5] Andrei Teodor Filip
Spin polarized electron transport in mesoscopic hybrid devices
Dissertation, RIJKSUNIVERSITEIT GRONINGEN, 2002.

[6] Igor Žutić, J. Fabian, and S. Das Sarma
Spintronics: Fundamentals and applications
REVIEWS OF MODERN PHYSICS, 76, 2004, 323.

[7] J. Kikkawa, I. P. Smorchkova, N. Samarth, and D. D. Awschalom
Lateral drag of spin coherence in gallium arsenide
Nature 397, 1999, 139.

[8] G. Schmidt, G. Richter, P. Grabs, C. Gould, D. Ferrand, and L.W. Molenkamp

Large magnetoresistance effect due to spin injection into a nonmagnetic semiconductor
Phys. Rev. Lett. 87, 2001, 227203.

[9] G. Schmidt, D. Ferrand, L.W. Molenkamp, A.T. Filip, and B.J. van Wees
Fundamental obstacle for electrical spin injection from a ferromagnetic metal into a diffusive semiconductor
Phys. Rev. B 62 (8), 2000, R4790–R4793.

[10] P. M. Tedrow and R. Meservey
Spin Polarization of Electrons Tunneling from Films of Fe, Co, Ni, and Gd
Phys. Rev. B 7(1), 1973, 318–326.

[11] M. Jullière
Tunneling between ferromagnetic films
Physics Letters 54A (3), 1975, 225–226.

[12] Jagadeesh S. Moodera
Spin-polarized tunnelling, magnetoresistance and interfacial effects in ferromagnetic junctions
Philosophical Magazine B 80 (2), 2000, 195–206.

[13] T. Miyazaki and N. Tezuka
Giant magnetic tunneling effect in $Fe/Al_2O_3/Fe$ junction
J. Magn. Magn. Mat. 139, 1995, L231.

[14] J.S. Moodera, L.R. Kinder, T.M. Wong, and R. Meservey
Large Magnetoresistance at Room Temperature in Ferromagnetic Thin Film Tunnel Junctions
Phys. Rev. Lett. 74 (16), 1995, 3273–3276.

[15] S. S. P. Parkin, K. P. Roche, M. G. Samant, P. M. Rice, R. B. Beyers, R. E. Scheuerlein, E. J. O'Sullivan, S. L. Brown, J. Bucchigano, D. W. Abraham, Yu Lu, M. Rooks, P. L. Trouilloud, R. A. Wanner, and W. J. Gallagher
Exchange-biased magnetic tunnel junctions and application to nonvolatile magnetic random access memory
J. Appl. Phys. 85 (8), 1999, 5828–5833.

[16] Supriyo Datta and Biswajit Das
Electronic analog of the electro-optic modulator
Appl. Phys. Lett. 56 (7), 1990, 665–667.

[17] J. Kikkawa, I. P. Smorchkova, N. Samarth, and D. D. Awschalom
Room-Temperature Spin Memory in Two-Dimensional Electron Gases
Science 277, 1997, 1284.

[18] R. I. Dzhioev, K. V. Kavokin, V. L. Korenev, M. V. Lazarev, B. Ya. Meltser, M. N. Stepanova, B. P. Zakharchenya, D. Gammon, and D. S. Katzer
Low-temperature spin relaxation in n-type GaAs
Phys. Rev. B 66, 2002, 245204.

[19] S. Gardelis, C. G. Smith, C. H. W. Barnes, E. H. Linfield, and D. A. Ritchie
Spin-valve effects in a semiconductor field-effect transistor: A spintronic device
Phys. Rev. B 60, 1999, 7764.

[20] P. R. Hammar, B. R. Bennett, M. J. Yang, and Mark Johnson
Observation of Spin Injection at a Ferromagnet-Semiconductor Interface
Phys. Rev. Lett. 83 (1), 1999, 203–206.

[21] H. X. Tang, F. G. Monzon, R. Lifshitz, M. C. Cross, and M. L. Roukes
Ballistic spin transport in a two-dimensional electron gas
Phys. Rev. B. 61 (1), 2000, 4437.

[22] F. G. Monzon, Mark Johnson, and M. L. Roukes
Strong Hall voltage modulation in hybrid ferromagnet/semiconductor microstructures
Appl. Phys. Lett. 71, 1997, 3088.

[23] E. I. Rashba
Theory of electrical spin injection: Tunnel contacts as a solution of the conductivity mismatch problem
Phys. Rev. B 62, 2000, R16267.

[24] G. Schmidt and L. W. Molenkamp
Spin injection into semiconductors, physics and experiments
Semicond. Sci. Technol. 17, 2002, 310.

[25] H.J. Zhu, M. Ramsteiner, H. Kostial, M. Wassermeier, H.P. Schönherr, and K.H. Ploog
Room-Temperature Spin Injection from Fe into GaAs
Phys. Rev. Lett. (87), 2001, 016601.

[26] O. M. J. van't Erve, G. Kioseoglou, A. T. Hanbicki, C. H. Li, B. T. Jonker, R. Mallory, M. Yasar, and A. Petrou
Comparison of Fe/Schottky and Fe/Al_2O_3 tunnel barrier contacts for electrical spin injection into GaAs
Appl. Phys. Lett. 84, 2004, 4334.

[27] A. T. Hanbicki, B. T. Jonker, G. Itskos, G. Kioseoglou, and A. Petrou
Efficient electrical spin injection from a magnetic metal/tunnel barrier contact into a semiconductor
Appl. Phys. Lett. 80, 2002, 1240.

[28] Y. Ohno, D. K. Young, B. Beschoten, F. Matsukura, H. Ohno, and D. D. Awschalom
Electrical spin injection in a ferromagnetic semiconductor heterostructure
Nature 402, 1999, 790.

[29] E. Johnston-Halperin, D. Lofgreen, R.K. Kawakami, D.K. Young, L. Coldren, A.C. Gossard, and D.D. Awschalom
Spin-polarized Zener tunneling in (Ga,Mn)As
Phys. Rev. B 65, 2002, 041306.

[30] S. Kreuzer, J. Moser, W. Wegscheider, D. Weiss, M. Bichler, and D. Schuh
Spin polarized tunneling through single-crystal GaAs(001) barriers
Appl. Phys. Lett. 80, 2002, 4582.

[31] M. Zenger, J. Moser, W. Wegscheider, D. Weiss, and T. Dietl
High-field magnetoresistance of Fe/GaAs/Fe tunnel junctions
J. Appl. Phys. 96, 2004, 2400.

[32] M. Kemerink, K. Sauthoff, P.M. Koenraad, J.W. Gerritsen, H. van Kempen, and J.H. Wolter
Optical Detection of Ballistic Electrons Injected by a Scanning-Tunneling Microscope
Phys. Rev. Lett. 86, 2001, 2404.

[33] O. Gunnarsson
Band model for magnetism of transition metals in the spin-density-functional formalism
J. Phys. F: Metal Phys. 6 (4), 1976, 587–606.

[34] J. F. Janak
Uniform susceptibilities of metallic elements
Phys. Rev. B 16 (1), 1977, 255–261.

[35] D. G. Pettifor
Electronic structure calculations and magnetic properties
J. Magn. Magn. Mat. 15–18, 1980, 847–852.

[36] F.J. Himpsel, J.E. Ortega, G.J. Mankey, and R.F. Willis
Magnetic Nanostructures
Advances in Physics 47 (4), 1998, 511–597.

[37] Fredrik Gustavsson
Properties of Fe/ZnSe Heterostructures
Dissertation, UPPSALA, 2002.

[38] S. M. Sze
Physics of Semiconductor Devices
John Wiley & Sons, New York, 1981.

[39] Michael Shur
Physics of Semiconductor Devices, 2nd edition
Prentice Hall, New Jersey, 1990.

[40] R.T. Tung
Electron transport at metal-semiconductor interfaces: General theory
Phys. Rev. B 45, 1992, 13509–13523.

[41] J. L. Powell and B. Crasemann
Quantum Mechanics
Addison-Wesley Publishing Company, Inc., Reading, Massachusetts, 1961.

[42] E. L. Wolf
Principles of electron tunneling spectroscopy
Oxford University Press, New York, 1985.

[43] John G. Simmons
Generalized Formula for the Electric Tunnel Effect between Similar Electrodes Separated by a Thin Insulating Film
J. Appl. Phys. 34 (6), 1963, 1793–1803.

[44] John G. Simmons and George J. Unterkofler
Potential Barrier Shape Determination in Tunnel Junctions
J. Appl. Phys. 34 (6), 1963, 1828–1830.

[45] John G. Simmons
Electric Tunnel Effect between Dissimilar Electrodes Separated by a Thin Insulating Film
J. Appl. Phys. 34 (9), 1963, 2581.

[46] John G. Simmons
Generalized Thermal J-V-Characteristic for the Electric Tunnel Effect
J. Appl. Phys. 35 (9), 1964, 2655–2658.

[47] P. Rottländer, M. Hehn, and A. Schuhl
Determining the interfacial barrier height and its relation to tunnel magnetoresistance
Phys. Rev. B 65, 2002, 054422.

[48] P. Rottländer, M. Hehn, O. Lenoble, and A Schul
Tantalum oxide as an alternative low height tunnel barrier in magnetic junctions
Appl. Phys. Lett. 78(21), 2001, 3274.

[49] R. Meservey and P. M. Tedrow
Spin-polarized electron tunneling
Physics Reports 238 (4), 1994, 173–243.

[50] D. Paraskevopoulos, R. Meservey, and P.M. Tedrow
Spin polarization of electrons tunneling from 3d ferromagnetic metals and alloys
Phys. Rev. B 16, 1977, 4907.

[51] R.J. Soulen Jr, J.M. Byers, M.S. Osofsky, B. Nadgorny, T. Ambrose, S.F. Cheng, P.R. Broussard, C.T. Tanaka, J. Nowak, J.S. Moodera, A. Barry, and J.M.D Coey
Measuring the spin polarization of a metal with a superconducting point contact
Science 282, 1998, 85.

[52] M. Zölfl, M. Brockmann, M. Kohler, S. Kreuzer, T. Schweinbock, S. Miethaner, F. Bensch, and G. Bayreuther
Magnetic films epitaxially grown on semiconductors
J. Magn. Magn. Mater. 175, 1997, 16.

[53] Stephan Kreuzer
Spinpolarisiertes Tunneln durch einkristalline Halbleiterbarrieren
Dissertation, Universität Regensburg, 2001.

[54] M.V. Weckwerth, J.A. Simmons, N.E. Harff, M.E. Sherwin, M.A. Blount, W.E. Baca, and H.C. Chui
Epoxy bond and stop-etch (EBASE) technique enabling backside processing of (Al)GaAs heterostructures
Supperlattices and Microstructures 20 (4), 1996, 561–567.

[55] C. T. Foxon and B. A. Joyce
Growth of thin films and heterostructures of III-V componds by molecular beam epitaxy
in Groth and characterisation of semiconductors, Adam Hilger, New York, 1990, 35–64.

[56] J. L. Merz, R. A. Logan, and A. M. Sergent
GaAs Integrated Optical circuits by Wet Chemical Etching
J. Quantum Electron. QE-15 (2), 1979, 72–81.

[57] C. Juang, K. J. Kuhn, and R. B. Darling
Selective etching of GaAs and $Al_{0.30}Ga_{0.70}As$ with citric acid/hydrogen

peroxide solutions
J. Vac. Sci. Technol. B 8 (5), 1990, 1122–1124.

[58] E. Yablonovitch, T. Gmitter, J.P. Harbison, and R. Bhat
Extreme selectivity in the lift-off of epitaxial GaAs films
Appl. Phys. Lett. 51 (26), 1987, 2222–2224.

[59] Shabbir A. Bashar
Study of Indium Tin Oxide (ITO) for Novel Optoelectronic Devices
Dissertation, University of London, 1998.

[60] R. H. Chang and S. Darack
Hydrogen plasma etching of GaAs oxide
Appl. Phys. Lett. 38 (11), 1981, 898.

[61] K.D. Choquette, R.J. Shul, A.J. Howard, D.J. Rieger, R.S. Freund, and R.C. Wetzel
Smooth reactive ion etching of GaAs using a hydrogen plasma pretreatment
J. Vac. Sci. Technol. B 13 (1), 1995, 40.

[62] J. Clarke
Squids
Scientific American 271, 1994, 46.

[63] C.H. Shang, J. Nowak, R. Jansen, and J.S. Moodera
Temperature dependence of magnetoresistance and surface magnetization in ferromagnetic tunnel junctions
Phys. Rev. B 58, 1998, R2917.

[64] J. Faure-Vincent, C. Tiusan, E. Jouguelet, F. Canet, M. Sajieddine, C. Bellouard, E. Popova, M. Hehn, F. Montaigne, and A. Schuhl
High tunnel magnetoresistance in epitaxial Fe/MgO/Fe tunnel junctions
Appl. Phys. Lett. 82 (25), 2003, 4507.

[65] R. Jansen and J. S. Moodera
Magnetoresistance in doped magnetic tunnel junctions: Effect of spin scattering and impurity-assisted transport
Phys. Rev. B 61 (13), 2000, 9047–9050.

[66] S. Zhang, P. M. Levy, A. C. Marley, and S. S. P. Parkin
Quenching of Magnetoresistance by Hot Electrons in Magnetic Tunnel Junctions
Phys. Rev. Lett. 79 (19), 1997, 3744–3747.

[67] D. Scholl, M. Donath, D. Mauri, E. Kay, J. Mathon, R.B. Muniz, and H.C. Siegmann
Exchange interactions at the surface of a ferromagnet
Phy. Rev. B 43, 1991, 13309.

[68] J. Mathon and S. B. Ahmad
Quasi-two-dimensional behavior of the surface magnetization in a ferromagnet with softened surface exchange
Phy. Rev. B 37, 1988, 660.

[69] G. Lugert and G. Bayreuther
Temperature dependence of the hyperfine field and magnetization in ultrathin epitaxial Fe films
Phys. Rev. B 38(16), 1988, 11068.

[70] W. F. Brinkman, R. C. Dynes, and J. M. Rowell
Tunneling Conductance of Asymmetrical Barriers
J. Appl. Phys. 41 (5), 1970, 1915–1921.

[71] T. Hagler, R. Kinder, and G. Bayreuther
Temperature dependence of tunnel magnetoresistance
J. Appl. Phys. 89 (11), 2001, 7570.

[72] G. W. Anderson, M. C. Hanf, and P. R. Norton
Growth and magnetic properties of epitaxial Fe(100) on S-passivated GaAs(100)
Phys. Rev. Lett. 74, 1995, 2764.

[73] J. J. Krebs, B. T. Jonker, and G. A. Prinz
Properties of Fe single-crystal films grown on (100)GaAs by molecular-beam epitaxy
J. Appl. Phys. 61 (7), 1987, 2596.

[74] L. I. Glazman and K. A. Matveev
Inelastic tunneling across thin amorphous films
Sov. Phys. JETP 67, 1988, 1276.

[75] Zisen Li, Cornelis de Groot, and Jagadeesh H. Moodera
Gallium oxide as an insulating barrier for spin-dependent tunneling junctions
Appl. Phys. Lett. 77 (22), 2000, 3630–3632.

[76] B. Lépine, S. Ababou, A. Guivarc'h, G. Jézéquel, S. Députier, R. Guérin, A. Filipe, A. Schuhl, F. Abel, C. Cohen, A. Rocher, and J. Crestou
Solid state interdiffusions in epitaxial Fe/GaAs (001) heterostructures during ultrahigh vacuum annealings up to 450° C
J. Appl. Phys. 83 (6), 1998, 3077.

[77] M.S. Carpenter, M.R. Melloch, M.S. Lundstrom, and S.P. Tobin
Effects of Na_2S and $(NH_4)_2S$ edge passivation treatments on the dark current-voltage characteristics of GaAs pn diodes
Appl. Phys. Lett. 52, 1988, 2157.

[78] G. W. Anderson, M. C. Hanf, X. R. Qin, P. R. Norton, K. Myrtle, and B. Heinrich
Epitaxial growth of Fe on sulphur-passivated GaAs(100): a method for preventing As interdiffusion
Surf. Sci. 346, 1996, 145.

[79] F. P. Zhang, P. S. Xu, E. D. Lu, H. Z. Guo, F. Q. Xu, and X. Y. Zhang
Growth and magnetic properties of Fe overlayer on S-passivated GaAs substrate
Thin Solid Films, 375, 2000, 64.

[80] M.J. Jeng, H.T. Wang, L.B. Chang, Y.C. Cheng, and S.T. Chou
Barrier height enhancement of Ag/n-GaAs and Ag/n-InP Schottky diodes prepared by $P_2S_5/(NH_4)_2S_x$ and HF treatments
J. Appl. Phys. 86 (11), 1999, 6261.

[81] Mark Johnson and R. H. Silsbee
Coupling of electronic charge and spin at a ferromagnetic-paramagnetic metal interface
Phys. Rev. B 37(10), 1988, 5312.

[82] P.C. van Son, H. van Kempen, and P. Wyder
Boundary resistance of the ferromagnetic-nonferromagnetic metal interface
Phys. Rev. Lett. 58, 1987, 2271.

[83] A. Fert and H. Jaffrès
Conditions for efficient spin injection from a ferromagnetic metal into a semiconductor
Phys. Rev. B 64, 2001, 184420.

[84] D. L. Smith and R. N. Silver
Electrical spin injection into semiconductors
Phys. Rev. B 64, 2001, 045323.

[85] H. Ohno, A. Shen, F. Matsukura, A. Oiwa, A. Endo, S. Katsumoto, and Y. Iye
(Ga,Mn)As: A new diluted magnetic semiconductor based on GaAs
Appl. Phys. Lett. 69, 1996, 363.

[86] H. Ohno
Making Nonmagnetic Semiconductors Ferromagnetic
Science 281, 1998, 951.

[87] H. Ohno
Properties of ferromagnetic III-V semiconductors
J. Magn. Magn. Mater. 200, 1999, 110.

[88] T. Dietl, H. Ohno, and F. Matsukura
Hole-mediated ferromagnetism in tetrahedrally coordinated semiconductors
Phys. Rev. B 63, 2001, 195205.

[89] D. Chiba, N. Akiba, F. Matsukura, Y. Ohno, , and H. Ohno
Magnetoresistance effect and interlayer coupling of (Ga,Mn)As tri-

layer structures
Appl. Phys. Lett. 77, 2000, 1873.

[90] M. Tanaka and Y. Higo
Large tunneling magnetoresistance in GaMnAs/AlAs/GaMnAs ferromagnetic semiconductor tunnel junctions
Phys. Rev. Lett. 87, 2001, 026602.

[91] Jaroslav Fabian, Igor Žutić, and S. Das Sarma
Theory of spin-polarized bipolar transport in magnetic p-n junctions
Phys. Rev. B 66, 2002, 165301.

[92] I. Žutić, J. Fabian, and S.D. Sarma
Spin injection through the depletion layer: A theory of spin-polarized p-n junctions and solar cells
Phys. Rev. B 64, 2001, 121201.

[93] I. Žutić, J. Fabian, and S. Das Sarma
Spin-polarized transport in inhomogeneous magnetic semiconductors: theory of magnetic/nonmagnetic p-n junctions
Phys. Rev. Lett. 88, 2002, 066603.

[94] Igor Žutić and J. Fabian
Spin-voltaic effect and its implications
Mater. Trans., JIM 44, 2003, 2062.

[95] F. A. Padovani and R. Stratton
Field and thermionic-field emission in Schottky barriers
Solid State Electronics, 9, 1966, 695.

[96] Stefan Sassen, Bernd Witzigmann, Claus Wolk, and Hans Brugger
Barrier height engineering on GaAs THz Schottky diodes by means of high-low doping, InGaAs- and InGaP layers
IEEE Trans. Electron Devices, 47, 2000, 24.

[97] J. Gyulai, J.W. Mayer, V. Rodriguez, AYC Yu, and H.J. Copen
Alloying behaviour of Au and AuGe on GaAs
J. Appl. Phys., 42, 1971, 3578.

[98] Otfried Madelung (Hrsg.)
Semiconductors - Basic Data
2nd ed., Springer-Verlag, Berlin, 1996.

[99] J. Kikkawa and D. D. Awschalom
Resonant spin amplification in n-Type GaAs
Phys. Rev. Lett. 80, 1998, 4313.

[100] A. Hirohata, Y.B. Xu, C.M. Guertler, and J. Bland
Spin-polarized electron transport in a NiFe/GaAs Schottky diode
J. Magn. Magn. Mat. 226–230, 2001, 914–916.

[101] J. A. C. Bland, A. Hirohata, C. M. Guertler, Y. B. Xu, and M. Tselepi
Spin-polarized electron transport in ferromagnet/semiconductor hybrid structures (invited)
J. Appl. Phys. 89(11), 2001, 6740.

[102] J. D. Albrecht and D. L. Smith
Electron spin injection at a Schottky contact
Phy. Rev. B 66, 2002, 113303.

Acknowledgments

First and foremost I offer my sincerest gratitude to my supervisor, Prof. Werner Wegscheider, who has supported me throughout my thesis work with his patience and knowledge. And I would also like to appreciate the help from Prof. Dieter Weiss, because without their generosity, ideas, encouragement and efforts, I could not complete my work and write this thesis. Also thank Prof. Karl F. Renk for providing the scholarship at the beginning of my study.

In the various laboratories for the experiments, I thank Stephan Kreuzer, who helped tutor me the whole process of devices fabrication in the cleaning room. I will especially thank Jürgen Moser and Marcus Zenger, who have provided me a lot of good arguments and useful suggestions during my work. I learned so many things from both of you, and without your kind help, this work will be definitely impossible. Thank Dieter Schuh, Matthias Reinwald, Christian Gerl, Peter Tranitz and Janusz Sadowski in our MBE group to prepare various samples for me. Thank Thomas Feil and Matthias Habl to show me the CEO preparation procedure and van der Pauw measurements at low temperature. Thomas Hagler showed me the sputtering and oxidation of aluminum. Thank Philipp Kotissek for your advice about spin injection device design and helped me to do the SQUID measurements with Matthias Sperl.

Beyond my experimental works, I would like to thank all the members in our group, especially Stephan Haneder, Ursula Wurstbauer and Johannes Bauer who share the same office with me, Elisabeth Reinwald, Robert Schuster and our secretaries Renate Creuzburg and Annemarie Dinkel, for their kindness and friendly help. Thank Peter Mueller, our technician, for his friendly smiles and a hello every time we met.

To my friends, Dr. Jiyan Shi, Dr. Shidong Wang and his wife Yuanyuan Ma, thank you for your words of encouragement. Dr. Shidong Wang spent so much time in proof-reading my thesis and articles. His help and discussion are invaluable. Finally, I thank my parents and my wife for supporting me throughout all my studies. Without your love and support, nothing in my life could be achieved.